

Defining the Role of Elastic Lubricants and Micro Textured Surfaces in Lubricated, Sliding Friction

by

Sara J. Hupp

B.S., Mechanical Engineering
Virginia Polytechnic Institute and State University, 2002

M.S., Mechanical Engineering
Massachusetts Institute of Technology, 2004

Submitted to the Department of Mechanical Engineering
In Partial Fulfillment of the Requirements for the Degree of

Doctor of Philosophy in Mechanical Engineering

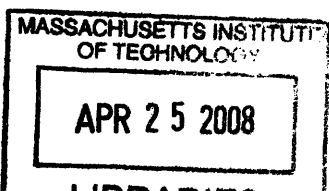
at the
Massachusetts Institute of Technology
February 2008

© 2008 Massachusetts Institute of Technology
All rights reserved

Signature of Author..... 
Department of Mechanical Engineering
January 15, 2008

Certified by..... 
Professor Douglas P. Hart
Professor of Mechanical Engineering
Thesis Supervisor

Accepted by..... 
Professor Lallit Anand
Chairman, Department Committee on Graduate Students
Department of Mechanical Engineering



ARCHIVES

Defining the Role of Elastic Lubricants and Micro Textured Surfaces in Lubricated, Sliding Friction

by

SARA JEAN HUPP

Submitted to the Department of Mechanical Engineering
on January 15, 2008 in partial fulfillment of the
requirements for the degree of
Doctor of Philosophy in Mechanical Engineering

ABSTRACT

Solutions for reducing friction in sliding, lubricated systems include modifying lubricant rheology using polymers and adding a micro-scale texture to the sliding surfaces, but the mechanism of how lubrication properties and surface texturing interact is poorly understood. This thesis presents a study of lubricant elasticity and surface micro texturing and explains the mechanisms for the resulting altered frictional profile on the Stribeck diagram.

In this work, isolating non-Newtonian effects in the lubrication flow is shown to normalize the frictional profiles of elastic and Newtonian lubricants. These non-Newtonian effects were determined to be the shear rate-dependent lubricant viscosity and the added normal stresses of the elastic lubricant undergoing shear flow. A modified Gumbel number is presented that includes the shear rate-dependent viscosity and scales the normal stress using the Deborah number. Experimental results from testing both elastic and inelastic lubricants using a triborheometer support the use of the new modified Gumbel number in place of the traditional Gumbel number for normalizing the effects of lubricant elasticity on the Stribeck diagram. To analyze the effect of surface micro texturing on the frictional profile, step-bearing theory and assumptions about the surface/lubricant interaction are used to develop scaling parameters for the transition velocities between lubrication regimes on the Stribeck diagram. These parameters indicate how the surface texture geometry can be altered to induce or delay transition between lubrication regimes. Micro textured surfaces are fabricated using photolithography and electroless nickel plating techniques, and friction testing indicates that the new scaling parameters successfully capture the trends of the related transition velocities.

TABLE OF CONTENTS

CHAPTER 1: INTRODUCTION	11
1.1 Background.....	12
1.1.1 Viscoelastic Lubricants	13
1.1.2 Surface Micro Texturing.....	15
1.2 Work in Progress	19
1.3 Research Presented for this Doctoral Thesis.....	21
1.3.1 Overview of Thesis Work.....	21
1.4 Overview of Thesis	23
CHAPTER 2: LUBRICATION FUNDAMENTALS.....	25
2.1 The Stribeck Diagram	26
2.2 Basic Lubrication Regimes	29
2.2.1 Hydrodynamic Lubrication	29
2.2.2 Mixed Lubrication	32
2.2.3 Boundary Lubrication.....	34
2.3 Non-Newtonian Lubricants.....	36
CHAPTER 3: LUBRICANT RHEOLOGY	39
3.1 Properties of Non-Newtonian Lubricants	39
3.2 Cone-and-Plate Rheometer	40
3.2.1 Viscosity	42
3.2.2 Relaxation Time.....	47
3.3 Extensional Rheometer.....	50
3.3.1 Newtonian Fluid Filament Radius	52
3.3.2 Second-Order Fluid Filament Radius.....	53
3.3.3 Filament Profiles.....	56
3.4 CABER Testing.....	58
3.4.1 PDMS 10 Pa·s	60
3.4.2 PDMS 100 Pa·s	62
3.4.3 STP Oil Treatment.....	65
3.4.4 Valucraft Oil Additive	66
3.5 Discussion	68
CHAPTER 4: LUBRICANT ELASTICITY AND THE STRIBECK DIAGRAM....	71
4.1 Shear Rate-Dependent Viscosity.....	74
4.2 Normal Stress Distribution	77
4.3 Experimental Verification of the Modified Gumbel Number.....	83
4.4 Summary	90
CHAPTER 5: SURFACE MICRO TEXTURING	93
5.1 Calculating Load Support.....	94
5.1.1 Side Flow.....	99
5.1.2 Cavitation.....	100

5.2 Support for Cavitation Theory	101
CHAPTER 6: LOAD SUPPORT BY CAVITATION.....	103
6.1 Experimental Evidence of Cavitation	104
6.1.1 Textured Surfaces	107
6.1.2 Flat Surface	111
6.2 Numerical Investigation of Cavitation.....	114
6.2.1 Numeric Simulation of Textured Surfaces	114
6.2.2 Comparing Results with Numeric Simulation.....	117
6.2.3 Cavitation at Low Velocities.....	122
6.2.4 Influence of Radial Pressure Gradients	124
6.3 Summary	125
CHAPTER 7: MICROTEXTURING AND THE STRIBECK DIAGRAM.....	127
7.1 Exploring Texturing Parameters	128
7.2 Effect of Texture on Stribeck Diagram.....	129
7.2.1 Boundary to Mixed Regime Transition.....	130
7.2.2 Mixed to Hydrodynamic Transition	131
7.3 Results and Discussion.....	133
7.3.1 Transition from Mixed to Boundary Lubrication	135
7.3.2 Transition from Hydrodynamic to Mixed Lubrication Regimes.....	138
7.4 Optimizing Surface Texture	141
7.5 Summary	144
CHAPTER 8: CONCLUSIONS AND RECOMMENDATIONS.....	145
8.1 Lubricant Elasticity.....	146
8.2 Surface Micro Texturing.....	147
8.3 Recommendations.....	149
8.4 Final Remarks.....	151
APPENDIX A: EXPERIMENTAL SETUP AND PROCEDURES.....	161
APPENDIX B: MANUFACTURE OF TEXTURED SURFACE.....	171
APPENDIX C: SURFACE PHOTOGRAPHS AND CHARACTERISTICS.....	191
APPENDIX D: SECOND ORDER FLUID SOLUTION FOR FLUID FILAMENT BREAK-UP.....	199

LIST OF FIGURES

Figure 1.1. Examples of textured surfaces	15
Figure 1.2. Illustration of cavitation due to raised surface features.....	16
Figure 2.1. A typical Stribeck diagram illustrating the 4 main regimes of sliding lubrication	26
Figure 2.2. Illustration of the 3 main lubrication regimes in sliding friction	29
Figure 2.3. Laser profilometer scan of a flat, electroless nickel surface.....	35
Figure 2.4. Stribeck diagram showing the ability of the Gumbel number to normalize Newtonian lubricants onto a single curve.....	37
Figure 3.1. Viscosity as a function of shear rate for 5 lubricants.....	42
Figure 3.2. Carreau model and shear thinning.....	44
Figure 3.3. STP viscosity as a function of temperature and viscosity.....	44
Figure 3.4. Reduced viscosity curve for STP	46
Figure 3.5. STP moduli at 25 °C	48
Figure 3.6. Valucraft moduli at 25 °C.....	48
Figure 3.7. STP and Valucraft relaxation times.....	48
Figure 3.8. PDMS 10 Pa·s moduli at 25 °C.....	49
Figure 3.9. PDMS relaxation time.....	50
Figure 3.10. 10 Pa·s viscosity polydimethylsiloxane (PDMS) is approximated as a Newtonian fluid because the characteristic relaxation time is less than 2 ms	60
Figure 3.11. The linear profile of a 10 Pa·s PDMS melt subjected to an extensional strain using a capillary break-up rheometer (CABER).....	61
Figure 3.12. Filament thinning profile for 100 Pa·s PDMS when tested with a CABER.....	62
Figure 3.13. Elastocapillary thinning of 100 Pa·s PDMS melt.....	63
Figure 3.14. Comparison of CABER data	64
Figure 3.15. Filament thinning of STP Oil Treatment during capillary break-up testing.	65
Figure 3.16. CABER data for STP	66
Figure 3.17. CABER filament profile for Valucraft oil treatment.	67
Figure 3.18. CABER data for Valucraft oil treatment	68
Figure 4.1. Stribeck diagram showing Newtonian and viscoelastic lubricants....	73
Figure 4.2. Gap clearance in the hydrodynamic regime increases with the Gumbel number	77
Figure 4.3. Stribeck diagram of STP and PDMS30 on a flat nickel surface	84
Figure 4.4. Stribeck diagram showing G_u modified for shear rate-dependent viscosity for PDMS30 and STP	85
Figure 4.5. Stribeck diagram showing G_u modified for elasticity for PDMS30 and STP	86
Figure 4.6. Fully modified Gumbel number.....	87
Figure 4.7. Limits of α	88
Figure 4.8. Stribeck curve showing G_u and G_u' at different temperatures with STP as the interfacial lubricant.....	89

Figure 4.9. Valucraft and PDMS 60 Pa-s on flat nickel surface with modified Gumbel number	90
Figure 5.1. Micro textured surface.....	94
Figure 5.2. Illustration of cavitation in a surface hole resulting in an asymmetric pressure profile and thus positive load support.	95
Figure 5.3. 1-D representation of a cavity on a micro textured surface	96
Figure 5.4. Side flow	99
Figure 5.5. Representation of pressure profile for a surface with a cavity.....	100
Figure 6.1. Alignment fixture	105
Figure 6.2. Illustration of the beamsplitter used as a mirror to view cavitation on the textured surface.....	106
Figure 6.3. Photo of rheometer setup for cavitation visualization.....	106
Figure 6.4. Pictures showing cavitation streamers taken from video footage of a textured surface with 100 μ m holes at a 5% area density	108
Figure 6.5. 100 μ m 10% surface with cavitation streamers	111
Figure 6.6. Cavitation streamers on flat surface.....	113
Figure 6.7. Surface map for 100 μ m 5% surface	118
Figure 6.8. Pressure profile at 1.65 mm/s.....	119
Figure 6.9. Pressure map at 1.65 mm/s.....	119
Figure 6.10. Cavitation map at 1.65mm/s.....	120
Figure 6.11. Cavitation map at 1.4mm/s.....	121
Figure 6.12. Pressure profile at 1.4 mm/s.....	122
Figure 6.13. Cavitation map at 0.9mm/s.....	123
Figure 7.1. Rendering and photo of micro textured surface.....	127
Figure 7.2. Surface texturing effects for 5 different surfaces	135
Figure 7.3. Comparison of experimental data and data predicted from theory for the transition from boundary to mixed lubrication.....	136
Figure 7.4. Illustration of fluid flow over a cavity.....	137
Figure 7.5. Comparison of experimental data and data predicted from theory for the transition point from mixed to hydrodynamic lubrication.	139
Figure 7.6. Illustration of pressure profile with cavitation	140
Figure 7.7. Optimization of texturing geometry	142
Figure 7.8. Transition velocity contours	143

LIST OF TABLES

Table 3.1. The shear-thinning viscosity of non-Newtonian lubricants at 25°C....	43
Table 3.2. Temperature/rheology data for STP tested on a glass plate attached to the Peltier.	47
Table 3.3. Five modes of capillary thinning and break-up observed using the CABER.	57
Table 3.4. Rheometric properties of 4 lubricants used for CABER testing.....	59
Table 3.5. Summary of rheometric properties of lubricants that are applicable to the tribological study of the Stribeck diagram.	69
Table 6.1. Experimental and theoretical cavitation velocity for 100µm 5% surface	109
Table 7.1. Summary of the textured nickel surfaces in this study.	134

CHAPTER 1: INTRODUCTION

Friction is “a force for which there is no general explanation” [1], yet it is found nearly everywhere that motion exists. The field of tribology includes phenomena ranging from earthquakes and the geophysical flows of the Earth’s shifting crust [2] to nano-scaled friction forces that are limiting the minimum size of magnetic storage devices [3, 4]. Also included in tribology are the biological lubrication of joints and the wear properties of joint replacements [5, 6], along with the more traditional study of friction and wear of bearings and pistons.

A few major consequences of friction in a system include energy loss, leakage in seals, and system failure due to wear. A 1994 study emphasized the magnitude of energy loss due to friction when it concluded that 40% of the total fuel energy in automotive engines is consumed by engine friction [7]. When this loss is considered in association with a study on greenhouse gas emissions in California, which reports that 37% of total carbon dioxide emissions in the state in 1999 were a result of motor fuel consumed by cars and light trucks [8], there is an obvious need to explore the means of reducing this friction. In addition to energy losses, reducing system wear helps reduce the frequency by which surfaces must be replaced and therefore reduces wasted raw materials and manpower.

In terms of financial losses, AudiWorld magazine in 2004 reported the importance of friction in terms of economic value by estimating that “friction and wear-related costs in Germany lie between 2 and 7 percent of the GDP” when Germany’s GDP in 2004 was EUR 2,129 billion [9]. Similar research reported in PhysicsWorld estimates that these “direct costs of friction and wear” in many industrialized nations can amount to nearly 10% of the gross national product [10]. Although friction is “a force for which there is no general explanation” [1], it is not a force that can be ignored in the current state of technology where energy efficiency is no longer a goal but a mandate by both consumers and government.

1.1 Background

Despite the serious consequences and numbers for the losses due to friction as we know it today, tribology has been studied since 1508, when Leonardo da Vinci postulated about the relationship between applied normal force on a surface and the resulting friction force. The current state of sliding, lubricated friction was described by Ludwig Gümbel in 1914 [11]. Gümbel analyzed the results from Richard Stribeck, who ran experiments on journal bearings operated with mineral oil as the interfacial lubricant. From this data, Gümbel determined that the changes in friction observed under different running conditions could be normalized to describe the friction between a particular lubricant/surface pair using a single curve. This normalized curve was named

the Stribeck diagram, and it is used as a design tool. The system loading, sliding velocity, or lubricant viscosity can be selected in order to minimize the friction losses or to determine how to avoid component wear.

Since the development of the Stribeck diagram, both lubricant rheology and surface engineering have emerged as solutions for reducing friction in sliding, lubricated contact. Lubricants have been designed to include long polymer chains to act as viscosity modifiers as well as additives to prevent wear and corrosion. By modifying the lubricant rheology according to different operating regimes, the lubricant can be tuned to the specific friction conditions. In addition to advances in lubricant design, surfaces have been designed to include geometric patterns or to be composed of multiple materials in order to perform specialized functions. These new patterns alter the frictional characteristics of the surface to reduce energy and wear.

This thesis focuses on two of these new technologies in tribology. The underlying mechanisms are determined and described in detail here, and the consequences of each on the frictional profile of sliding, lubricated surfaces are investigated.

1.1.1 Viscoelastic Lubricants

Since the early 1900's, lubricant technology has experienced great advances and is no longer a simple Newtonian science. Mineral oil lubricants used in industrial and automotive applications have dramatically changed due to the use of viscosity index improvers (VII) and additive packages that are designed to reduce corrosion, wear, and emissions [12-14]. In addition, non-

Newtonian polymers such as Poly Alfa Olefins have been introduced as synthetic oils to accommodate more severe engine environments [13]. Outside of the automotive market, the growing micro- and nano- technology markets require highly-specialized lubricants, such as the viscoelastic perfluoropolyether boundary lubricant used in magnetic recording devices [15]. Bio-mimetic lubricants are being developed for bio-tribology applications in an attempt to replace damaged or lost cartilage and fluid in joint-replacement surgeries [16]. These new lubricants are uniquely designed, and they cannot be described by a single Newtonian fluid parameter, as given by Gümbel when he formulated the Stribeck diagram in 1914.

The importance of lubricant elasticity has been demonstrated experimentally since the 1960's [17], but more recent work has benefited from the technology to measure normal forces generated in the viscoelastic lubricants from shear flows [18]. This experimental work has been verified using viscoelastic fluid models such as the Phan-Thein-Tanner model [19] and the upper convected Maxwell model [20], but these models have been applied to very specific lubrication conditions and geometries. There is no generalized model for viscoelastic fluids that can capture the frictional profile of the lubricant-surface pair such as the Stribeck diagram, which was developed for Newtonian fluids. This generalized model is needed to allow for lubricant selection and system design without the need to develop a full-system numerical model of the surfaces and lubricant.

1.1.2 Surface Micro Texturing

In addition to altering the Stribeck diagram by using elastic lubricants, another option is to apply a micro-scale surface texture such as those shown in Figure 1.1.

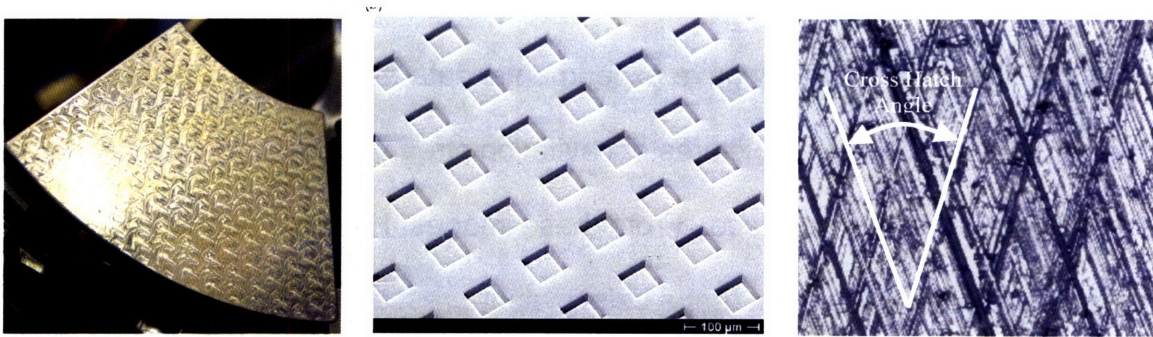


Figure 1.1. Examples of textured surfaces. From left to right: textured thrust bearing by Glavatskih and McCarthy [21], textured surface for friction and wear reduction in the boundary lubrication regime by Pettersson and Jacobson [22], and a honed engine cylinder liner by Bolander and Sadeghi [23].

Surface micro texturing first appeared in the literature in 1959 when Lewis and McCutchen published an article in *Nature* about the role that surface structure of cartilage played in lubricating animal joints [24]. This article highlighted the fact that cartilage is a sponge-like material with a micro-scale texture that can capture fluid in tiny pores. The potential for these micro-scale pores to reduce friction was finally realized for mechanical devices in 1965 [25]. Bossler showed that by glass bead peening a steel surface, it was possible to significantly reduce sliding friction in the boundary lubrication regime. He postulated that the mechanism of reduced friction was that the pores acted as lubricant reservoirs, and the exact amount of reduced friction depended strongly

on the final RMS surface roughness attained with the glass beads. From this initial research, others began experimentally exploring the effects of micro texturing.

In 1966, Hamilton and co-workers published a paper showing the effects of micro texturing in the hydrodynamic regime by designing a mechanical face seal with controlled micro texturing. The surface texturing was applied by etching copper. This paper not only gave experimental data that showed a decrease in friction, but it also showed pictures of cavitation streamers between the asperities that were etched in the surface. From these images, Hamilton suggested that pressure within the lubricant drops below vapor pressure as it moves over the asperities, causing cavitation of the lubricant and thus local pockets of lubricant vapor, as illustrated in Figure 1.2. This drop in pressure results in an asymmetric pressure profile for each individual micro-post and consequently a net normal force between the two sliding surfaces.

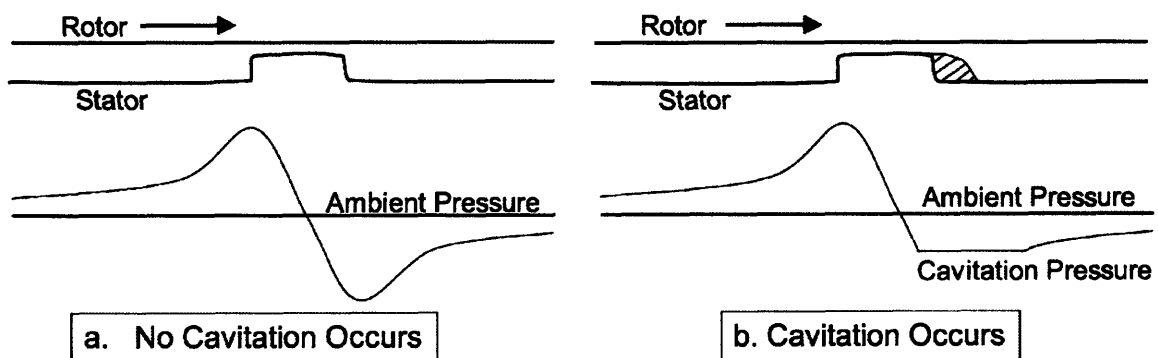


Figure 1.2. Illustration of cavitation due to raised surface features. Replicated from Hamilton et al. [26]

After realizing the benefits of surface micro texturing for altering the frictional profile for a surface/lubricant pair, subsequent publications indicate significant interest in the subject. Experimental studies often focused on optimizing texturing parameters for a particular system, and there were differing theories about the mechanisms of reduced friction. In 1989 Suh and co-workers explored the effects of surface texture in the boundary lubrication regime using titanium with channels that were transverse to the sliding direction [27]. They concluded that for the boundary lubrication regime, the surface texture acted as a reservoir to collect wear particles. Later work performed on channeled sapphire surfaces [28] and work focusing on the sheet metal forming industry [29] suggested that the mechanism of friction reduction in the boundary lubrication regime was the micro holes channels acting as lubricant reservoirs to replenished the lubricant in the contacting regions.

Cogdell and co-workers further explored experimental investigations of micro textured surfaces having an irregular surface pattern with the conclusions that the resulting friction was related to the texture depth [30], and Yu and co-workers postulated that laser-texturing a mechanical seal resulted in each pore acting as a micro-hydrodynamic bearing [31]. Other experimental investigations conclude that the texture acts as a lubricant reservoir that releases lubricant under starved conditions [32], and another explained that since the lubricant film thickness increased when texturing was applied, the lubricant flow could turn turbulent and increase hydrodynamic pressure [33]. Each experimental study was performed for a very specific application, and therefore a unified theory as to

the mechanisms of reduced friction by surface micro texturing was difficult to interpret.

Instead of investigating the effects of surface micro texturing using experimental techniques, many researchers decided to perform numerical studies. Tønder studied lubricant flow between textured surface based on a modified Reynolds number and concluded that for a simple parallel slider bearing with a textured inlet region there were two mechanism of reduced friction [34-36]. The first was a pressure build-up due to the step-bearing effect. The second method of reduced friction was that the texturing prevented lubricant from sliding out of the contact area and therefore it increased the amount of available lubricant in the critical contact area.

Brajdic-Mitidieri and co-workers presented a CFD analysis for a thrust bearing with pockets using the full Navier-Stokes equations instead of the Reynolds lubrication approximation [37]. This analysis concludes that cavitation did occur at the immediate pocket entrance at very low convergence ratios as the bearing tended toward a parallel surface. In addition, there is evidence of a “ram effect” or pressure buildup at the pocket exit, which is characteristic of a step bearing. Another analysis of a thrust bearing showed that in a theoretical study of geometries where the inlet and outlet lengths to a surface hole were not symmetric, the pressure drop in each section would also not be symmetric and therefore an asymmetric pressure profile would provide for load support [38]. This mechanism was given the term ‘inlet suction’ by Olver and coworkers to describe the flow of lubricant that results from the region of very low pressure at

the leading edge of the surface cavity. This pressure drop is also effective in situations where cavitation is not induced.

Etsion and co-workers have performed both experimental and theoretical analyses of micro textured surfaces. These application-specific studies support Hamilton's original hypothesis of friction reduction through the mechanism of cavitation and show relatively good correlation between simulation and experiments. In 1996, Etsion and Burstein presented a model for micro textured mechanical face seals based on the Reynolds lubrication equation and considering cavitation [39]. Later, Etsion and co-workers published experimental work on face seals [40], where it was compared experiments to improved numerical simulations based on the Reynolds equations and solved using a finite difference method. but laser surface texturing, as described by Etsion [41], helped researchers more concisely define other surface geometries.

1.2 Work in Progress

Surface micro texturing has been shown since Bossler's initial studies in 1965 to be an effective method of reducing friction in sliding, lubricated contacts [25], but a comprehensive study of the mechanisms by which this effect works is needed in order to optimize the frictional benefits. With an array of experimental, numerical, and theoretical investigations on these mechanisms, a unified study combining all three methods of investigation without design for a specific application is needed. In addition to altering a surface/lubricant frictional profile using surface micro texturing, viscoelastic lubricants have been developed to

improve lubrication conditions. Despite these improvements, studies have not been performed to show how to select the lubricant properties to optimize friction conditions.

Recent improvements in the technology used to measure lubricant properties at very small clearances, such as those found in lubrication flows, allow a new look at the stress experienced by surfaces sliding relative to one another. Results from non-Newtonian fluids cannot simply be interpolated to low velocities and gap heights like the results from Newtonian fluids, so the friction at lower speeds and gaps must be directly measured. In addition, micro fabrication techniques have improved to allow micro texturing of surfaces with very specific geometric patterns at scales below those attainable with macro-machining techniques. These new improvements allow a new look at the Stribeck diagram in order to expand its application for recent friction solutions.

1.3 Research Presented for this Doctoral Thesis

The research presented for this thesis provides a systematic fundamental study of lubricant elasticity and surface micro texturing in all lubrication regimes and explains the mechanism for the resulting altered frictional profile on the Stribeck diagram. In particular, the pressure distribution in the lubricant layer between sliding, textured surfaces is explored, and the effect of lubricant elasticity under these conditions is quantified. Experimental evidence is presented to verify the theoretical conclusions and assumptions.

A new dimensionless parameter is introduced that quantifies and normalizes the effect of lubricant elasticity when it is used in place of the Gumbel number on the Stribeck diagram. In addition, scaling parameters that describe the effect of different surface texture geometries on the Stribeck diagram are presented. These parameters allow optimization of surface texturing geometries for a particular lubrication regime and running conditions.

1.3.1 Overview of Thesis Work

Determining the effects of lubricant rheology and surface micro texturing on the Stribeck diagram required both an experimental and theoretical approach to the problem. Initially, a theoretical analysis was performed to determine the possible mechanisms for friction reduction. This analysis included recalling the

fundamental lubrication equations, which have already been discussed in this section, and applying the appropriate constitutive equations and flow conditions.

Once hypotheses were developed to describe the physical mechanisms for the altered friction profiles, experimental investigations were performed. All experiments were implemented using a tribo-rheometer, which is described in Appendix A. Investigation of lubricant rheology required finding weakly viscoelastic lubricants for testing and determining the properties of the lubricant using torsional and extensional rheometers. Once the rheometric properties of the lubricants were determined, friction experiments with the elastic lubricants were performed both on textured and untextured nickel plates as well as on glass plates to collect the data necessary to construct Stribeck diagrams that showed the viscoelastic trends. From these diagrams, the postulated effects of the lubricant rheology were verified.

Experimental investigation of surface micro texturing first required design and fabrication of micro textured surfaces using novel fabrication techniques to ensure consistent, repeatable surfaces with different texture geometries. The surfaces were measured to determine the exact geometric parameters, and then the coefficient of friction was determined as a function of the running conditions using the tribo-rheometer, and Stribeck curves for each surface were constructed. Once the Stribeck curves were determined, the transition points on the curves were compared with theoretical models to determine the capability of the models to capture the effects of the difference surface geometries.

From the experimental and theoretical studies of both lubricant rheology and surface micro texturing, conclusions about the effect of each parameter on the Stribeck diagram were made. These conclusions were compared to the results presented by different authors from previous experimental investigations found in the literature.

1.4 Overview of Thesis

This thesis is organized so that the introduction emphasizes the importance of tribology and describes previous research performed in determining the effect of lubricant elasticity and surface micro texturing on the Stribeck diagram. Chapter 2 presents a basic understanding of the lubrication theory used in this thesis, and the rheometric properties of the lubricants used for this study are determined and explained in Chapter 3.

After understanding the surface/lubricant pairs used in this study, theoretical and experimental work can be explored. Chapter 4 presents theory to explain the role of lubricant elasticity on the Stribeck diagram. These theories are verified experimentally using results from the triborheometer that is presented in Appendix A along with explaining the methods for testing friction using a triborhoemeter to collect data that can be used to construct a Stribeck diagram. Next, Chapter 5 discusses the theory of pressure distribution in a lubricant film for textured surfaces and hypothesizes about load support based on lubricant cavitation, and Chapter 6 verifies that cavitation is present in a lubricant film between two sliding surfaces using both experimental and numerical methods.

Chapter 7 builds on the theory developed in Chapter 5 by applying it to describe the effect of surface texturing on the Stribeck diagram. Experimental verification of this theory is also shown and discussed in Chapter 7 using surfaces fabricated using an additive method based on photolithography and electroless nickel plating. The details of the fabrication process are explained in Appendix B. All textured surfaces for this study were made using this technique. Chapter 8 summarizes the research performed on both lubricant elasticity and surface micro texturing and provides conclusions.

CHAPTER 2: LUBRICATION FUNDAMENTALS

In order to provide the reader with a basic understanding, the terminology and basic underlying principals of tribology related to the lubrication and frictional properties between lubricated, sliding surfaces are discussed. Under these conditions, there are three basic lubrication regimes that are defined based on the surface/lubricant interaction and the resulting friction coefficient. These regimes are described by Bhushan [42] as: hydrodynamic lubrication, elastohydrodynamic lubrication, and boundary lubrication. Many tribologists refer to another regime called the mixed lubrication regime. Mixed lubrication is a state that has characteristics of both boundary and hydrodynamic lubrication. The relationship between each lubrication regime and a basic understanding of the physical interaction between the surface and lubricant is best illustrated using a Stribeck diagram.

2.1 The Stribeck Diagram

The Stribeck diagram, or Reynolds-Sommerfeld curve as it is otherwise known [43], is often used to characterize sliding, lubricated friction because the running conditions for a particular surface/lubricant pair are normalized onto a single curve [44]. This diagram was defined in 1914 by Ludwig Gümbel using data collected by Stribeck. A typical Stribeck diagram with labels indicating the lubrication regimes is shown in Figure 2.1.

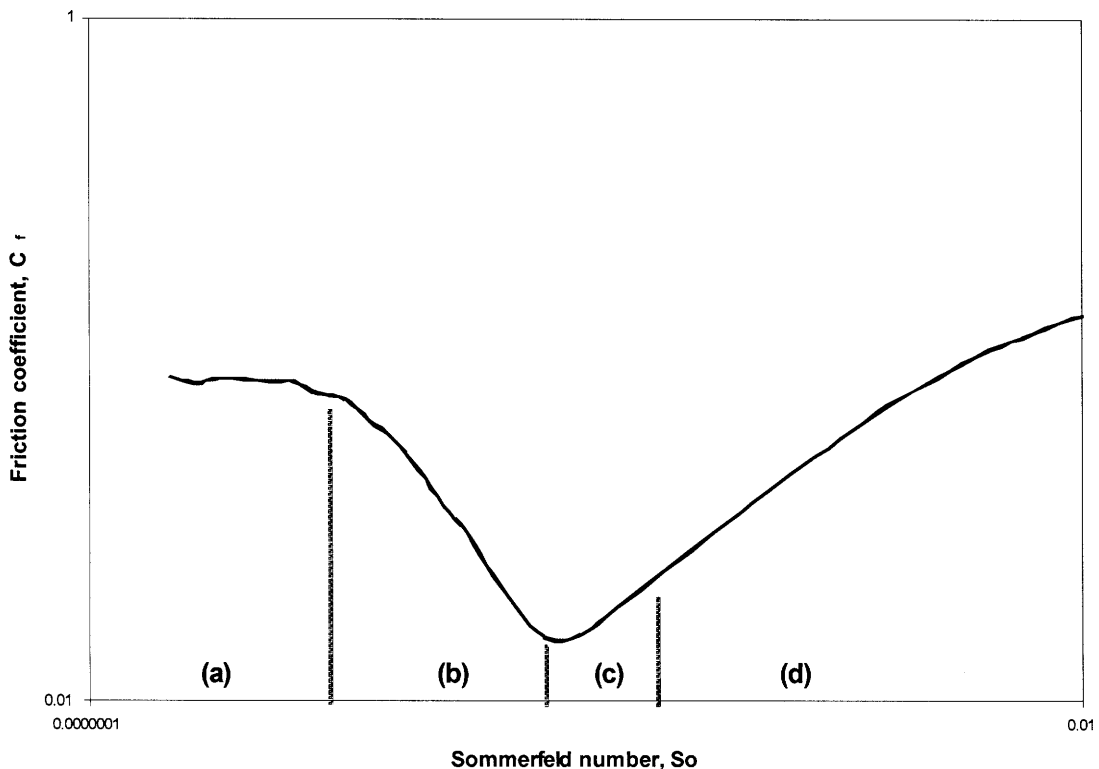


Figure 2.1. A typical Stribeck diagram illustrating the 4 main regimes of sliding lubrication. These regimes are (a) boundary lubrication, (b) mixed lubrication, (c) elastohydrodynamic lubrication (if applicable), and (d) hydrodynamic lubrication. Boundary lubrication (a) is found at lower Sommerfeld numbers where either the normal load is very high or the sliding velocity is very slow. Mixed lubrication (b) is found at moderate Sommerfeld numbers, and the characteristic dip in the Stribeck curve, is indicative of the transition from mixed to full-film lubrication (c). High Sommerfeld numbers indicate either very light normal loads or high sliding velocities, which lead to hydrodynamic lubrication (d).

The Stribeck diagram is an essential tool for design and studies in tribology, and it must be determined experimentally for a particular surface/lubricant pair. The experimental method used in this study to determine Stribeck curves is to perform an angular velocity sweep on a triborheometer with a constant normal load and variable gap height. The shearing stress (Pa) τ , required to rotate one surface across the other stationary surface is calculated from the applied torque and normalized with the normal stress (Pa) σ , or load, to get a friction coefficient, C_f .

$$C_f = \frac{\tau}{\sigma} \quad (2.1)$$

The resulting friction coefficient is plotted as a function of the Sommerfeld number, So , which is the dynamic viscosity of the Newtonian lubricant μ (Pa·s), times the linear relative speed U (m/s), divided by the normal stress per unit length P (Pa/m), assuming a constant bulk viscosity.

$$So = \frac{\mu U}{P} \quad (2.2)$$

When looking at a Stribeck diagram, boundary lubrication is characterized by a coefficient of friction that is independent of the Sommerfeld number and is found at lower Sommerfeld numbers, where either the normal load is very high or the sliding velocity is low. Mixed lubrication is found at higher Sommerfeld numbers relative to boundary lubrication, and the characteristic dip in the

Stribeck curve, such as the one shown in Figure 1, is indicative of the transition from mixed to either elastohydrodynamic lubrication or hydrodynamic lubrication depending on the surface material properties. High Sommerfeld numbers indicate either very light normal loads or high sliding velocities, which lead to hydrodynamic lubrication and the establishment of a full film of lubricant between the sliding surfaces.

In rotational systems, often the Gumbel number, Gu , replaces the Sommerfeld number [45]. The Gumbel number uses angular velocity (rad/s), Ω , instead of the sliding velocity and normal stress (Pa), σ , instead of the normal stress per unit length.

$$Gu = \frac{\mu\Omega}{\sigma} \quad (2.3)$$

Other dimensionless parameters for the Stribeck diagram include the Hersey number, which can be used for journal bearings and the Stribeck number, which describes cylinder-plane contacts. These additional parameters are discussed in detail by Cuilli [45].

One advantage of the Stribeck curve in tribology research is that the non-dimensional Gumbel or Sommerfeld numbers allow a single curve to represent the same lubricant-surface pair under varying sliding speeds and normal forces. To fully characterize the sliding frictional properties between two surfaces in lubricated contact, a complete Stribeck curve spanning all three lubrication regimes, such as that in Figure 2.1, is required.

2.2 Basic Lubrication Regimes

The three main lubrication regimes, which were indicated on the Stribeck diagram in Figure 2.1, are illustrated in Figure 2.2 and described in detail in this section. Each regime is characterized by different flow and pressure conditions, therefore the fluid mechanics for each regime must be investigated independently.

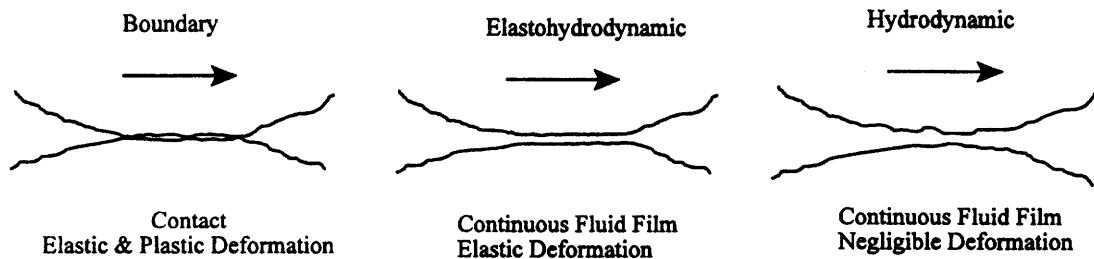


Figure 2.2. Illustration of the 3 main lubrication regimes in sliding friction [42]. Under both hydrodynamic and elastohydrodynamic lubrication, the sliding surface experiences hydrodynamic lift and is fully supported by a continuous, load-bearing film of lubricant. Elastohydrodynamic lubrication allows a force to be transmitted through the fluid and elastically deform the surfaces. Boundary lubrication results when the full film of lubricant between the two sliding surfaces breaks down and the surfaces come into contact. Tribologists also often refer to a mixed lubrication regime, which is a state that combines the properties of full-film and boundary lubrication. The fluid supports a fraction of the load, while the contacting surfaces support the remainder of the load.

2.2.1 Hydrodynamic Lubrication

Hydrodynamic lubrication is the term given to the regime where the sliding surface experiences hydrodynamic lift and are fully supported by a continuous, load-bearing film of lubricant. There is no interaction between the two surfaces, and therefore very little wear occurs. Theoretically, lift is produced as a result of a change in the distance between the two sliding surfaces, but load support for

parallel surfaces has been observed in practice and is typically assumed to be induced as a result of the surface asperities and waviness [46]. Under elastohydrodynamic lubrication conditions, there is also a continuous film of lubricant between the two surfaces, but the surfaces are loaded such that a force is transmitted through the fluid and the surfaces deform elastically under the load. Elastohydrodynamic lubrication typically occurs at either slower speeds or at higher loads than the conditions for hydrodynamic lubrication and depends on the bounding surface material characteristics.

To describe the flow and pressure distribution between sliding surfaces experiencing hydrodynamic lubrication, it is most appropriate to start with the equations of continuity and momentum for a Newtonian fluid.

In tensor form, the equation of continuity for incompressible flow with the related velocity vector v is

$$(\nabla \cdot v) = 0. \quad (2.4)$$

The second fundamental equation for this study of lubrication flow is the equation of motion that is derived from the conservation of momentum, and is written in tensor form by the equation [47]

$$\frac{\partial}{\partial t} \rho v = -[\nabla \cdot \rho v v] - [\nabla \cdot \pi] + \rho g \quad (2.5)$$

where ρ is the fluid density, π is the stress tensor, and g is the force per unit mass due to gravity. In words, this equations states that the rate of change in momentum for an arbitrary control volume is equal to the sum of the rate of momentum flux into the control volume, the rate of addition of momentum due to surfaces forces on the volume, and the rate of addition of momentum due to a

body force imposed by gravity. Other body forces such as electromagnetic forces have been neglected, but they can be added to the last term of the equation of motion.

Reynolds Equation

The continuity and momentum equations are sufficient to describe lubrication flows for Newtonian fluids, but it is more common to see them combined into a single equation called the *Reynolds equation* [42]. To attain this form of the continuity equation and equation of motion, the first step is to assume a lubrication approximation, which relates the relative importance of the distance in the sliding direction and the film thickness.

The lubrication approximation assumes that the sliding length of the lubricant film is much larger than the lubricant thickness between the sliding surfaces, so the pressure gradient across the film thickness can be neglected. This approximation also assumes that because the lubricant thickness is very small, the Reynolds number is also very low and therefore the inertial terms of the momentum equation can be neglected, which include the change of momentum and the momentum flux. In addition to neglecting these terms, the thin lubricant film is assumed to be free of body forces, so gravity is neglected. The remaining terms of the momentum equation are substituted into the across-film equation of continuity and integrated with the following boundary conditions on velocity for an orthogonal Cartesian coordinate system (x, y, z) :

$$\begin{aligned} u &= U_1, \quad w = 0, \quad \text{at } y = 0 \\ u &= U_2, \quad w = 0, \quad \text{at } y = h \end{aligned} \tag{2.6}$$

The resulting equation, called the *Reynolds equation*, gives the pressure distribution, p , in a lubricant film of thickness h for a lubricant with constant viscosity μ

$$\frac{\partial}{\partial x} \left(\frac{h^3}{\mu} \frac{\partial p}{\partial x} \right) + \frac{\partial}{\partial z} \left(\frac{h^3}{\mu} \frac{\partial p}{\partial z} \right) = 6(U_1 - U_2) \frac{\partial h}{\partial x} + 6h \frac{\partial(U_1 + U_2)}{\partial x} + 12(V_2 - V_1) \quad (2.7)$$

The Reynolds equation is only applicable in the hydrodynamic regime with rigid bounding surfaces since it only considers the fluid parameters and ignores the surface characteristics. When the surfaces are deformable, as found in elastohydrodynamic lubrication, the equations of surface material elasticity and the pressure dependence of lubricant viscosity must be coupled with this analysis [48, 49]. Excessive surface roughness can also affect the pressure distribution in lubrication flows. Patir and Cheng numerically solved the Reynolds equation for micro bearings to show that the effect of surface roughness could be modeled by obtaining the Patir-Cheng flow factors [50]. These flow factors adjust the mass flow rate of lubricant to account for surface asperity interaction with the flow.

2.2.2 Mixed Lubrication

Once the full-film of lubricant breaks down and there is surface-to-surface contact between the two sliding surface, a combination of both boundary and full film lubrication conditions must be considered. It is reasonable to assume that the sliding surfaces enter into the mixed lubrication regime when the value of the film thickness is less than or equal to the height of the tallest surfaces asperities

[51]. This transition regime between hydrodynamic lubrication and boundary lubrication is called the mixed lubrication regime.

Since surfaces are not perfectly smooth and are often characterized by mountains and valleys of micro asperities, lubricant becomes trapped in some of the lower regions on the surface and is capable of helping to sustain some of the load between the two surfaces. A statistical analysis can be performed to determine what percent of the load between surfaces the lubricant carries and what percent is sustained by the surfaces [52]. Due to the statistical distribution of roughness, as the film thickness decreases due to reduced hydrodynamic support, more asperities will come into contact until reaching boundary lubrication, where the asperities support the entire load between the two surfaces.

During the mixed lubrication regime, estimates about the percentage of surface in contact can be determined using electrical resistance techniques. These techniques, which are described by Furey [53], assume that no electrical current is passed through a full-film of lubricant, so there is infinite electrical resistance measured between the surfaces. Once the full-film breaks down, the surfaces contact and there is an electrical bridge between the two sliding surfaces. As more surface area comes into contact, the electrical resistance between the two surfaces decreases until it reaches a minimum value in the boundary lubrication regime.

2.2.3 Boundary Lubrication

Boundary lubrication results when the full film of lubricant between the two sliding surfaces no longer supports any of the applied load, and it is instead transferred to the surface asperities. The area of asperity contact is only a fraction of the apparent area because at the microscopic level, surfaces are composed of asperities that create hundreds of micro-scale peaks and valleys, as illustrated and shown in the surface profile in Figure 2.3.

Boundary lubrication is often characterized by very high friction and wear due to the intimate contact between the two surfaces. As a result of this contact, surface asperities break and reform constantly while releasing bursts of energy that often result in flash temperatures [54] along with local changes in surface contact. Along with the friction associated with the breaking of surface asperities, the broken pieces contaminate the lubricant. These wear particles lead to friction and wear by “plowing” across the surfaces [27]. The exact interaction between the surfaces combines elastic and plastic deformations as well as surface chemistry. Advanced numerical finite element models are being developed to calculate the interactions between these effects [49].

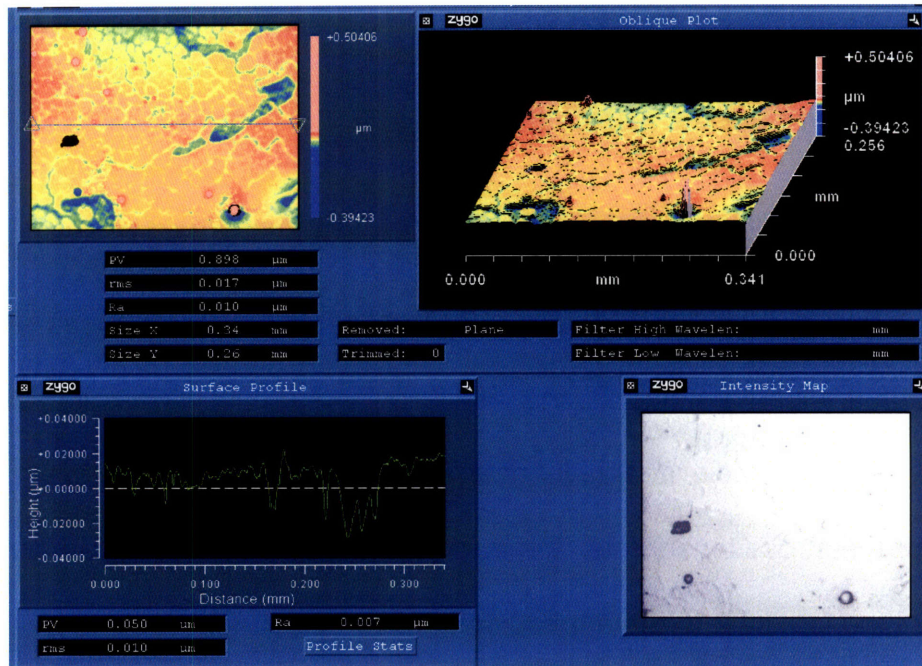


Figure 2.3. Laser profilometer scan of a flat, electroless nickel surface. Although the surface asperities are not visible, they are apparent in the surface profile scan in the lower left corner of the screen capture.

Since lubricant bulk properties are assumed to be inconsequential in this regime, much research has been performed to understand and develop boundary lubricants. These specialized lubricants interact with the chemistry of the surface to create a protective barrier layer of lubricant molecules that are partially absorbed by one or both of the contacting surfaces [55]. Currently, many boundary lubricants simply act as a sacrificial layer and only delay the onset of higher friction and wear.

2.3 Non-Newtonian Lubricants

The continuity and momentum equations are valid for all flows of incompressible fluids, but the Reynolds equation is not valid for all flows since it assumes that the lubricant has a constant viscosity and a Newtonian form of the stress tensor. For non-Newtonian lubricants, an appropriate constitutive equation for the stress tensor must be found that adequately describes the response of the lubricant to the applied conditions.

The ineffectiveness of the Stribeck diagram for describing non-Newtonian fluids is shown in Figure 2.4. Out of the four lubricants on the graph, two are non-Newtonian, and it is evident that although the Stribeck diagram is successful in normalizing the Newtonian fluids onto a single curve, it is not successful for the non-Newtonian lubricants. To further understand this discrepancy, the coefficient of friction, C_f , and the Gumbel number, Gu were defined in equations (2.1) and (2.3). These two dimensionless parameters can be successfully evaluated by determining the shear stress distribution required to rotate parallel surfaces relative to one another under a known normal force at a desired rotational velocity. Although shear stress cannot be directly measured, the shear stress is integrated to get torque, and the torque is measured directly from a torsional rheometer with a parallel-plate geometry.

Other dimensionless parameters like the Gumbel number have been developed for sliding friction with non-rotational geometries [45]. The best know

parameter is the Sommerfeld number, So , which describes linear sliding systems by replacing the rotational velocity by the sliding velocity per unit length of the sliding surface. None of these parameters, however, have addressed the need to describe the friction of systems using non-Newtonian interfacial lubricants.

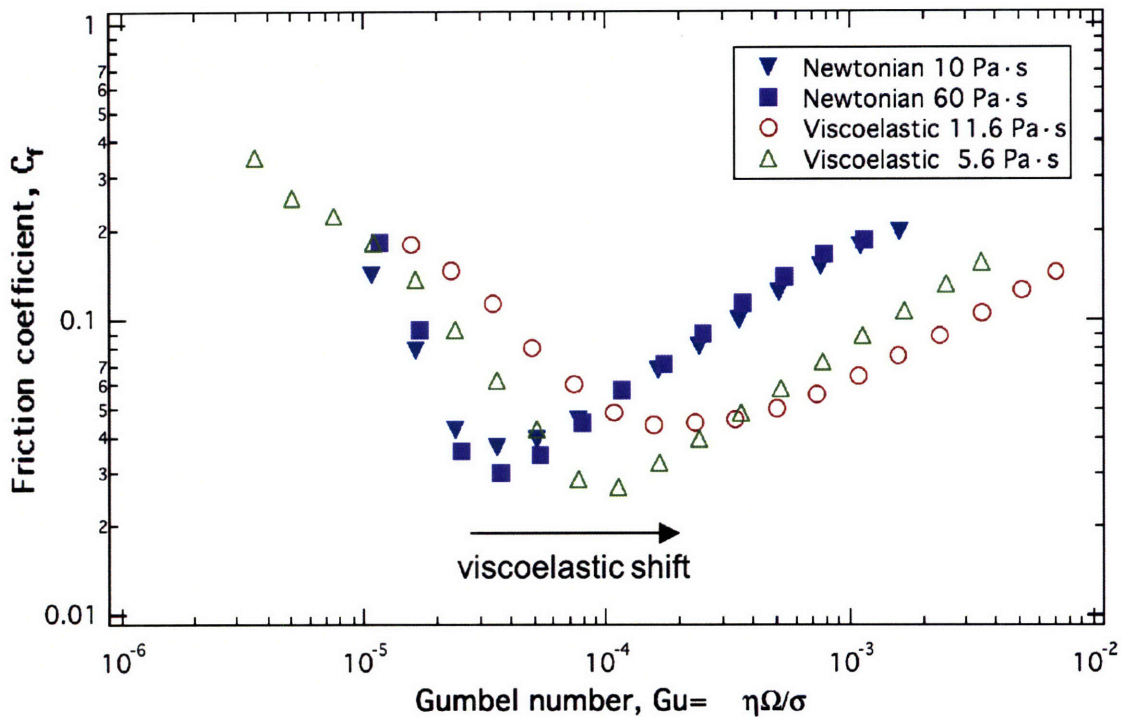


Figure 2.4. Stribeck diagram showing the ability of the Gumbel number to normalize Newtonian lubricants onto a single curve. Viscoelastic lubricants, however, are not successfully normalized. The two Newtonian lubricants are different molecular weight and viscosity PDMS melts. The 12 Pa·s viscosity lubricant is STP Oil Treatment, and the 5 Pa·s viscosity lubricant is Valucraft Oil Treatment.

Friction maps have been introduced that include non-Newtonian lubricants. One of these, which was introduced by Luengo, used an effective viscosity in place of the zero-shear rate viscosity suggested in the Gumbel number, and it replaced the normal load with the film thickness between the interacting surfaces. Despite the success of this new friction map in capturing

non-bulk effects of the lubricant, the new parameters required to create this new map are inaccessible for most non-laboratory applications. The use of basic parameters such as velocity, loading, and shearing stress make the Stribeck diagram the optimal choice for industrial and design applications where it is only important to know information such as where the minimum point of friction is located or what running conditions will keep the system in the hydrodynamic lubrication regime. Therefore, there is a need to modify the Stribeck diagram to include non-Newtonian lubricants.

CHAPTER 3: LUBRICANT RHEOLOGY

When Gmbel designed the Stribeck diagram in 1914, he used data from Stribeck's experiments that tested journal bearings lubricated with mineral oil, a Newtonian lubricant. Since the early 1900's, lubricant technology has experienced great advances and is no longer a simple Newtonian science.

3.1 Properties of Non-Newtonian Lubricants

Base oils such as mineral oil and silicone oil that have traditionally been used in tribological systems can be characterized as Newtonian fluids. These fluids have a constant viscosity and follow a simple relationship for stress τ , and strain $\delta V / \delta n$, that is linear with bulk viscosity μ , such that $\tau = \mu \delta V / \delta n$. Non-Newtonian lubricants are described as those that "have a more complex relationship between the shear stress and the velocity derivative" [56]. For this study, we will focus only on the viscoelastic properties of non-Newtonian lubricants and describe how these properties affect the Stribeck diagram.

Viscoelastic lubricants can experience shear rate-dependent viscosity, stress or strain relaxation, or both. The continuity and momentum equations described in Chapter 2 are valid for all flows of incompressible fluids, but the

Reynolds equation is not valid for all flows since it assumes that the lubricant has a constant viscosity and a Newtonian form of the stress tensor. For non-Newtonian lubricants, an appropriate constitutive equation for the stress tensor must be found that adequately describes the response of the lubricant to the applied conditions. The appropriate form of the constitutive equation for a particular fluid depends on the molecular structure of the polymer chains that make up the fluid. Exploring the non-Newtonian properties of the fluid can give insight into the appropriate form of the governing constitutive equations. The first method of exploring these properties will use a cone-and-plate viscometer, and the second method will be an extensional rheometer

3.2 Cone-and-Plate Rheometer

The cone-and-plate rheometer used for this study was the AR-G2 controlled-stress torsional rheometer by TA Instruments Inc. with an aluminum 60mm cone at a 1 degree angle. A parallel-plate configuration is described in Chapter 3 for the triborheometer, but to eliminate the radial variation in the local shear stress, the cone and plate geometry is more suitable for rheological measurements.

The relaxation time of a fluid λ , can be determined on a cone-and-plate rheometer by running a small-amplitude oscillatory shear flow test and determining the responses to the applied shear over a range of shear frequencies, ω . According to Bird et al., for a Newtonian fluid, the shear stress τ is in phase with the shear rate $\dot{\gamma}$ [47], but for viscoelastic fluids, the response

to an oscillatory shear rate input has both an in-phase and out-of-phase component and can be written in terms of the material functions G' (storage modulus) and G'' (loss modulus) such that

$$\tau = -G'(\omega)\gamma^0 \sin \omega t - G''(\omega)\gamma^0 \cos \omega t \quad (3.1)$$

The fluid relaxation time can be defined according to the Maxwell model, which has the following general constitutive equation relating the stress tensor in the fluid to the applied strain rate tensor

$$\lambda \frac{\partial \tau}{\partial t} + \tau = -\eta \dot{\gamma} \quad (3.2)$$

Substituting the shear stress and partial time derivative of the shear stress from equation (3.1) into the Maxwell model for an applied shear stress γ^0 , the resulting equation gives the relaxation time as

$$\lambda(\omega) = \frac{G'}{G''\omega} \quad (3.3)$$

The characteristic relaxation time for a fluid is defined as the limit of the relaxation time as the frequency ω goes to zero.

3.2.1 Viscosity

The steady shear viscosities of five lubricants used in this research are shown in Figure 3.1. The viscosity was determined by testing the fluids using a cone-and-plate geometry on a torsional rheometer at 25 degrees Celsius.

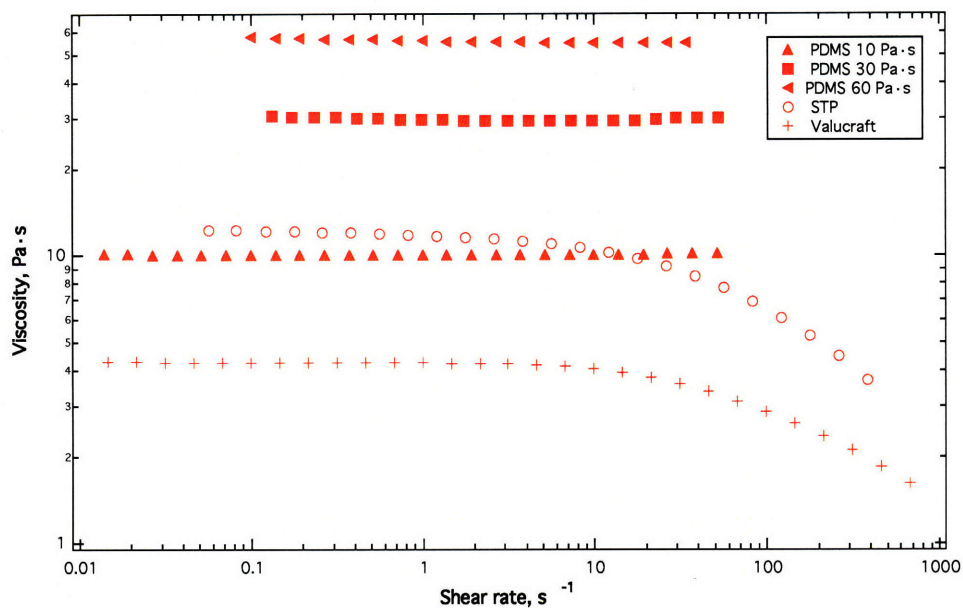


Figure 3.1. Viscosity as a function of shear rate for 5 lubricants. Data collected from a controlled-stress rheometer (AR-G2) shows the shear rate dependence of STP and Valucraft while illustrating that PDMS is a constant-viscosity fluid.

Three different molecular weight polydimethylsiloxane (PDMS) melts are shown in Figure 3.1, and they are described by their respective viscosities. At low molecular weights, PDMS can be well described as a Newtonian fluid, so it is independent of shear rate. At low shear rates, higher molecular weight PDMS melts are also independent of shear rate, but they exhibit other non-Newtonian characteristics, as it will be shown in the subsequent sections. STP and

Valucraft are commercial oil additives that have proprietary chemical compositions and fluid properties. As illustrated in Figure 3.1, these lubricants are shear-thinning at high shear rates.

To characterize the shear-thinning properties of STP and Valucraft, the experimental data can be fit to a Carreau model for the lubricant viscosity η

$$\frac{\eta - \eta_{\infty}}{\eta_0 - \eta_{\infty}} = \left[1 + (\lambda \dot{\gamma})^2 \right]^{(n-1)/2} \quad (3.4)$$

As described by Bird [47], this is a four-parameter empirical model that describes the zero-shear-rate viscosity η_0 in the low to zero-shear region, the infinite-shear-rate η_{∞} in the very high, asymptotic shear region, and the “power law exponent” n that describes the slope and transition into the “power-law regime”. The time constant λ characterizes the natural time scale of the fluid. The inverse of the time constant can be used to approximate the shear rate below which the fluid has a constant viscosity equal to the zero-shear-rate viscosity.

Using the commercial Rheology Advantage software, the Carreau model is fit to the viscosity data collected from the torsional rheometer. The resulting fit parameters are given in Table 3.1, and both the data and model are plotted in Figure 3.2 for the two shear-thinning lubricants.

Table 3.1. The shear-thinning viscosity of non-Newtonian lubricants at 25°C. These lubricants can be described by the Carreau model with the 4 fitting parameters given in the table.

	η_0 (Pa·s)	η_{∞} (Pa·s)	λ (s)	n
STP	11.6	1.8×10^{-6}	0.076	1.34
Valucraft	4.2	1.1×10^{-5}	0.044	1.27

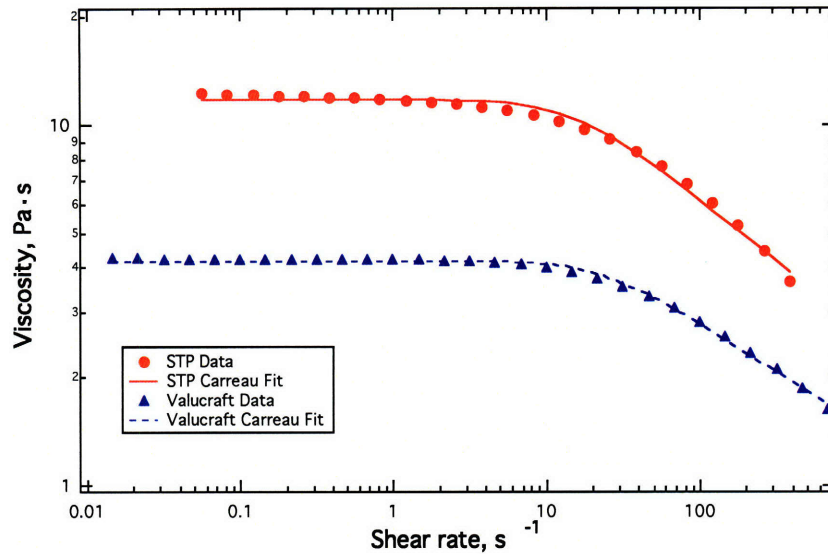


Figure 3.2. Carreau model and shear thinning. The shear-thinning viscosity of STP and Valucraft can be estimated using the 4-parameter empirical Carreau model.

In addition to being shear rate-dependent, both lubricant dependent viscosity and relaxation time are also temperature-dependent. The viscosity of STP is shown in Figure 3.3 as a function of temperature and shear rate.

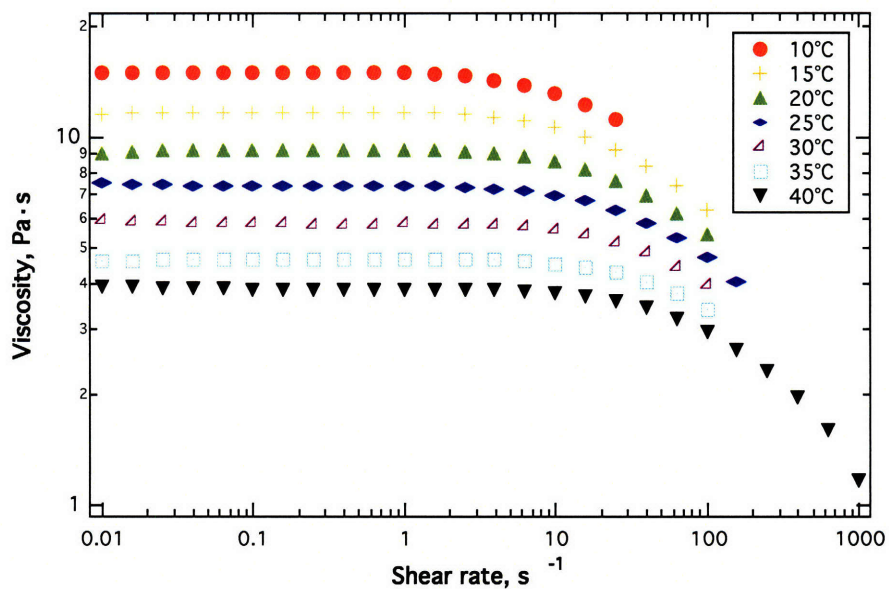


Figure 3.3. STP viscosity as a function of temperature and viscosity. Both lubricant viscosity and relaxation time are temperature-dependent. Data shown here is collected using a cone-and-plate geometry tested on a glass plate. The temperature shown is the Peltier temperature and not the temperature of the lubricant.

The viscosity curves in Figure 3.3 can be reduced onto a single master curve using the “method of reduced variables” described by Bird et al. [47]. This method selects an arbitrary reference temperature T_0 and calculates a reduced viscosity η_r , and reduced shear rate $\dot{\gamma}_r$, based on a shift factor a_T . This shift factor can be determined from experimental data, or it can be calculated using methods based in molecular theory. Due to the large amount of data available for this study, a_T is determined experimentally using the equation

$$a_T = \frac{\eta_0(T)T_0\rho_0}{\eta_0(T_0)T\rho} \quad (3.1)$$

for the current study, the density ratio is small because of the very small range of temperatures studied. It was therefore neglected in the actual calculation of the shift factor. The reference temperature T_0 is set at the standard operating temperature of 25°C. The reduced viscosity curve for each temperature is calculated from the equation

$$\eta_r = \eta(\dot{\gamma}, T) \frac{\eta_0(T_0)}{\eta_0(T)} \quad (3.2)$$

and plotted with the reduced shear rate for each temperature, which can be found using the following equation

$$\dot{\gamma}_r = a_T \dot{\gamma} \quad (3.3)$$

The resulting reduced-viscosity graph is shown in Figure 3.4.

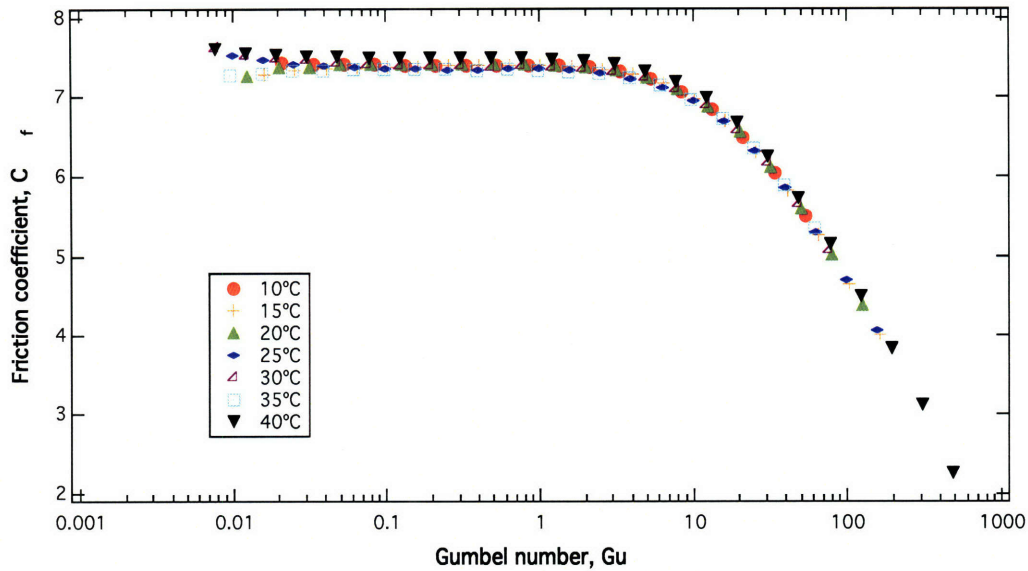


Figure 3.4. Reduced viscosity curve for STP. The “method of reduced variables” described by Bird et al. [47] allows viscosity data to be reduced to a single curve using a shift factor that can be determined experimentally.

The advantage of this master curve is that viscosity data collected at 40°C can be used to estimate the viscosity at other temperatures. Due to torque restrictions, the cone and plate torsional rheometer used for this study was only able to shear the lubrication to a maximum shear rate of 158 s^{-1} at 25°C. The lubricant viscosity is reduced by half from 25°C and 40°C, so the limiting shear rate at 40°C is higher than that at the lower temperatures. Therefore a larger portion of the shear-thinning region can be explored using the method of reduced variables for viscosity.

Table 3.2 gives the relaxation time and Carreau variables for STP when tested on a glass plate attached to the Peltier, with the Peltier temperature ranging from 10 to 40 degrees Celsius. The temperature of the lubricant is not identical to that of the Peltier plate due to thermal losses through the glass and layer of paraffin used to attach the glass.

Table 3.2. Temperature/rheology data for STP tested on a glass plate attached to the Peltier.

Peltier Temp. T (°C)	η_0 (Pa·s)	η_∞ (Pa·s)	λ (s)	N
10	15.92	1.67×10^{-4}	0.100	0.31
15	11.68	2.99×10^{-5}	0.060	0.35
20	8.52	3.20×10^{-5}	0.057	0.28
25	7.53	4.90×10^{-6}	0.042	0.31
30	5.85	2.39×10^{-5}	0.035	0.29
35	4.72	2.89×10^{-6}	0.026	0.31
40	3.78	2.08×10^{-5}	0.023	0.29

3.2.2 Relaxation Time

The lubricant relaxation time was determined from the linear viscoelastic moduli. Figure 3.5 shows a graph of these moduli as a function of angular frequency for STP, and Figure 3.6 the graph of the storage and loss moduli for Valucraft. Along with determining the relaxation time from the Maxwell model theory, it can also be estimated as the inverse of the frequency at the location at which the data for the storage modulus would intersect the data for the loss modulus if the linear section of the lines were superimposed to higher shear rates. Qualitatively, it appears that the graph of the STP moduli would intersect at a lower frequency, which indicates a faster relaxation time. The relaxation time can be better calculated from equation (3.3), where the characteristic

relaxation time for the fluid is estimated to be the limit of time at which the frequency goes to zero. Figure 3.7 shows the relaxation times for STP and Valucraft.

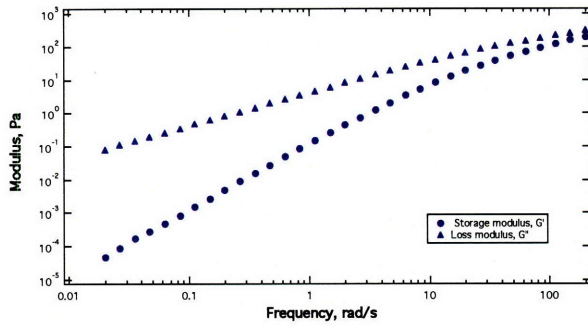


Figure 3.5. STP moduli at 25 °C

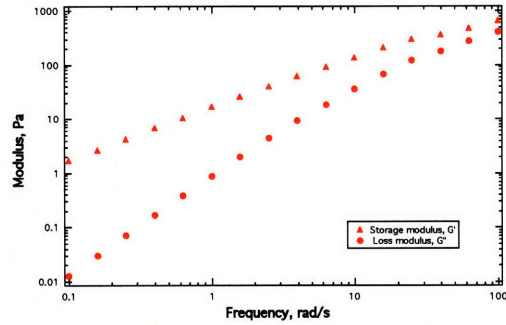


Figure 3.6. Valucraft moduli at 25 °C

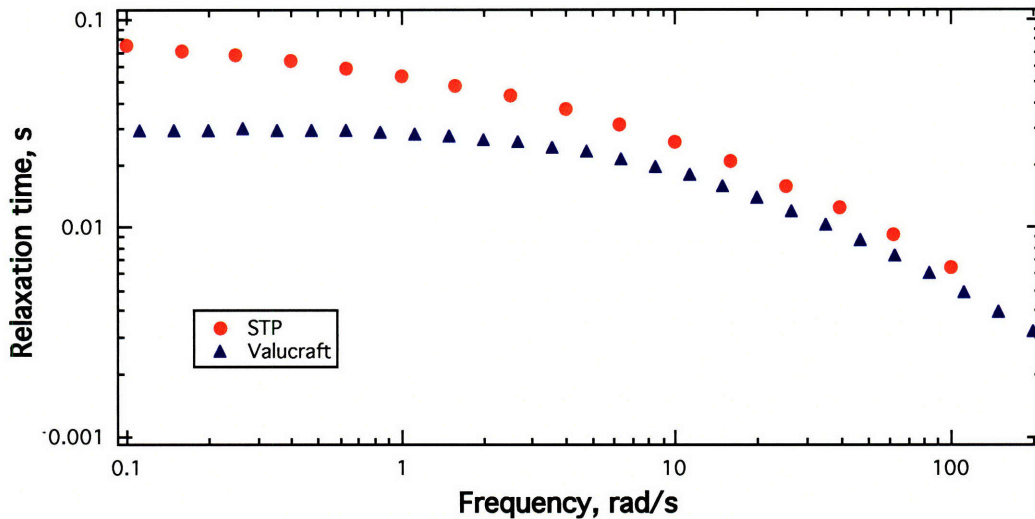


Figure 3.7. STP and Valucraft relaxation times. The relaxation time is defined according to the Maxwell model, and the characteristic relaxation time for a fluid is the limit at which the frequency approaches zero.

At low molecular weights, PDMS melts are approximated as Newtonian fluids, but as the molecular weight increases, these polymers exhibit a higher level of viscoelastic response. As a Newtonian fluid, the graph of the storage and loss moduli as a function of frequency should be two parallel lines that never

cross. Figure 3.8 shows 65,000 molecular weight PDMS, also known by its dynamic viscosity as PDMS 10 Pa·s. It is not a perfectly Newtonian fluid since the lines are not exactly parallel, but they can be estimated to cross only at a very high angular frequency. When the relaxation times are calculated, Figure 3.9 illustrates how the times are insignificantly small at very low molecular weights, but the relaxation time increases according to the molecular weight.

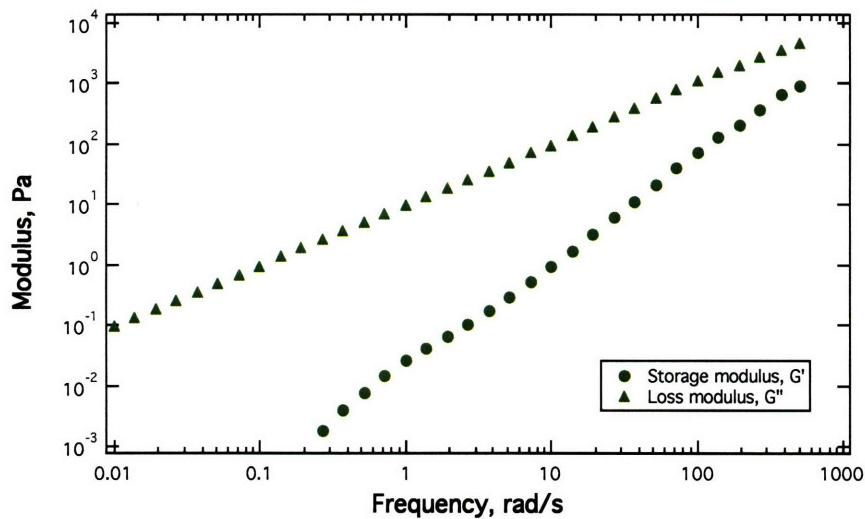


Figure 3.8. PDMS 10 Pa·s moduli at 25 °C. The two moduli do not intersect until high frequencies, indicating a low relaxation time and minimal elasticity.

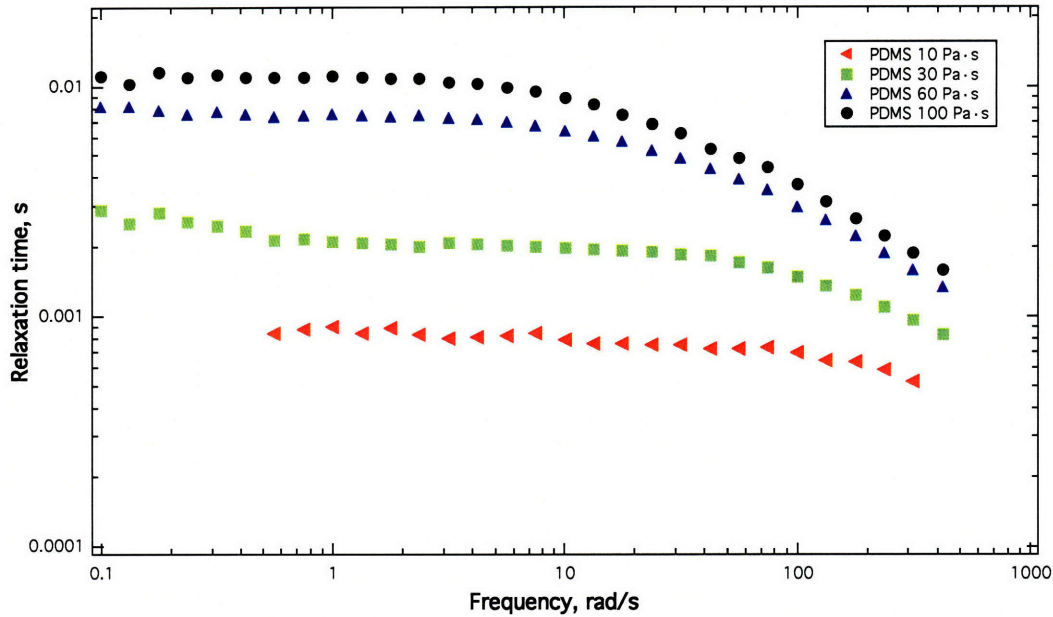


Figure 3.9. PDMS relaxation time. As molecular weight of PDMS decreases, the relaxation time becomes decreasingly significant.

3.3 Extensional Rheometer

The extensional rheometer used for this study was a capillary break-up rheometer (CABER) that was designed to apply a uniaxial elongational flow to a fluid and measure the resulting filament radius as a function of time. Along with determining the extensional viscosity and fluid characteristic relaxation time, this measurement can be used to give insight into the appropriate constitutive model that should be used to describe the viscoelastic fluid. Because the use of an extensional rheometer is somewhat unique for tribology applications, it will be described here in detail.

The appropriate solution for the capillary break-up of a Newtonian fluid is relatively straightforward [57] and will be explained here briefly. For a capillary

break-up system where there is an initial near-instantaneous strain imposed on the fluid, the driving force to break the elongated thread of fluid on small scales in the absence of inertial effects is surface tension, σ . An axial force balance that neglects gravity leads to the expression

$$\pi R^2(p + \tau_{zz}) = 0 \quad (3.4)$$

where R is the thread radius, p is the external fluid pressure, and τ_{zz} is the axial stress. Next, a radial force balance solves for the external fluid pressure

$$p = p_a + \frac{\sigma}{R} - \tau_{rr} \quad (3.5)$$

If p_a is the gauge pressure, then it can be set to zero and equations 1 and 2 are equated to give the extensional stress difference as a function of surface tension and radius

$$(\tau_{zz} - \tau_{rr}) = -\frac{\sigma}{R} \quad (3.6)$$

To solve for the kinematics of the flow, the previous assumptions for neglecting inertia and gravity as well as assuming a cylindrical cross-section lead to the flow conditions of a pure uniaxial extensional flow. A mass balance sets the initial cross-sectional area of the thread times a differential height equal to the instantaneous cross-sectional area of the thread times the new differential height. Differentiating with respect to time, t , leads to the axial strain rate, $\dot{\epsilon}$

$$\begin{aligned}
v_z = \dot{\epsilon}z &= \frac{dz}{dt} \\
\frac{dz}{dt} &= \left(-\frac{2}{R} \frac{dR}{dt} \right) dz \\
\dot{\epsilon} &= \left(-\frac{2}{R} \frac{dR}{dt} \right) \tag{3.7}
\end{aligned}$$

3.3.1 Newtonian Fluid Filament Radius

For a Newtonian fluid, the extensional stress difference given by equation (3.6) is equal to the extensional viscosity η_E , multiplied by the axial strain rate. Since the extensional viscosity is equal to three times the Newtonian viscosity μ [58], this leads to

$$-\frac{\sigma}{R} = -3\mu\dot{\epsilon} = -\frac{6\mu}{R} \frac{dR}{dt} \tag{3.8}$$

This result for the radius of a Newtonian fluid undergoing capillary break-up is a linear equation with the following solution for the filament radius at a given time and initial radius, R_0

$$R = R_0 - \frac{\sigma}{6\mu} t \tag{3.9}$$

The analysis so far has assumed that the filament is cylindrical and any changes in the filament diameter occur gradually and are negligible. This assumption is not valid near the end plates where the filament diameter changes rapidly since the liquid covers the entire surface of the plate. Detailed analyses of the end-plate effects have been performed, and correction factors have been

introduced from numerical and similarity solutions of the problem. A summary of these papers is given by McKinley and Tripathi [57]. In order to include these effects into the analysis, we will add the correction variable X to the capillary stress term and analyze how the correction factor introduced by Papageorgiou [59] fits with our experimental data. The equation for the radius of a Newtonian fluid in extensional flow including the suggested correction factor, $(2X-1)$, is

$$R = R_0 - \frac{(2X-1)\sigma}{6\mu}t \quad (3.10)$$

3.3.2 Second-Order Fluid Filament Radius

In order to predict the filament radius of a viscoelastic fluid, a constitutive equation for the fluid behavior must be assumed and then compared with experimental profiles. A complete discussion of the thinning of polymer solutions is given by McKinley [60], but only the second-order-fluid solution will be developed here.

For weakly viscoelastic fluids undergoing elongational flow, we cannot simply assume that the extensional stress difference is equal to that of a Newtonian model. Instead, we must choose a constitutive equation to relate stress to strain rate. For this analysis of a weakly viscoelastic fluid, we will determine a solution for a second-order fluid (SOF). A SOF is characterized by the generation of normal stress in pure shear, but there is very little shear thinning of the fluid until high shear rates.

To model the SOF, a retarded motion expansion is simplified by assuming steady, homogeneous, and irrotational flow to yield a Reiner-Rivlin model. A formal statement of the equation for the Reiner-Rivlin model can be found in Bird on page 504 [47]. For our capillary break-up analysis, we formulate our constitutive equation by taking advantage of the fact that if the flow is irrotational. The velocity gradient is this symmetric and identically equal to its transpose, leading to

$$\gamma_{(n)} = (-1)^{n+1} \gamma_{(1)}^n \quad (3.11)$$

This can be substituted into the retarded motion expansion, and when the equation is limited to second-ordered terms, the resulting equation, with $\gamma_{(1)} = \dot{\gamma}$, is

$$\tau = -[b_1 \dot{\gamma} + (b_{11} - b_2) \dot{\gamma}^2] \quad (3.12)$$

The strain rate tensors for a fluid undergoing uniaxial elongational flow can be found in Appendix C of Bird et al. [47]. Using these tensors, the extensional stress difference in terms of the constant axial strain rate is found to be

$$-\frac{(\tau_{zz} - \tau_{rr})}{\dot{\epsilon}} = 3b_1 + 3(b_{11} - b_2) \dot{\epsilon} \quad (3.13)$$

The zero-shear rate viscosity can be substituted for b_1 while the difference $(b_{11} - b_2)$ can be replaced with an extensional constant, b_E . Substituting the extensional stress difference from equation (3.6) into equation (3.13) and including the correction factor for the end plates, the resulting capillary force/strain rate equation is

$$\frac{(2X-1)\sigma}{6R(t)} = (3\eta_0 + 3b_E \dot{\epsilon}) \dot{\epsilon} \quad (3.14)$$

Replacing the axial strain rate with equation (3.7) gives a nonlinear ordinary differential equation in dR/dt

$$\frac{(2X-1)\sigma}{6R} = \left\{ 3\eta_0 + 3b_E \left(-\frac{2}{R} \frac{dR}{dt} \right) \right\} \left(-\frac{2}{R} \frac{dR}{dt} \right) \quad (3.15)$$

The solution for this equation is given in Appendix D for the initial condition that at time equal to zero, the filament radius is equal to the end plate radius. The result is two equations that can be used to model the filament radius of a second-order fluid in extensional flow. These equations are

$$y = \sinh^{-1} \left(3\eta_0 R / 4(2X-1)\lambda\sigma \right) \quad (3.16)$$

$$\frac{1}{2} (e^{2y} - 1) + y = \frac{(t_c - t)}{2B} \quad (3.17)$$

where λ is the relaxation time of the fluid, t_c is the time at which the filament breaks, and $B = (\lambda\sigma/3\eta_0 R_0)$. For times close to breakup where $y \ll 1$, the radius decays with time as

$$R(t) \approx \frac{(2x-1)\sigma}{4B} \frac{\sigma}{b_E} (\hat{t}_c - \hat{t})^2 \quad (3.18)$$

for

$$t = \frac{\hat{t}\sigma}{6\eta_0 R_0} \quad (3.19)$$

3.3.3 Filament Profiles

Although only 2 fluid models have been developed to describe the filament evolution of a fluid undergoing capillary thinning, a number of models can be developed in the same way using different constitutive equations. A summary of “the most commonly-observed modes of capillary thinning and break-up” are illustrated in Table 3.3, which is a replication of a chart from McKinley [60].

Table 3.3. Five modes of capillary thinning and break-up observed using the CABER. Replicated from McKinley[60].

Bingham Plastic	Power Law Fluid	Newtonian	Weakly Elastic Fluid	Elastic Fluid
$\frac{R_{mid}(t)}{R_0} = \frac{\sigma/R_0}{\sqrt{3}\tau_c} \left[1 - \exp\left(-\frac{\tau_c(t-t_c)}{2\sqrt{3}\mu}\right) \right]$	$\frac{R_{mid}}{R_0} = \Phi(n) \frac{\sigma}{K} (t_c - t)^n$	$\frac{R_{mid}}{R_0} = 0.0709 \frac{\sigma}{\eta_s R_0} (t_c - t)$	$\frac{R_{mid}}{R_0} \approx \frac{\sigma}{48b_E R_0} (t_c - t)^2$	$\frac{R_{mid}}{R_0} = \left(\frac{GR_0}{2\sigma}\right)^{1/3} \exp(-t/(3\lambda_1))$
<p>Critical radius for yield and onset of capillary-driven flow is: $R < R_c = \sigma/\sqrt{3}\tau_c$</p> <p>Close to break-up, when viscous effects dominate, the radius decreases linearly in time.</p>	<p>The front factor Φ must be determined numerically (Doshi et al. 2003):</p> <p>$\Phi_{1/3} \approx 2^{-n/3}$</p> <p>$\Phi_{non} = 0.071 + 0.239(1-n) + 0.548(1-n)^2 + O(1-n)^3$</p>	<p>The front factor is determined from the similarity solution for Stokes flow (Papageorgiou, 1995):</p> <p>$t_c = 14.1 \eta_s R_0 / \sigma$</p>	<p>The Second-Order Fluid model gives:</p> <p>$\eta_E = 3\eta_0 + 3b_E \dot{\epsilon} + \dots$</p> <p>where:</p> <p>$b_E = (-b_2 + b_{11}) > 0$</p> <p>$t_c = \sqrt{48(b_{11} - b_2) / \sigma}$</p>	<p>Homogeneous extensional flow with $Wi = \lambda_1 \dot{\epsilon} = 2/3$. Filament does not break without considering finite extensibility of polymer chain:</p> <p>$t_c \approx 3\lambda_1 \ln \left[\frac{4}{3} I^2 (GR_0 / \sigma)^{4/3} \right]$</p>

In order to determine the appropriate constitutive equations for the lubricants used in this study, the rheometric properties were determined from the torsional rheometer so that the magnitude of the elastic effects could be determined. In addition, the filament profiles were found from experiments with the CABER then compared to the common modes of breakup shown in Table 3.3 in order to determine the appropriate constitutive models for the lubricants.

3.4 CABER Testing

In order to experimentally determine the appropriate constitutive models for the different lubricants in this study, they were tested using a CABER. The testing procedures for this device are described in detail by Rodd and coworkers [61] but will be briefly described here.

In order to estimate only the effects of capillary thinning on the fluid, a small, cylindrical column of fluid is placed between two parallel steel plates that are 2mm in diameter and approximately 2mm apart. The exact distance between the plates is based on the capillary length $\ell_{cap} = \sqrt{\sigma/\rho g}$, in order to improve boundary condition approximations and is discussed by Rodd and coworkers. When the test begins, a spring forces the plates apart instantaneously to simulate a step-strain, and the filament radius thins with time due to capillary forces. A digital micrometer within the device measures the evolution of the

radius with time, and an external camera records the profile of the stretched filament.

The data can be compared to Table 3.4 in order to determine the mode of capillary thinning, but in order to develop models for the filament radius, the lubricant viscosity, density, surface tension, and relaxation time must be known. The viscosity and relaxation time have been previously measured with the torsional rheometer, so the surface tension was measured with a tensiometer using a ring configuration, and the density was measured with a densitometer. A summary of the rheometric properties of the fluids measured with CABER is given in Table 3.4.

Table 3.4. Four lubricants are tested to determine their modes of capillary thinning and break-up. The rheometric properties of these fluids were determined using a tensiometer to measure surface tension, a densitometer to measure fluid density, and a constant-stress torsional rheometer to determine the viscosity and relaxation time.

Fluid	Viscosity (Pa·s)	Density (kg/m³)	Surface tension (mN/m)	Relaxation time (s)
PDMS 10 Pa·s	10	974	19.9	< 0.002
Valucraft (VC)	4.2	899	32.6	0.029
STP	11.6	879	29.3	0.076
PDMS 100 Pa·s	100	977	20.0	0.012

3.4.1 PDMS 10 Pa·s

Although PDMS is an elastic polymer melt, for molecular weights below 100,000 g/mol (viscosity of approx. 30 Pa·s at 25 °C), the relaxation time for the fluid is less than 2ms, which is small enough that it can be approximated as Newtonian fluid. This assumption will be verified experimentally for elongational flows. The viscosity of the fluid was determined using a controlled-stress torsional rheometer by testing the viscosity over a range of shear rates. Figure 3.1 shows that the PDMS melt does not shear-thin within the given limits of the shear rate.

Figure 3.10 shows a progression of images taken during the capillary break-up of a 10 Pa·s viscosity PDMS melt, which can be approximated as a Newtonian fluid. These images should be compared to the profile of a Newtonian fluid in Table 3.3. Notice that there is always an hour-glass-shaped filament rather than one where a constant-radius filament connects the top and bottom reservoirs.

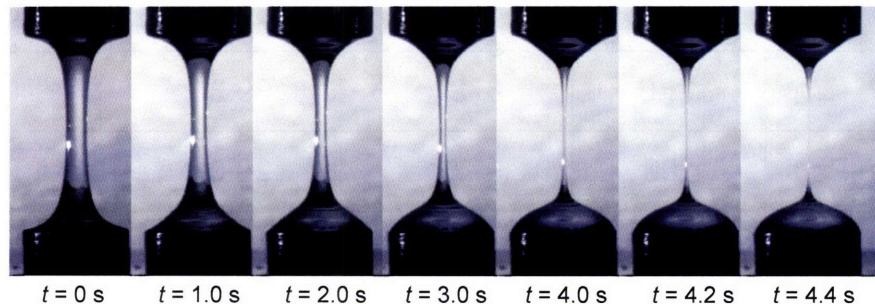


Figure 3.10. 10 Pa·s viscosity polydimethylsiloxane (PDMS) is approximated as a Newtonian fluid because the characteristic relaxation time is less than 2 ms. This sequence of photos shows the PDMS melt undergoing capillary break up. The filament profile can be compared to that of a Newtonian fluid.

If PDMS is modeled as a Newtonian fluid, then when PDMS is subjected to extensional shear the filament radius is expected to decrease linearly with time, as shown in equation (3.10). The midpoint radius is plotted as a function of time in Figure 3.11. Notice that after the initial stretching occurs, the slope of the line is nearly constant until the filament breaks. Given the rheometric properties of the PDMS melt from Table 3.4, if we take the slope of the line to be only the ratio of surface tension to viscosity, then the slope should be -3.8mm/s . The actual slope of the line for the decreasing PDMS filament radius is calculated to be -0.28mm/s , so we must include the correction factor for the end plates in our calculation. The Papageorgiou estimate of 0.0709 [59] results in a slope of -0.27mm/s , which is in good agreement with our experimental results.

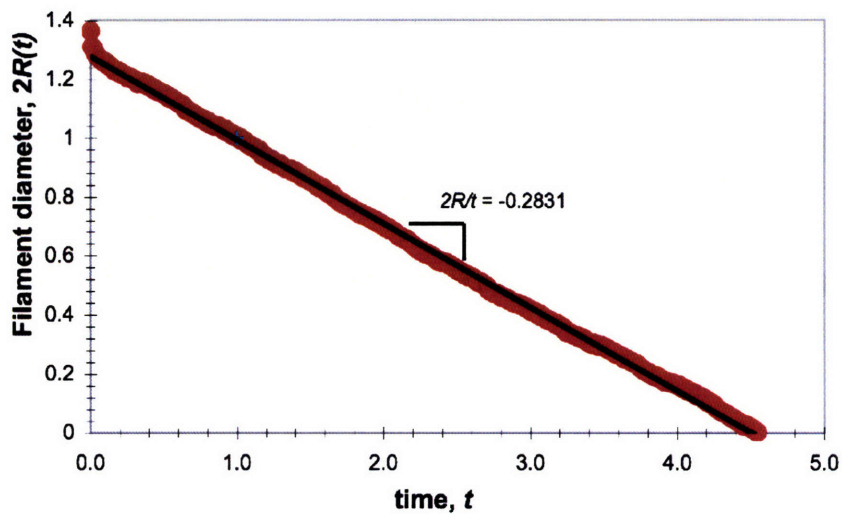


Figure 3.11. The linear profile of a 10 Pa-s PDMS melt subjected to an extensional strain using a capillary break-up rheometer (CABER) indicates that the polymer can be modeled as a Newtonian fluid.

3.4.2 PDMS 100 Pa·s

As the molecular weight of the PDMS melt increases, the fluid becomes both more viscous and more elastic, as shown in Figure 3.1 and Figure 3.9. In order to determine the appropriate constitutive model for the increased elastic effects in the fluid, we can first qualitatively compare the filament profiles shown in Table 3.3 to the filament profile images from CABER testing of 100 Pa·s viscosity PDMS shown in Figure 3.12. The distinct hourglass shape indicates that the fluid acts like a power-law fluid under extensional flow.

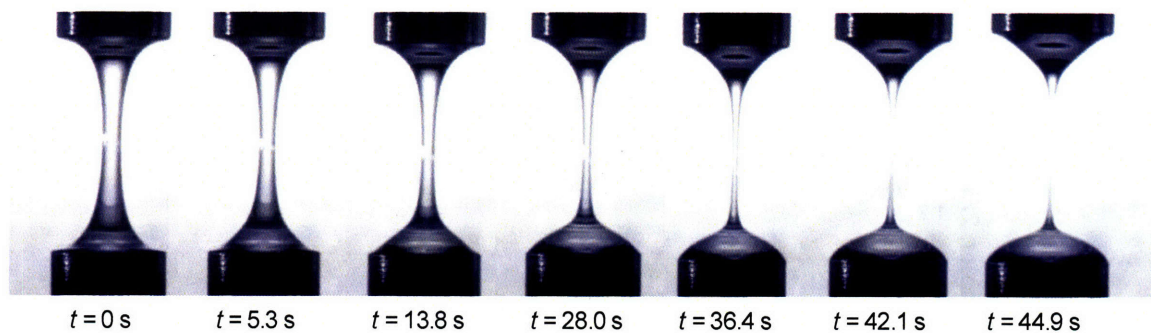


Figure 3.12. Filament thinning profile for 100 Pa·s PDMS when tested with a CABER.

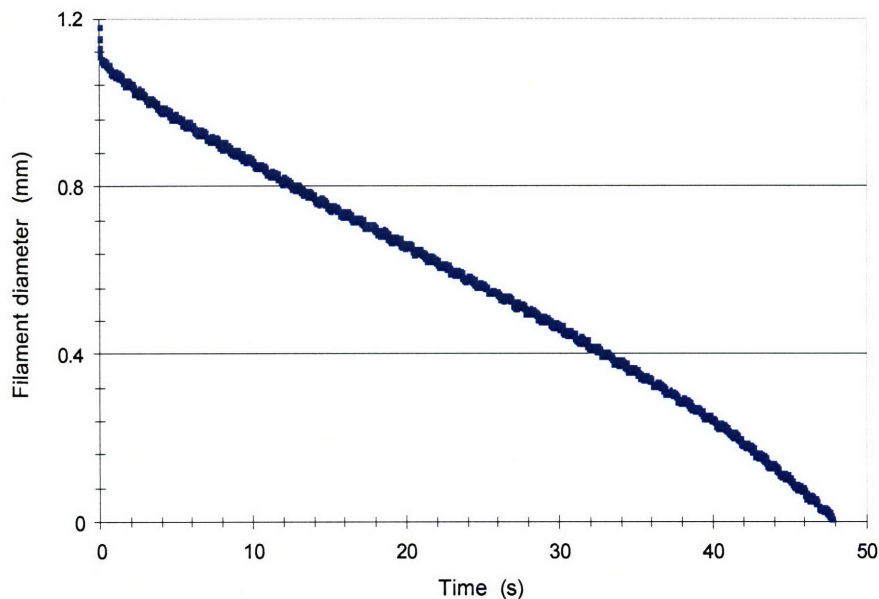


Figure 3.13. Elastocapillary thinning of 100 Pa·s PDMS melt. The increasingly negative slope indicates that this polymer could be modeled as a power law fluid.

Another method of determining the appropriate model for the extensional flow of a polymer is to look at a graph of the filament midpoint radius as a function of time. We have already seen that for the low molecular weight PDMS solutions, the graph of diameter versus time was linear and therefore the polymer melt could be approximated with a Newtonian model. Figure 3.13, however, shows that the diameter versus time graph for data from a 100 Pa·s viscosity PDMS melt (the highest molecular-weight solution tested), is not linear. Instead, the slope of the line is approximately linear for short times, and then the slope becomes more negative as the filament thins. This effect is indicative of a power law fluid since all other models shown in Table 3.3, with the exception of the Bingham plastic model, have a slope that becomes less negative with time.

Figure 3.14 shows a plot of diameter versus time for each of the four PDMS melts tested. The change in slope is increasingly evident with the two highest viscosity fluids, which indicates that the elastic effects increase with molecular weight.

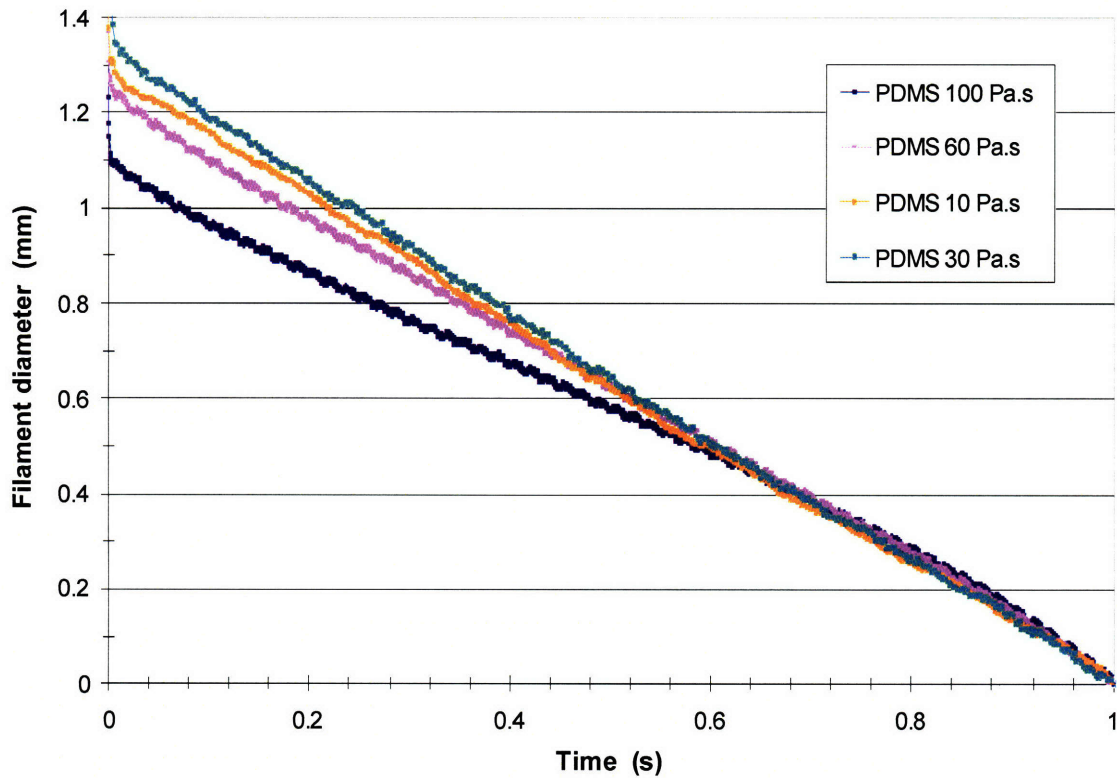


Figure 3.14. Comparison of CABER data showing that above a threshold of approximately 100,000 g/mol molecular weight PDMS (30 Pa.s viscosity), as the polymer increases in molecular weight it also increases in viscosity and elasticity. The increase in elasticity is illustrated by the increasing deviation from a linear profile for the filament diameter.

3.4.3 STP Oil Treatment

A similar analysis can be performed for STP in order to determine the mode of capillary breakup. STP is a weakly elastic fluid that was shown in Figure 3.1 to exhibit shear thinning and has a significant characteristic relaxation time, as illustrated in Figure 3.7. The filament profile of STP from CABER tests is shown in Figure 3.15 and can be qualitatively compared to the characteristic profiles from Table 3.3. The profile shows that while the filament is more cylindrical through the mid-section than PDMS melts, which are characterized as Newtonian at low molecular weights and as power-law fluids at high molecular weights, STP still maintains an hour-glass shape near the ends of the filament, so it likely well-characterized as a weakly elastic fluid.

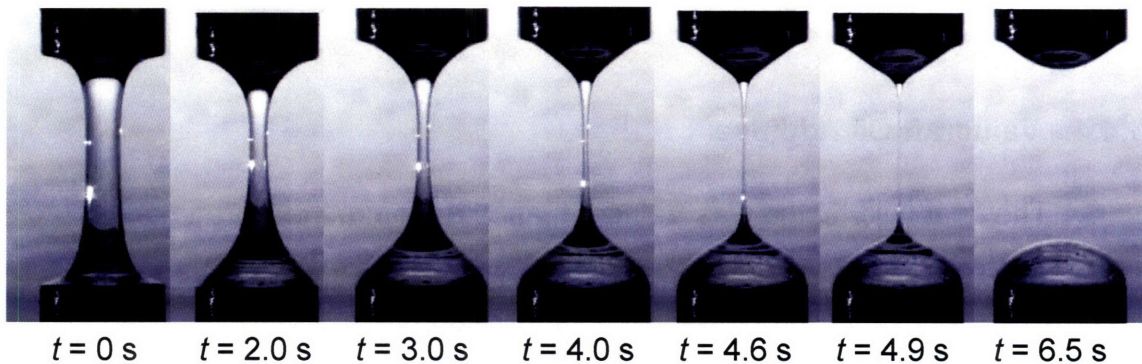


Figure 3.15. Filament thinning of STP Oil Treatment during capillary break-up testing. STP is a weakly viscoelastic fluid that can be modeled as a SOF.

To confirm this characterization, the filament radius profile measured with the digital micrometer is plotted in Figure 3.16 along with the prediction of the radius

from equation (3.18) considering the lubricant properties from Table 3.4 and with a fitted X correction factor value of 0.782 for end effects. The good correlation between the measured and predicted filament diameter measurements gives evidence that the SOF model can be used to describe the behavior of STP Oil Treatment.

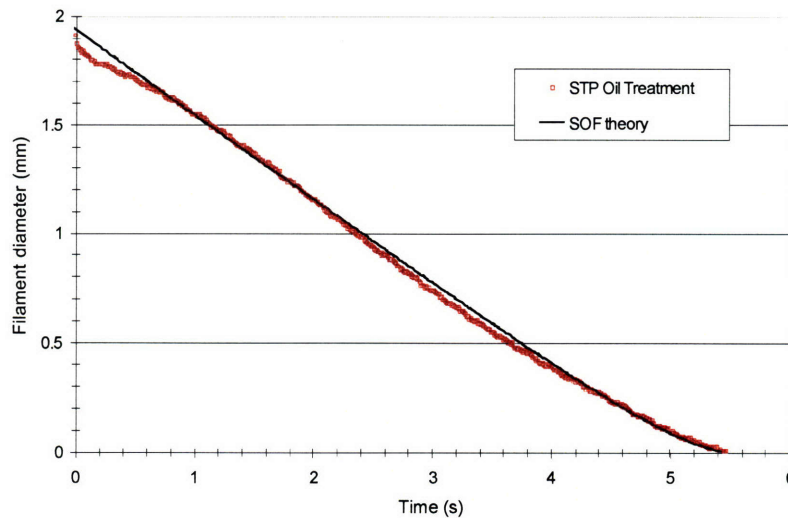


Figure 3.16. CABER data for STP. The slight decrease in slope for the filament midpoint diameter as a function of time indicates that STP can be modeled as a SOF. This model predicts a quadratic form for the changing slope

3.4.4 Valucraft Oil Additive

The final fluid tested was Valucraft, another commercial brand of oil additives. Although Figure 3.1 indicates that Valucraft shear thins at higher shear rates than does STP and Figure 3.7 shows that it has a lower characteristic relaxation time, it was expected to behave similarly to STP because both lubricants are used for the same application. Figure 3.17, however, shows a filament profile that is very different from the profile in Figure 3.15 for STP. The Valucraft filament forms an almost perfectly cylindrical thread

between the two fluid reservoirs instead of the more gradual transition from thread to reservoir for the STP fluid. This difference in filament profiles indicates that Valucraft should be modeled differently than STP.

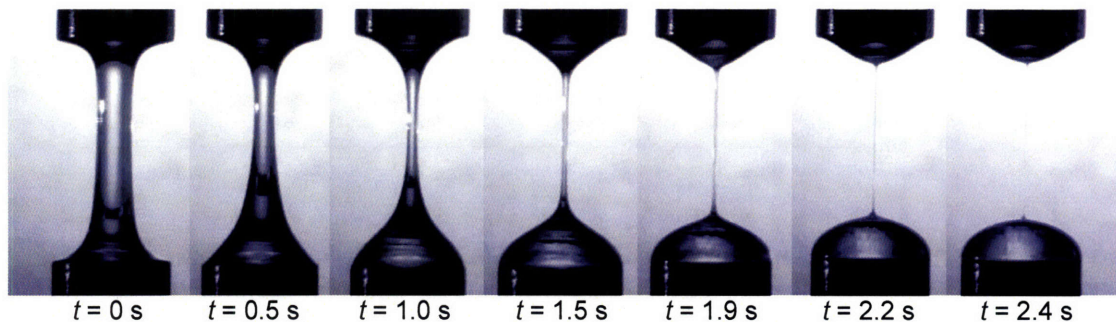


Figure 3.17. CABER filament profile for Valucraft oil treatment.

Comparison to Table 3.3 shows strong correlation between the filament profile for an elastic fluid and the Valucraft profile. To verify this correlation, the diameter versus time data for Valucraft is plotted on a semi-log graph, shown in Figure 3.18. This scaling shows that since the resulting data approximately fits into a straight line for times far from the initial strain and the final break-up, the resulting model must have an exponential relationship between time and filament diameter. This corresponds with the elastic model shown in Table 3.3.

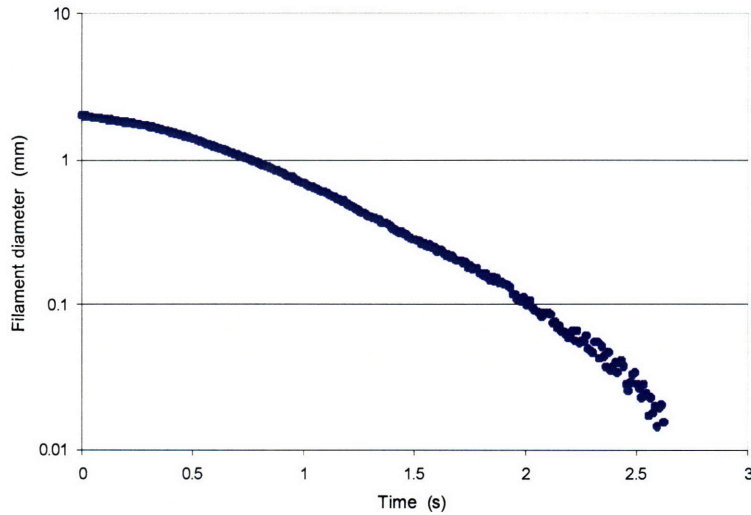


Figure 3.18. CABER data for Valucraft oil treatment. The indicated model for the filament radius will be exponential with time because the filament midpoint diameter during stable stretching is linear on a semi-log scale.

3.5 Discussion

Capillary break-up testing of fluid filaments for the lubricants in this study was used to determine the constitutive models that are appropriate to model the fluid stress/strain relationship. A summary of the lubricants and their associated constitutive models is given in Table 3.5. These models were verified by predicting the evolution of the diameter of a polymer bridge subjected to a step-strain, and the predictions were compared to experimental results from a capillary break-up rheometer. The resulting constitutive equations can be combined with lubrication equations to predict the stress/strain behavior of the lubricants subjected to sliding, lubricated contact and to modify the Stribeck diagram to consider elastic lubricants.

Table 3.5. Summary of rheometric properties of lubricants that are applicable to the tribological study of the Stribeck diagram.

Lubricant	Viscosity, η (Pa·s)	Relaxation time, λ (s)	Constitutive model
PDMS 10	10	NA	Newtonian
PDMS 30	30	NA	Newtonian
PDMS 100	100	0.012	Power-Law
STP	$\eta(\dot{\gamma}) = \frac{11.6}{(1 + (0.067\dot{\gamma})^2)^{0.17}}$	0.076	Weakly Elastic
VC	$\eta(\dot{\gamma}) = \frac{4.2}{(1 + (0.044\dot{\gamma})^2)^{0.135}}$	0.044	Elastic

CHAPTER 4: LUBRICANT ELASTICITY AND THE STRIBECK DIAGRAM

To understand how the lubricant rheology described in Chapter 3 affects the Stribeck diagram, a brief understanding of lubrication flow of Newtonian lubricants will be explained, and then these concepts will be applied to viscoelastic lubricant. Base oils such as mineral oil and silicone oil that have traditionally been used in tribological systems can be well characterized as Newtonian fluids. They have a constant viscosity that does not depend on the shear rate, and in the absence of inertial effects, they exhibit only a shear stress distribution that scales linearly with the imposed boundary deformation flow. When comparing the dynamical characteristics of the friction between two differentially rotating surfaces using Newtonian lubricants, the coefficient of friction C_f , is often presented as a function of the Gumbel number Gu , and the resulting curve is known as the Stribeck diagram. The Gumbel number can be found by non-dimensionalizing the Reynolds equation, which is given in equation (2.7) and re-written in cylindrical coordinates for the pressure gradient with angular velocity Ω :

$$\frac{\partial}{\partial r} \left(rh^3 \frac{\partial p}{\partial r} \right) + \frac{1}{r} \frac{\partial}{\partial \theta} \left(h^3 \frac{\partial p}{\partial \theta} \right) = 6\mu\Omega r \left(\frac{\partial h}{\partial \theta} \right) \quad (4.1)$$

Several quantities must be introduced to give the following dimensionless equation with the Gumbel number:

$$\bar{r} = \frac{r}{R}, \quad \bar{h} = \frac{h}{H}, \quad \bar{p} = \frac{p}{6\sigma R^2/H^2}, \quad Gu = \frac{\mu\Omega}{\sigma}$$

$$\frac{\partial}{\partial \bar{r}} \left(\bar{r} \bar{h}^3 \frac{\partial \bar{p}}{\partial \bar{r}} \right) + \frac{1}{\bar{r}} \frac{\partial}{\partial \theta} \left(\bar{h}^3 \frac{\partial \bar{p}}{\partial \theta} \right) = Gu \left(\bar{r} \frac{\partial \bar{h}}{\partial \theta} \right) \quad (4.2)$$

Figure 2.4 is repeated from Chapter 2 and illustrates that while the fluid properties of Newtonian fluids can be well-characterized by the Stribeck diagram, when the fluids are non-Newtonian and have elastic properties, they are not normalized on the Stribeck diagram with the Gumbel number. Chapter 3 presented the rheometric properties for viscoelastic lubricants, and showed that unlike Newtonian fluids, which are only characterized by the lubricant viscosity, viscoelastic lubricants have both viscous and elastic material responses. These non-Newtonian properties are evident in any of three ways: the viscosity can be a function of shear rate, shearing the two surfaces relative to one another can result not only in a shear stress distribution but also in an anisotropic normal stress distribution in the fluid due to the fluid elasticity, and the lubricant stress response to an applied motion may be out of phase with the imposed motion [47].

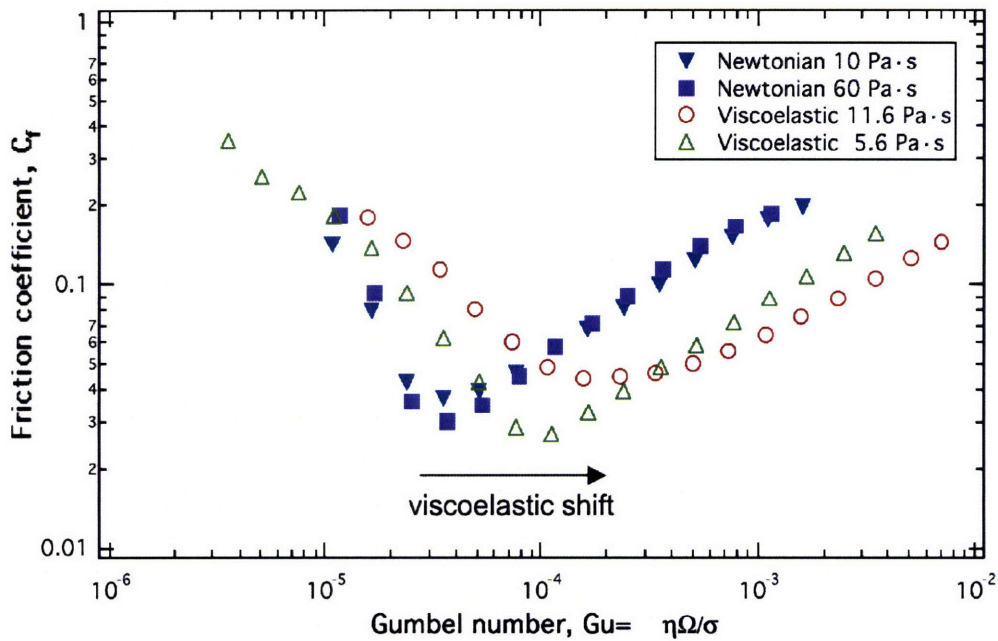


Figure 4.1. Stribeck diagram showing Newtonian and viscoelastic lubricants. While the fluid properties of Newtonian fluids can be well-characterized by the Stribeck, non-Newtonian fluids with elastic properties are not normalized on the Stribeck diagram with the Gumbel number.

Previous research on non-Newtonian boundary lubricants [62, 63] and experimental observation from friction testing (Figure 2.4)[18, 64] verify that friction testing with non-Newtonian lubricants can result in substantial deviations from the standard Stribeck curve measured under similar running conditions with Newtonian fluids. Since an extra material parameter, the fluid relaxation time, is needed to describe elastic lubricants, Buckingham Pi theory concludes that at least one additional dimensionless group must be added to the Gumbel number in order to fully describe the state of the system [65].

This section describes how to modify the Stribeck curve and Gumbel number in order to normalize the additional fluid properties of viscoelastic lubricants. The material responses discussed will include the shear rate-dependent viscosity and the added normal stress distribution. Phase-shifting of

the stress will not be discussed because the experiment described is steady-state shearing and not oscillating flow.

4.1 Shear Rate-Dependent Viscosity

The Stribeck curve normalizes lubricant properties using the lubricant viscosity, so when a lubricant with shear rate-Dependent viscosity is used, the appropriate viscosity must be determined. For this study, lubricants with characteristic relaxation times on the order of 10^{-2} were used, and therefore assuming a constant viscosity is only meaningful when the shear rates are less than the inverse of the relaxation time, or 10^2 s^{-1} . For the experiments performed for this study, shear rates from 1 to 10^5 s^{-1} were applied, and therefore the assumption of a constant, bulk viscosity is inappropriate.

Chapter 3 presented the Carreau model for lubricant viscosity in order to describe the viscosity as a function of shear rate. For lubrication flows, the layer of lubricant must be significantly smaller than the length-scale in the sliding direction. This indicates very small clearances between the sliding surfaces in the z-direction and therefore high shear rates $\dot{\gamma}$, using the definition for shear due to sliding velocity u :

$$\dot{\gamma} = \frac{\partial u}{\partial z} \quad (4.3)$$

The shear rate can be estimated from experimental data because the rheometer records a gap height at each data point. The gap height recorded is

the distance that the rheometer head has moved from an initial reference point and is therefore not the actual gap measurement between the two plates. In order to calibrate the gap height, a minimum gap must be determined, and this minimum gap occurs at the transition point from hydrodynamic lubrication to the mixed lubrication regime, which is the point of minimum friction on the Stribeck curve. Once the recorded gap is determined at the velocity corresponding to the minimum point of friction, the difference between the recorded gap and the actual gap can be calculated and defined as the calibration value because the actual gap will be approximately equal to the height of the tallest surface asperity since the minimum point of friction occurs just before the surfaces come into contact.

To calibrate the gap data, the calibration value, or the difference between the recorded and actual gap heights, can be subtracted from all of the data points to find the actual gap height. The accuracy for gap height is very tolerant because even a 2-micron change in the measured gap height at the transition point only corresponds to an 11 percent change in the viscosity of STP, which results in a change of less than 0.4 in the Gumbel number. Since the Gumbel number typically spans 3 decades, as long as the gap height can be determined to within $\pm 2\mu\text{m}$ there should not be significant error in the resulting value of the viscosity. The compliance of the rheometer is approximately $1\mu\text{m}/\text{N}$, but the normal force is maintained within $0.1\mu\text{m}$ of a constant value; therefore it is not a significant source of error.

The gap height is meaningful in the hydrodynamic regime and can be used to determine lubricant viscosity, but once surface contact is reached, the

gap height is no longer meaningful. Due to the high shear stress on the textured surface and the use of paraffin to attach the surface to the Peltier plate, Poisson effects in the paraffin can result in significant apparent changes in the gap height. These Poisson effects can be estimated, but this calculation is not important within the scope of this research. After reaching the mixed lubrication regime, it can be assumed that the surfaces remain in contact and therefore the gap height will only change as a result of surface wear or asperity breakage.

Figure 4.2 shows the gap measurements as a function of the Gumbel number in the hydrodynamic regime for a friction test on a flat nickel surface with STP as the interfacial lubricant. The surface roughness is approximately $1\mu\text{m}$, so the gap height has been calibrated according to this reference. Once the gap height has been determined at each rotational velocity Ω , the shear rate at the rim (rim radius is R) can be estimated as $\dot{\gamma} = \Omega R / \text{gap}$, and the corresponding lubricant viscosity at each point can be calculated from the Carreau model in equation (3.4). This shear rate-dependent viscosity can be used in place of the bulk lubricant viscosity in the Gumbel number in order to normalize the effects of variable shear for non-Newtonian lubricants.

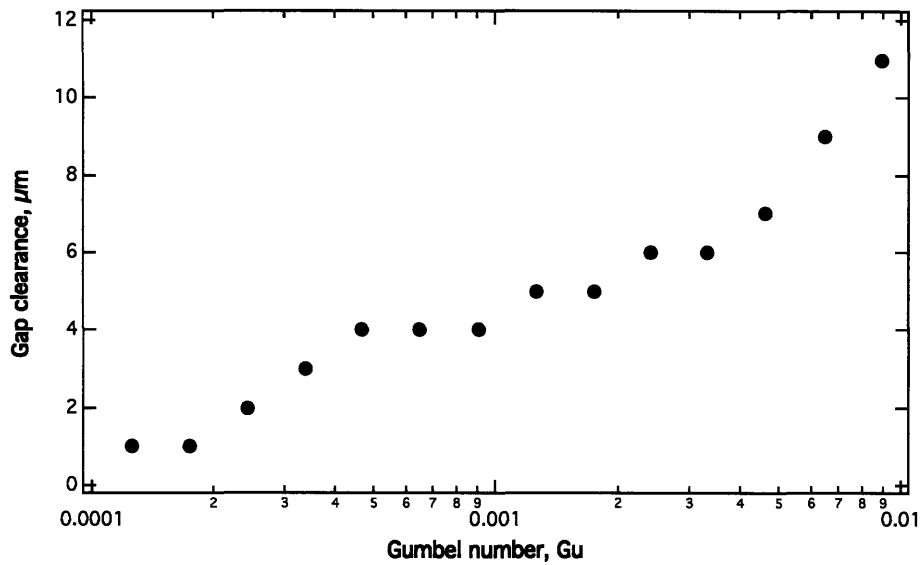


Figure 4.2. Gap clearance in the hydrodynamic regime increases with the Gumbel number. This clearance is calibrated with reference to the tallest asperity on the contacting surfaces.

4.2 Normal Stress Distribution

A general understanding of the normal stress distribution on a two-dimensional surface will require detailed simulations of both full-film and boundary lubrication with an appropriate viscoelastic constitutive equation or molecular model. Such detailed simulations in model geometries with smooth walls can now be considered [4, 66]. However, many lubricant oils are, by design, only weakly elastic and in this limit insight can be gained theoretically. For example, in 1974 Green and Brockley assumed a standard linear solid model of linear viscoelasticity to explore the effects of viscoelastic boundary lubricants on the transverse load rate dependence of static friction [62]. Using this assumption, they were able to successfully capture general curve shifts associated with the viscoelastic boundary lubricants on the transverse load rate

dependence of static friction instead of determining the shifts for only very specific simulated geometries and details.

Since linear viscoelastic constitutive models are inherently limited to studies of small deformations, they do not give rise to additional normal stresses in the fluid [47]. However, it is these additional normal stresses that we expect to modify the load bearing characteristics of a viscoelastic lubricant. To describe the effect of lubricant elasticity near the transition point on the Stribeck diagram, we thus need to consider a constitutive model that is capable of capturing the effects arising in the large straining deformations experienced by fluid elements in the narrow clearances between surfaces.

This study analyzes the Second-Order Fluid (SOF), which may be considered as the lowest order canonical model for steady flows of general non-Newtonian fluids [47] and has been used in previous studies of the general non-Newtonian effects on lubrication flows by Sawyer and Tichy [63]. This model was chosen because of the ability to measure the relevant material parameters. Reviews of other models, such as the Phan-Thein-Tanner fluid [19] and the convected Maxwell model [20] can also be found in the literature. The SOF constitutive model is a perturbation about the Newtonian fluid and is valid for slow and slowly varying flows. This model is used to systematically account for small departures from Newtonian behavior, and it is important to note that the SOF is a valid approximation to the fluid response only for small Deborah numbers where the second-order term is a small correction to the Newtonian solution. The Deborah number, $De = \lambda u / \ell$, is a ratio of the fluid relaxation time λ

to the characteristic convective time of the system, l/u . For the rotating system used in this study, the Deborah number is defined using the angular velocity such that $De = \lambda\Omega$. The constitutive equation for a SOF may be expressed in the form

$$\boldsymbol{\tau} = - \left[\eta_0 \boldsymbol{\gamma}_{(1)} - \frac{1}{2} \Psi_{10} \boldsymbol{\gamma}_{(2)} + \Psi_{20} \{ \boldsymbol{\gamma}_{(1)} : \boldsymbol{\gamma}_{(1)} \} \right] \quad (4.4)$$

where Ψ_{10} and Ψ_{20} are respectively the first and second normal stress coefficients, and $\boldsymbol{\gamma}_{(1)}$ and $\boldsymbol{\gamma}_{(2)}$ are the first and second rate of strain tensors. The rate of strain tensors are defined as

$$\begin{aligned} \boldsymbol{\gamma}_{(1)} &\equiv \dot{\boldsymbol{\gamma}} \\ \boldsymbol{\gamma}_{(2)} &= \frac{D}{Dt} \boldsymbol{\gamma}_{(1)} - \nabla \mathbf{v}^T \cdot \boldsymbol{\gamma}_{(1)} - \boldsymbol{\gamma}_{(1)} \cdot \nabla \mathbf{v} \end{aligned} \quad (4.5)$$

The characteristic relaxation time of the fluid, which is a measure of the fluid elasticity, can be defined in terms of the normal stress coefficient and viscosity such that $\lambda = \Psi_{10}/2\eta_0$. Since the SOF model is limited to terms that are of second order in the rate of strain tensor it does not describe shear-thinning in the viscosity. This has been described separately in the previous section.

To find the effect of lubricant elasticity on the Gumbel number, the solution for the resulting stress tensor of a SOF in a rotating parallel plate can be found using the constitutive model given by equation (4.4), the equation of motion, (equation), and the kinematic equations in cylindrical coordinates. The only velocity vector for the rotating system is given as

$$V_\theta = \frac{\Omega r z}{H} \quad (4.6)$$

for angular velocity Ω in rad/s, radius r in meters, and lubricant thickness H in meters with z measure in meters perpendicular to the lower surface into the fluid.

The resulting velocity gradient tensor is

$$\nabla v = \begin{pmatrix} 0 & \Omega z/H & 0 \\ -\Omega z/H & 0 & 0 \\ 0 & \Omega r/H & 0 \end{pmatrix} \quad (4.7)$$

The strain rate $\dot{\gamma}$, is the rate of change of the velocity vector across the thickness of the lubricant

$$\dot{\gamma} = \frac{\partial v}{\partial z} = \frac{\Omega r}{H} \quad (4.8)$$

Using this definition of the strain rate, the first and second convected derivatives of the strain rate tensor can be calculated from equation (4.5) to be

$$\gamma_{(1)} = \nabla v + \nabla v^T = \dot{\gamma} \begin{pmatrix} 0 & 0 & 0 \\ 0 & 0 & 1 \\ 0 & 1 & 0 \end{pmatrix} \quad (4.9)$$

and

$$\gamma_{(2)} = -2\dot{\gamma}^2 \begin{pmatrix} 0 & 0 & 0 \\ 0 & 1 & 0 \\ 0 & 0 & 0 \end{pmatrix} \quad (4.10)$$

Now that the kinematics are defined, they can be substituted into equation (4.4), the constitutive equation for the SOF, so that the resulting stress tensor in matrix notation is

$$\boldsymbol{\tau} = - \left[\eta \dot{\gamma} \begin{pmatrix} 0 & 0 & 0 \\ 0 & 0 & 1 \\ 0 & 1 & 0 \end{pmatrix} + \Psi_{10} \dot{\gamma}^2 \begin{pmatrix} 0 & 0 & 0 \\ 0 & 1 & 0 \\ 0 & 0 & 0 \end{pmatrix} + \Psi_{20} \dot{\gamma}^2 \begin{pmatrix} 0 & 0 & 0 \\ 0 & 1 & 0 \\ 0 & 0 & 1 \end{pmatrix} \right] \quad (4.11)$$

The Navier-Stokes equations can be reduced to a simplified index form by removing all of the non-existing stresses for the rotating parallel-plate system and the inertial terms. The resulting equations are

$$\frac{\partial p}{\partial r} = \frac{\tau_{\theta\theta}}{r} \quad 0 = -\frac{\partial}{\partial z} \tau_{z\theta} \quad \frac{\partial p}{\partial z} = -\frac{\partial}{\partial z} \tau_{zz} \quad (4.12)$$

After this simplification, the hoop stress $\tau_{\theta\theta}$ from the constitutive equation can be substituted into the pressure gradient in the radial direction, and integrating from the center of the disk to the outer rim radius solves for the pressure. Next, replace the pressure with the total normal stress $\pi_{zz} = \tau_{zz} + p$, by adding the normal stress to both sides of the pressure equation to get the following expression for pressure as a function of the shear rate at the rim $\dot{\gamma}_R^2$:

$$\pi_{zz} = p(R) + \frac{1}{2} (\Psi_{10} + \Psi_{20}) \dot{\gamma}_R^2 \quad (4.13)$$

To non-dimensionalize this equation, we introduce the following variables

$$De = \frac{\Psi_{10}}{2\eta_0} \Omega, \quad \bar{h} = \frac{h}{H}, \quad \bar{\pi}_{zz} = \frac{(\pi_{zz} - p)}{\eta_0 \Omega R^2 / H^2} \quad (4.14)$$

Using these dimensionless forms along with equation (4.13), the normal stress is related to the strain rate such that

$$\bar{\pi}_{zz} = De \left(1 + \frac{\Psi_{20}}{\Psi_{10}} \right) \frac{1}{\bar{h}^2} \quad (4.15)$$

Dimensional analysis indicated that the resulting frictional profile of weakly viscoelastic fluids is expected to be modified from the Newtonian result by the addition of an extra parameter, the characteristic relaxation time. Equation (4.15) indicates that the relaxation time is added in dimensionless form to the Stribeck diagram by modifying the normal stress that enters into the denominator of the Gumbel number to include the Deborah number. In addition to the added normal stressed in the lubricant due to elasticity, the SOF analysis does not include shear thinning properties of the lubricant, so these effects can be superimposed with the normal stress effects in a combined modified Gumbel number

$$Gu' = \frac{\eta(\dot{\gamma})\Omega}{\sigma(1 + \alpha De)} \quad (4.16)$$

The added constant α is a parameter that must be determined experimentally for a particular lubricant/surface pair. Although the Gumbel number can be shown to scale with the Deborah number, the extent of the added normal forces will depend on system/geometric parameters that must be determined experimentally.

4.3 Experimental Verification of the Modified Gumbel Number

To test the effect of viscoelastic lubricants on the friction between sliding surfaces, nickel surfaces were lubricated with both Newtonian and non-Newtonian lubricants and friction tested against a stainless steel rotating flat plate according to the experimental procedures for the triborheometer outlined in Appendix A. For this chapter, a steel 20-mm diameter parallel plate was rotated relative to a flat nickel surface that was attached to the Peltier plate using paraffin wax. The relevant lubricant properties are described in Chapter 3.

Figure 4.3 is a Stribeck diagram showing the friction for a 20mm diameter steel plate on a flat nickel surface with two different lubricants: PDMS30 and STP. In addition to these lubricants having a factor of 3 difference in viscosity (Table 3.5), PDMS30 can be approximated as a Newtonian lubricant, while STP exhibits both shear thinning and has a significant characteristic relaxation time. These two lubricants are not successfully normalized using the Gumbel number.

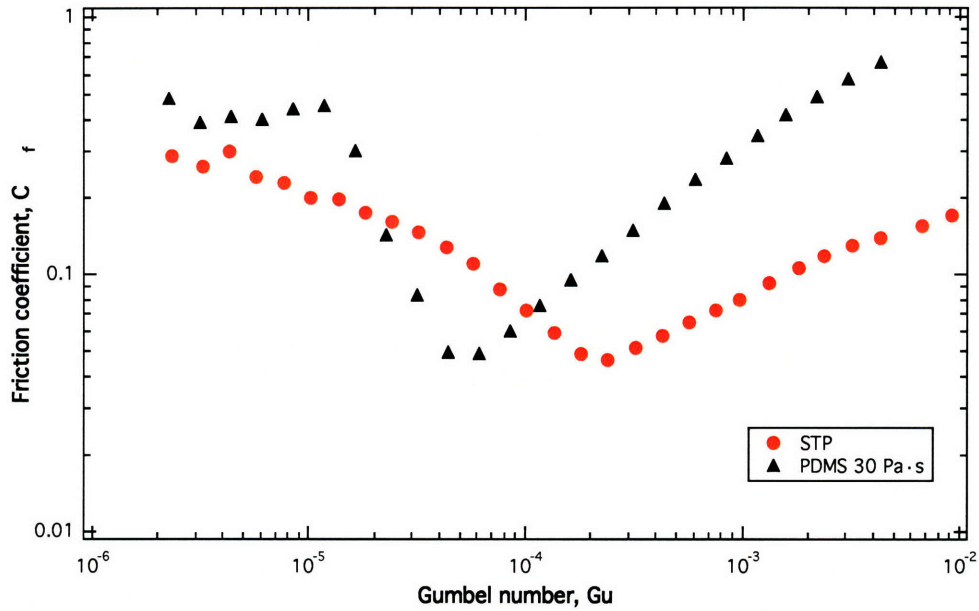


Figure 4.3. Stribeck diagram of STP and PDMS30 on a flat nickel surface. STP is characterized by both a shear-thinning viscosity and a characteristic relaxation time, while PDMS30 is a Newtonian lubricant.

The effects of shear thinning and the added normal forces can be seen individually by correcting for only one at a time on the Stribeck diagram. First, Figure 4.4 illustrates the same experiment from Figure 4.3, but instead of using the bulk viscosity in the Gumbel number, the shear rate-dependent viscosity is used. Since the viscosity of PDMS30 is not shear rate-dependent, its Stribeck curve does not change, but the curve for STP shifts to much lower Gumbel numbers since the actual viscosity at each particular rotational velocity is lower than the bulk viscosity.

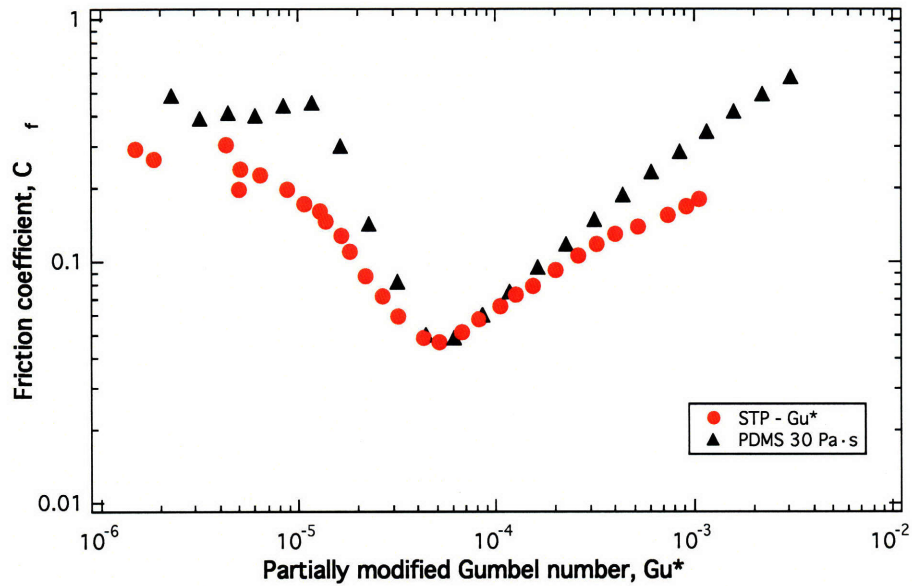


Figure 4.4. Stribeck diagram showing $Gu^* = \frac{\eta(\dot{\gamma})\Omega}{\sigma}$ for PDMS30 and STP. The viscosity for STP is corrected to be a function of shear rate.

Figure 4.4 shows that by only shifting the Stribeck curve to normalize the shear-thinned viscosity of the lubricant, the curve successfully shifts to agree with the Newtonian lubricant until reaching very high velocities. At high velocities, the curves diverge, indicating that there is another mechanism of lubrication that is not considered.

Now instead of correcting the Stribeck diagram for shear thinning effects, it is modified for normal stresses. Including the Deborah number in the calculation of the normal stress in the Gumbel number normalizes the Stribeck curve for added normal stress that arise due to lubricant elasticity. Figure 4.5 shows a Stribeck diagram with a dimensionless parameter that includes the bulk viscosity and the Deborah number.

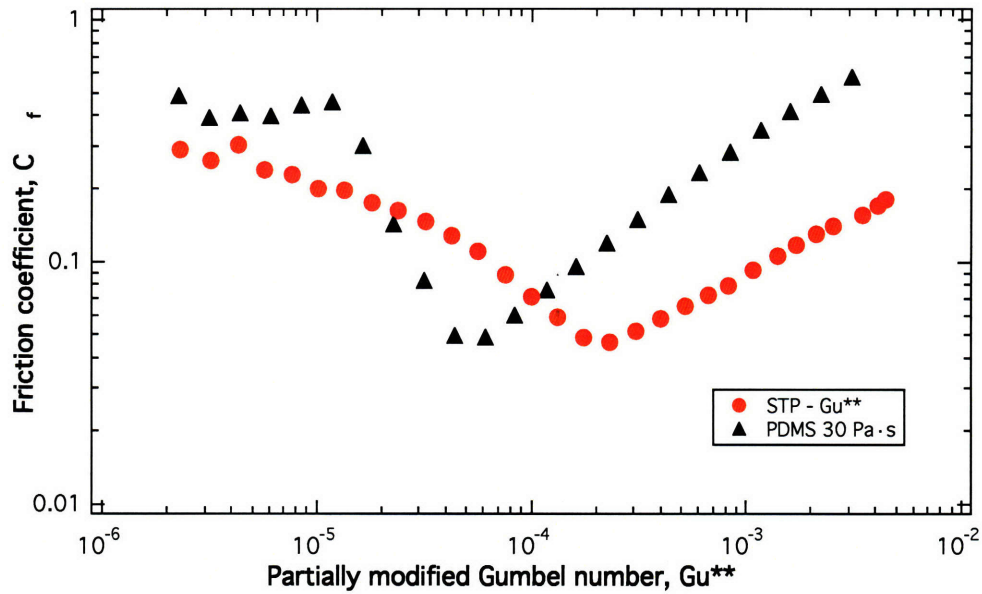


Figure 4.5. Stribeck diagram showing $Gu^{**} = \frac{\eta\Omega}{\sigma(1 + \alpha De)}$ for PDMS30 and STP. The normal stress are corrected by adding the Deborah number, which scales with $\alpha=0.6$.

The Deborah number corrects the Stribeck curve for the elastic tail at high velocities so that now in the hydrodynamic lubrication regime, the slopes for the Newtonian and viscoelastic lubricants are nearly parallel. This correction is only valid for the hydrodynamic regime since the theoretical basis was developed for a full-film of lubricant.

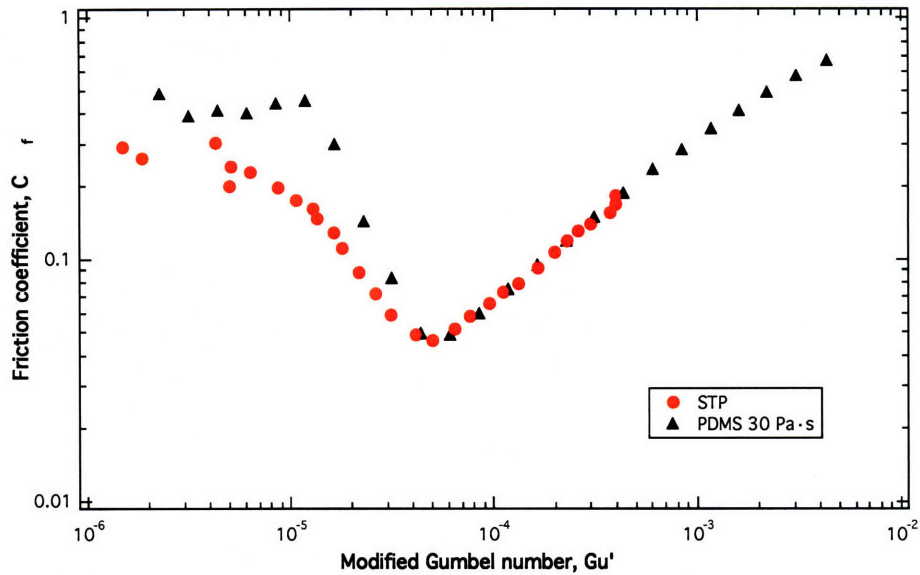


Figure 4.6. Fully modified Gumbel number with $Gu' = \frac{\eta(\dot{\gamma})\Omega}{\sigma(1 + \alpha De)}$. STP, a weakly elastic lubricant is shifted to normalize all elastic effects.

When both the shear thinning and Deborah number effects are included to form a modified Gumbel number, the resulting Stribeck diagram is shown in Figure 4.6. The experimental shift factor α is determined to have a value of 0.6 in order to match the experimental data. The influence of this shift factor on the Stribeck diagram is illustrated in Figure 4.7, which shows the Stribeck curves for different values of α .

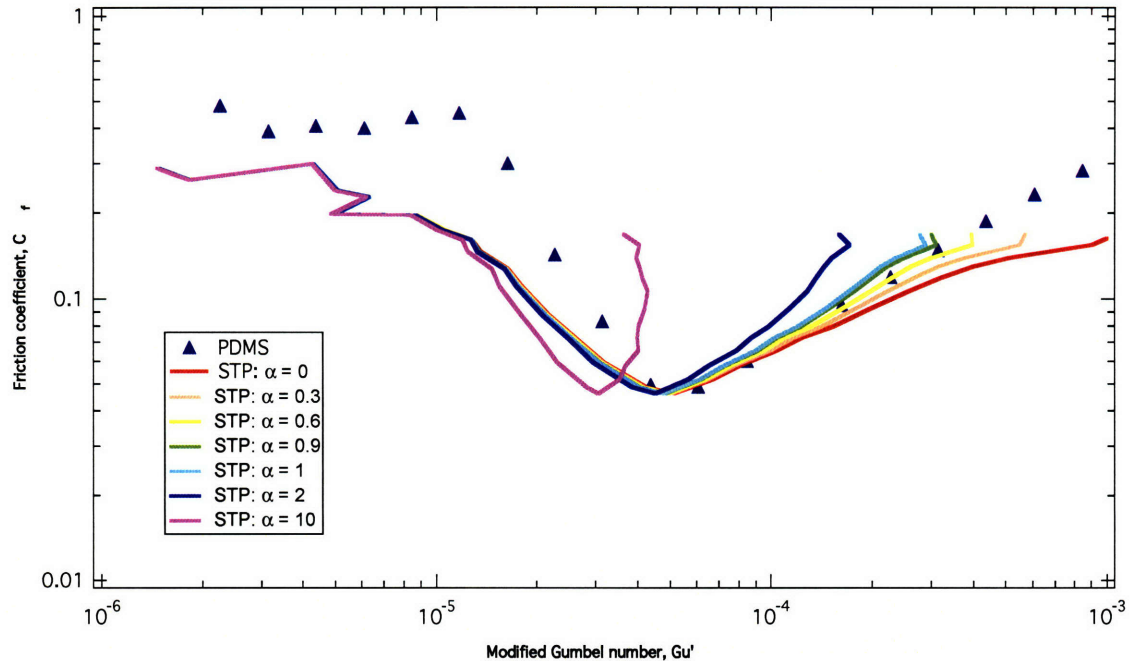


Figure 4.7. Limits of alpha. The influence of the parameter on the Stribeck diagram helps determine the appropriate value.

In order to assure that the proper lubrication mechanisms are being captured in the shear thinning and Deborah corrections, the properties and Stribeck curves of STP at different temperatures are measured. Table 3.2 gives the measured properties of STP at 5 different Peltier temperatures when the tests are performed on a glass plate attached to the Peltier plate. The viscosity and elasticity both change by nearly an order of magnitude, however, when the Stribeck curves are plotted using these new values with the modified Gumbel number, the curves remain normalized despite the change in fluid properties. This indicates that all of the contributing mechanisms are being captured in the modified Gumbel number and that it is able to successfully normalize both Newtonian and viscoelastic lubricants.

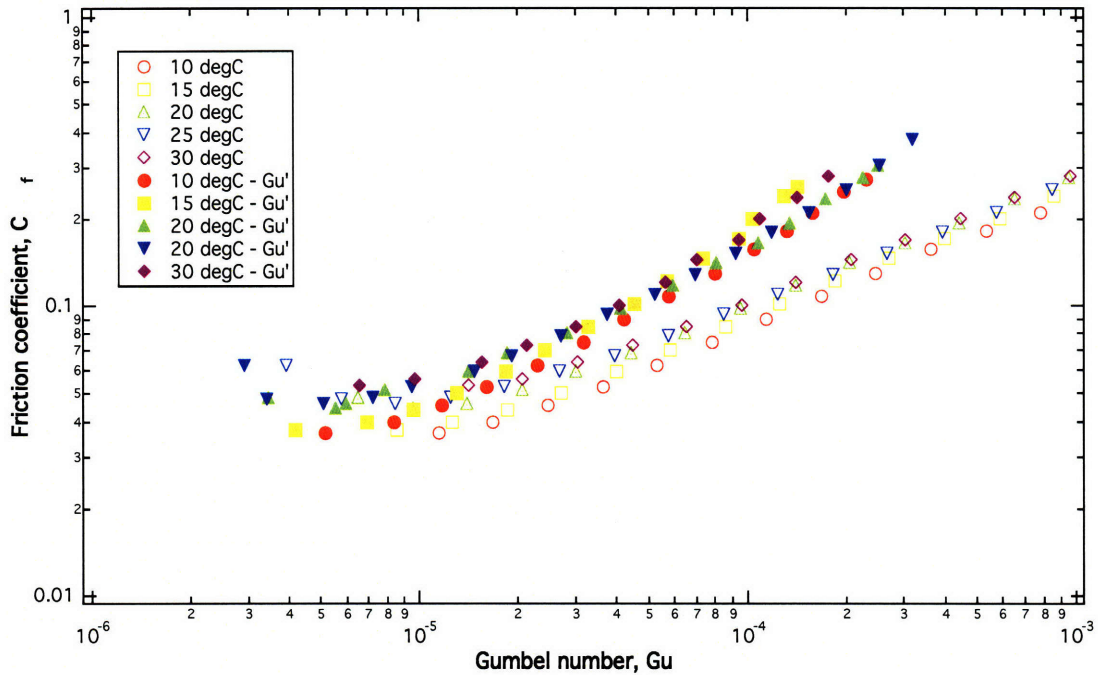


Figure 4.8. Stribeck curve showing Gu and Gu' at different temperatures with STP as the interfacial lubricant. The curves remain normalized despite the change in temperature, which indicates that the modified Gumbel number is able to successfully normalize viscoelastic effects. The friction tests were performed on a glass plate attached to the Peltier with a layer of wax. The reported temperature is at the Peltier plate and not the actual temperature of the lubricant.

To confirm that the modified Gumbel number successfully scales the Stribeck diagram for other viscoelastic lubricants, another lubricant was friction tested on a flat nickel surface along with 60 Pa·s PDMS. This new lubricant, Valucraft, is also a commercial oil additive but has different rheometric properties, as given in Table 3.5. Figure 4.9 shows that Valucraft is also successfully normalized with the modified Gumbel number to scale with Newtonian lubricants.

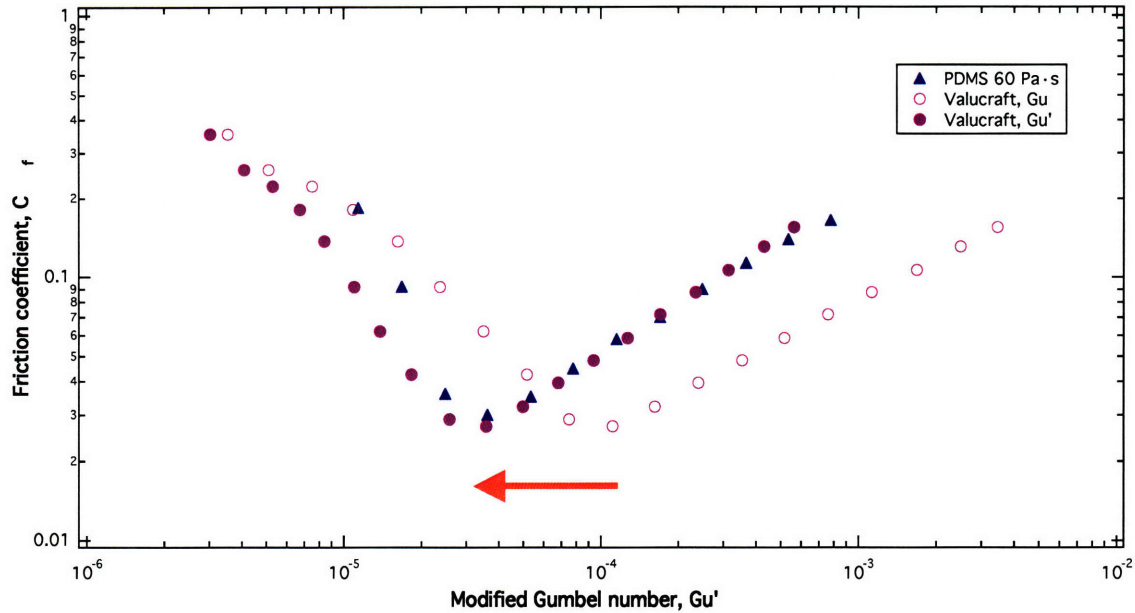


Figure 4.9. Valucraft and PDMS 60 Pa·s on flat nickel surface with modified Gumbel number. The red arrow indicates the shift when Valucraft is normalized with the modified Gumbel number compared to the original Gumbel number. $\alpha = 0.6$.

4.4 Summary

The Stribeck curve was shown in Figure 2.4 to successfully normalize the Stribeck curve for a lubricant/surface pair when the lubricant could be approximated as Newtonian over the range of applicable shear rates. Viscoelastic lubricants, however, were not successfully normalized. The curve shifting properties of viscoelastic lubricants can potentially be used to design systems with a lower friction coefficient at a particular set of running conditions, but a new dimensionless parameter is needed to normalize the viscoelastic effects on the Stribeck diagram.

The effects of both shear thinning and added normal stresses in a viscoelastic lubricant were demonstrated on the Stribeck diagram, and a novel dimensionless parameter that normalized these effects was introduced based on a Carreau viscosity model and the Second Order Fluid constitutive equations. Figure 4.6 shows that the new modified Gumbel number successfully modifies the Stribeck diagram for viscoelastic lubricants.

CHAPTER 5: SURFACE MICRO TEXTURING

Another method that has been shown to alter the frictional profile for a surface/lubricant pair is to add a micro-scale texturing to one or both sliding surfaces [41]. Shapes and designs for surface micro texturing depend on the application and lubrication regime for which the texturing is meant to reduce friction. Some of these textures are shown in Figure 5.1. For disk drives, the surfaces are typically lubricated with a boundary lubricant and contain raised bumps to prevent head stiction [67]. In fully flooded, high Reynolds number flows, texturing such as that found on natural sharkskin can be used to create a turbulent boundary layer near the sliding surface and therefore reduce skin friction. For slider bearings, a single channel close to the inlet of the slider has been shown to maximize lubrication [37, 68].

For this study, parallel surfaces are rotated relative to one another around a common axis with an interfacial lubricant, as shown in figure \$\$\$, and the required torque for rotation at a specified angular velocity is studied. These surfaces have cylindrical pores linearly spaced in rows and columns with a specified cavity depth. Because of the axial rotation of the surfaces, there is no symmetry in the hole placement.

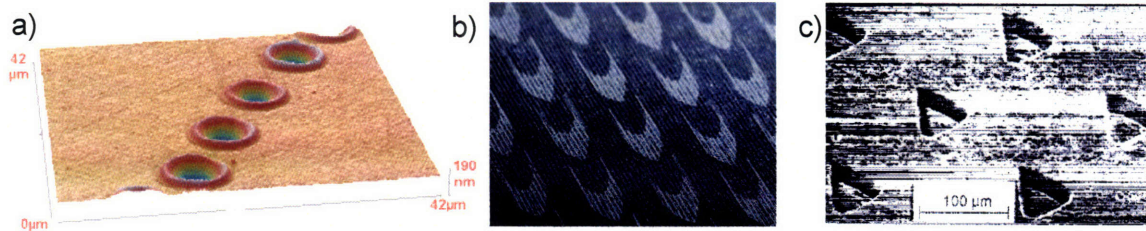


Figure 5.1. Micro textured surface. The shapes and designs for surface texturing depend on the target application. Photo a) shows a micro textured disk drive to help prevent head stiction [69], b) illustrates a 2mm-sized pattern sewn into Speedo's Fastskin™ swimsuits to reduce a swimmer's drag (www.speedo.com), and c) illustrates a suggested face-seal texture for lubricated, sliding friction [33].

5.1 Calculating Load Support

As a first approximation, when looking at a single cavity on a micro textured surface, it looks like a 2-part step bearing. First there is a step down, and then there is a step up. For surfaces with repeating patterns, these steps are typically equal in size and length so that the net effect of the steps is zero and there is no added load support. In 1966, Hamilton described the situation where a load-bearing asymmetric pressure profile can be produced from surface cavities. If cavitation is induced by the sudden drop in pressure over the leading edge of the surface cavity then the pressure profile that was previously symmetric is truncated at low pressures [26]. An illustration of a step bearing with a pocket of vapor from cavitation is shown Figure 5.2. For a semi-infinite, non-repeating patterned surface, the pressure profile can also be asymmetric due to differences in the pressure drop over the entrance and exit regions [38].

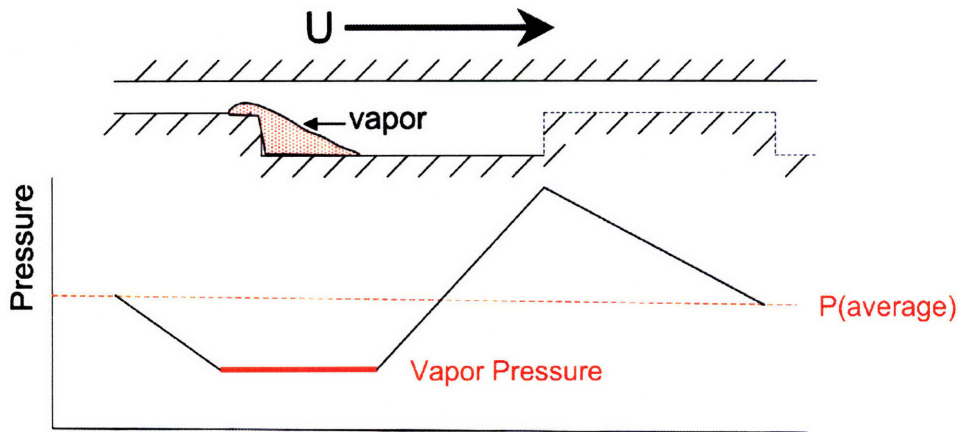


Figure 5.2. Illustration of cavitation in a surface hole resulting in an asymmetric pressure profile and thus positive load support.

To approximate the pressure distribution equations for a single surface cavity, the continuity equation is applied to each step region and the effects of the inlet and exit regions are neglected. Spikes discusses the possible consequences of including these regions in the analysis [38], but they will not be reviewed here.

The one-dimensional (infinitely long) geometry for the surface cavity analyzed in this study is given in Figure 5.3. The surfaces are nominally parallel, and the cavity has breadth L_c , while the surface region has breadth L_0 . The lubricant thickness is h_0 in the surface region and h_c in the cavity region, which gives a cavity depth of $H = h_c - h_0$. The pressure is assumed to be continuous between the two regions and is designated by p_0 and p_1 .

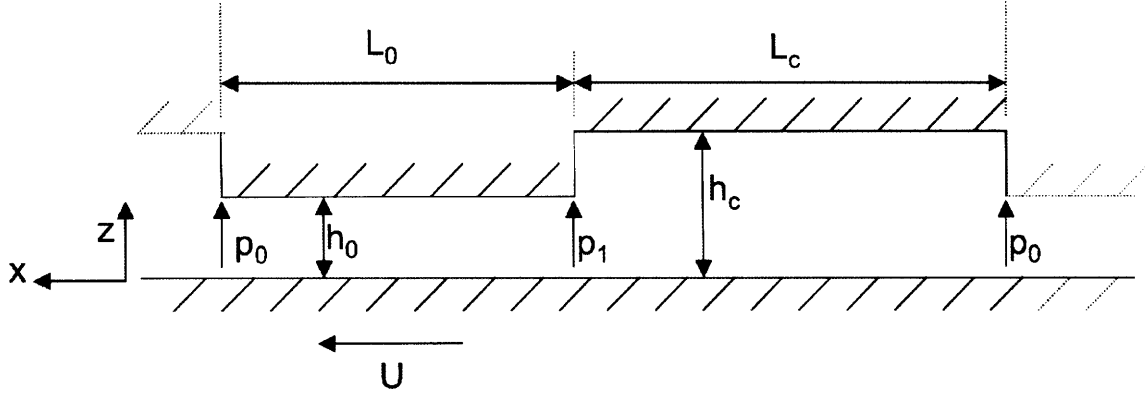


Figure 5.3. 1-D representation of a cavity on a micro textured surface. This pressure profile for this geometry can be described using the equations of continuity and momentum.

To start the pressure analysis, the one-dimensional equation of momentum in orthogonal Cartesian coordinates for Stokes' flow of an incompressible Newtonian lubricant of constant viscosity η , neglecting gravity and assuming constant velocity u is written as

$$0 = -\frac{\partial p}{\partial x} + \eta \frac{\partial^2 u}{\partial z^2} \quad (5.1)$$

The Stokes' flow assumption should be checked by ensuring that the Reynolds number, $Re = \rho U h_0 / \eta$, is much less than one. If the Reynolds number is close to one, then the inertial terms of the Navier-Stokes equations cannot be neglected. Equation (5.1) is solved for the velocity and applied to the surface region by assuming boundary conditions for the rigid bounding surfaces.

$$\begin{aligned} u &= U \text{ for } z = 0 \\ u &= 0 \text{ for } z = h_0 \end{aligned} \quad (5.2)$$

The pressure distribution between the parallel surfaces is linear if the edge effects are neglect, so the resulting equation for the flow rate per unit width of the bearing is

$$q_0 = \frac{Uh_0}{2} - \frac{h_0^3}{12\eta} \frac{(p_0 - p_1)}{L_0} \quad (5.3)$$

Physical insight about the problem can be gained by looking at the relationship between the pressure drop and the surface region breadth. For all other variables remaining constant, as the surface region gets larger, the pressure drop also grows.

Using the same momentum analysis with different boundary conditions, the flow rate in the cavity q_c , can be found and equated to the flow rate in the entrance region by the principle of continuity for an incompressible fluid $q_0 = q_c$ to give the equation

$$\frac{Uh_0}{2} - \frac{h_0^3}{12\eta} \frac{(p_0 - p_1)}{L_0} = \frac{Uh_c}{2} - \frac{h_c^3}{12\eta} \frac{(p_1 - p_0)}{L_c} \quad (5.4)$$

For surfaces with repeating patterns, this same conclusion would be reached if the surface region were split into an entrance and an exit region of equal lengths with an intermediate unknown pressure, so the equations are condensed here to represent a surface region and a cavity region.

The resulting pressure distribution in the lubricant can be solved from equation (5.4) in terms of the fluid properties, surface geometry, and the applied velocity

$$p_1 - p_0 = \frac{6\eta L_0 L_c (h_c - h_0) U}{h_c^3 L_0 + h_0^3 L_c} \quad (5.5)$$

This local pressure difference is required to determine at what speed cavitation occurs, but in order to determine the effect of micro texturing on load support, the pressure must be integrated over the surface. To capture the effect of texturing over the entire surface, the integration must be performed in multiple parts since the equations are not continuous over the entire surface. For the geometry shown in Figure 5.3, the integration for an infinitely long slider can be performed to determine the load support W per unit length B and is given by

$$\frac{W}{B} = \int_{L_c} (p_1(x) - p_0(x)) dx + \int_{L_0} (p_0(x) - p_1(x)) dx \quad (5.6)$$

Calculating the load using equation (5.6) requires an equation for each of the two pressures as a function of sliding distance. Since equation (5.5) shows only the pressure difference and not the pressure distribution, an alternate method must be used. First, it is assumed that the pressure distribution is linear with sliding distance in each of the two surface segments. Then, the load can be calculated as the area under the pressure curve as shown in Figure 5.5. This estimation leads to the following equation for the added load support due to the surface texturing $W_{texture}$:

$$\frac{W_{texture}}{B} = \frac{1}{2} L_0 (p_0 - p_1) + \frac{1}{2} L_c (p_1 - p_0) \quad (5.7)$$

5.1.1 Side Flow

The step-bearing pressure analysis presented considers only one-dimensional flow where all of the lubricant within the cavity must flow into and out of the surface cavity. An actual micro textured surface is characterized by three-dimensional flow, and Fuller discusses “side flow”, which occurs in an infinite-width step bearing as a result of the fluid flowing away from the high pressure region created by the step [70]. This flow along the channel of the bearing instead of over the step can reduce load capacity by almost 20%, according to Fuller. For the micro textured surfaces described in this study, the cavities have a finite length and width, as illustrated in Figure 5.4, so fluid cannot easily move out of the cavity without being forced over a step. Therefore, the effects of side flow will be significantly lower than the 20% predicted by Fuller, and consequently they will be neglected in this analysis.

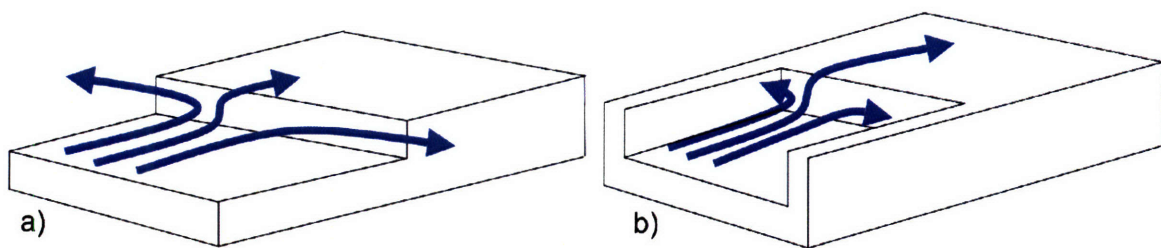


Figure 5.4. Side flow. This illustration shows: a) side flow in a step bearing for an infinite step, and b) the blocking of side flow when the geometry is a finite-width cavity.

5.1.2 Cavitation

As the relative velocity U increases, the pressure difference between the two surfaces will also increase and the pressure at the inlet to the surface cavity can drop below the pressure at which dissolved gases come out of the lubricant as vapor. This out-gassing of the dissolved gas from the lubricant can be above the vapor pressure of the lubricant itself, but in the tribology literature this event is referred to as cavitation [26, 71]. For consistency, the familiar terminology will also be used in this study, so the pressure at which dissolved gasses come out of the lubricant is called the cavitation pressure p_{cav} .

Since the pressure in the lubricant cannot fall below vapor pressure, the result of cavitation is an asymmetric pressure profile and a net positive pressure that gives positive load support. Figure 5.5 shows both the pressure profiles for the situations where the lubricant remains above cavitation pressure (a), and when it falls below cavitation pressure (b) for the geometry show in Figure 5.3.

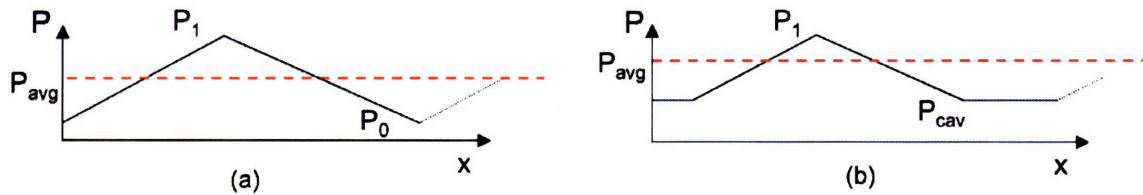


Figure 5.5. Representation of pressure profile for a surface with a cavity. The pressure does not fall below vapor pressure, so when the cavity has cavitated, the average pressure for the surface increases

$$P_{avg} = \frac{\int PdA}{\int dA} \quad (5.8)$$

Although there is an additional load support due to the asymmetric pressure profile, as a larger portion of the textured surface cavitates, there is less area to rebuild pressure within the surface cavity before reaching the edge of the step. In the case where the entire cavity has cavitated, it is not possible to build pressure within the cavity.

For a textured surface where a percentage ϕ of the surface cavity has cavitated, the equation for load support W , per unit length B , can be determined by splitting the cavity analysis into a separate cavitation region where the pressure remains at cavitation pressure. The resulting load support can be calculated, and the equation is given as

$$\frac{W}{B} = (L_0 + \phi L_c) \left(\frac{3\eta L_0 \phi L_c (h_c - h_0)}{h_c^3 L_0 + h_0^3 \phi L_c} \right) U + P_{cav} (L_0 + L_c) \quad (5.9)$$

5.2 Support for Cavitation Theory

Although a number of authors have described cavitation as a method of load support for textured surfaces, it is still not a widely accepted theory for load support. Only Hamilton [26] has shown experimentally that cavitation streamers exist on a textured surface by taking photographs of a textured face seal running against a glass surface. More evidence of cavitation using updated technology is needed to support the equations developed in this section. This evidence will be presented in Chapter 6.

CHAPTER 6: LOAD SUPPORT BY CAVITATION

Load support can be generated on a parallel textured surface if an asymmetrical pressure profile is generated such that there is a net load-supporting force. This is accomplished when the local fluid pressure drops below the cavitation pressure of the lubricant, which is the pressure at which dissolved gases come out of solution, and creates an isobaric pocket. Hamilton and coworkers introduced this concept of cavitation as the mechanism of load support in 1966 after observing cavitation streamers on the surface of a face-seal [26].

The work for this thesis describes experiments to verify that cavitation exists on micro textured surfaces and whether it occurs at velocities low enough to affect all lubricant load-bearing regimes of the Stribeck diagram. First, experimental work will be described that visually affirms the existence of cavitation on textured surfaces. Then numerical modeling will also be presented to support the assumption that the cavitation pockets can be theoretically predicted at high velocities where they are experimentally seen. This modeling will also be used to evaluate conditions at low velocities where localized cavitation is expected to exist but cannot be experimentally observed.

6.1 Experimental Evidence of Cavitation

The typical experimental setup for triborheometry, as described in Appendix A, was insufficient for visualizing cavitation because there was no way to see the contacting surface through either the rheometer head or Peltier plate. Instead of the typical arrangement, a new system was developed that maintained the functionality of the triborheometer but added the new dimension of surface visualization.

This new system rotated a textured, nickel surface relative to a glass plate. The textured surfaces were 20mm diameter aluminum disks that were processed according to the photolithography and electroless nickel texturing procedures in Appendix B. These disks were attached to a parallel plate rheometer geometry, but an alignment fixture was required in order to avoid eccentricity effects. As shown in Figure 6.1, this alignment fixture had a counterbored hole such that the through hole matched the diameter of the textured surface, and the counterbore matched the diameter of the rheometer geometry. Using this fixture, the textured surface was placed texture-down on the Peltier plate in the center of the alignment fixture, and a layer of paraffin is laid on top of the ring. Then the rheometer head is lowered into the alignment fixture, and a 15N normal force is applied to the surface of the textured disk while the temperature is raised to the melting point of the paraffin. After the melting point is reached and held for at least a minute, the Peltier is once again cooled with the normal force still applied so that parallelism is maintained. After cooling,

the alignment fixture is removed, and the textured surface should be securely affixed to the rheometer head.



Figure 6.1. Alignment fixture. This fixture centers the textured disk on the surface of the rheometer geometry to avoid eccentricity effects.

With the textured surface itself rotating, the mating surface was chosen to be a glass plate held in contact with a beam splitter that was 80% reflective at 532nm and affixed on top of the Peltier plate using melted wax. The beam splitter consists of 2 right-angle prisms attached at a 45-degree angle so that the mating surface is reflective and allows viewing of the contacting surface through the front of the cube, and the Peltier plate was still capable of measuring the applied normal force on the system. Figure 6.2 shows an illustration of the prism, and a photograph of the system is shown in Figure 6.3.

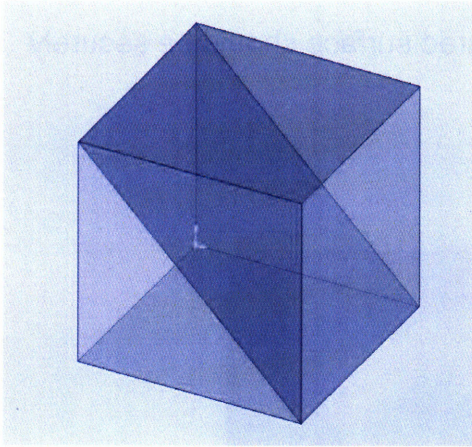


Figure 6.2. Illustration of the beamsplitter used as a mirror to view cavitation on the textured surface. The beamsplitter is made of two right-angle prisms, and the center plane acts as a mirror.

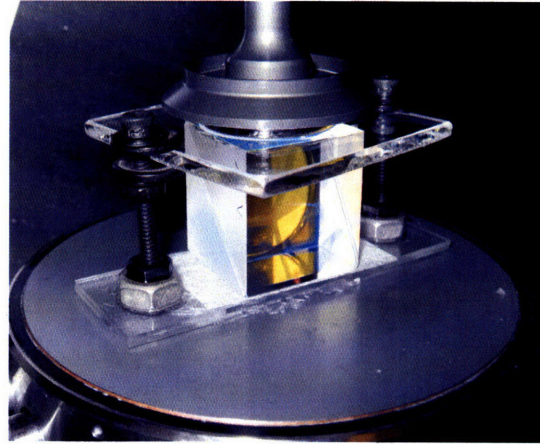


Figure 6.3. Photo of rheometer setup for cavitation visualization. The circular textured surface can be seen as yellow through the face of the prism.

A Phantom® 5.0 high speed camera was used with a Nikon ED lens to capture video of the cavitation through the side of the prism, and Phantom Camera Control v.8 software recorded the videos. The sample rate for the videos was 5300 pps, with a resolution of 512×512 pixels. The same experimental procedures as described in Chapter 3 were used for the cavitation testing with the exception that no run-in period was performed. Because the contact between surfaces remained in the hydrodynamic regime, there was no wearing down of the surface asperities. Video footage of the textured surface at different rotational velocities was recorded, and still images were collected from the videos.

6.1.1 Textured Surfaces

Figure 6.4 shows a series of images taken from a 100 μm 5% surface with STP as the interfacial lubricant. These images are snapshots of the surface at speeds increasing from 0.1 to 10 rad/s, and the circumferential cavitation streamers are visible as dark streaks on the surface. There are arrows pointing from the center of rotation to the innermost radius at which cavitation streamers are visible. Streamers are a result of a large quantity of vapor coming out of solution and building up in the cavity. Then it does not readily go back into solution due to saturation of the lubricant in the area around the cavity. Because cavitation can be a very localized phenomenon, the inception of cavitation occurs within the surface cavities at a much lower velocity than that at which streamers can be seen on the surface. Figure 6.4 shows cavitation streamers, but it is not possible to see from these images where localized cavitation is occurring.

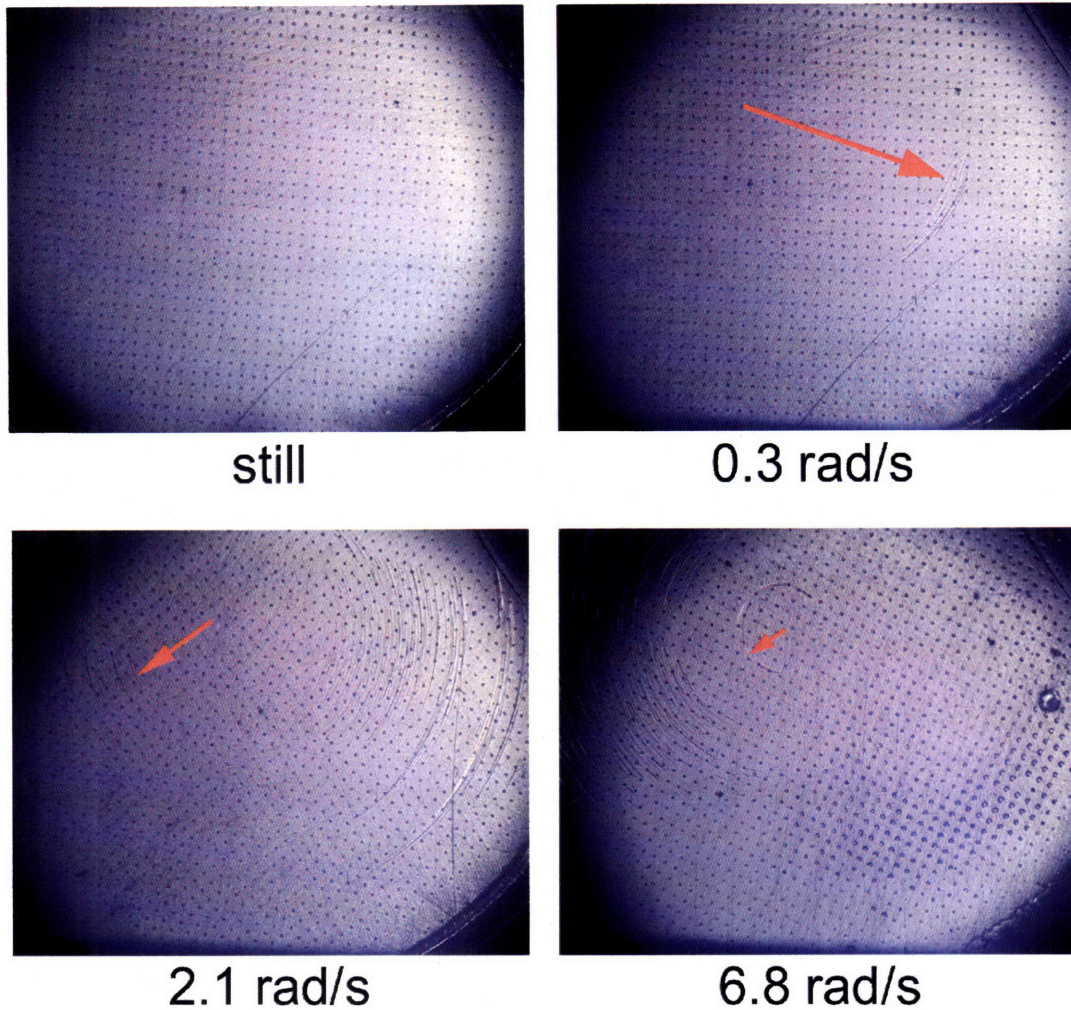


Figure 6.4. Pictures showing cavitation streamers taken from video footage of a textured surface with $100\mu\text{m}$ holes at a 5% area density. Each photo is $14 \times 17 \text{ mm}^2$. The textured surface was rotated relative to a glass surface with STP Oil Treatment as the interfacial lubricant. The radius of the cavitation streamers, which is indicated by a red arrow, decreases as a function of increasing velocity.

The innermost radius of cavitation changes in each image of Figure 6.4 because both the rotational speed and the gap between the two surfaces are changing. Table 6.1 shows the gap height and innermost radius of the occurrence of cavitation streamers for the $100\mu\text{m}$ 5% surface shown in Figure 6.4. For a specified gap, the sliding speed at which cavitation initiates can be calculated from equation (5.5). Table 6.1 shows the calculated experimental

rotational velocity and the theoretical velocity calculated using equation (5.5) with an estimated oil cavitation pressure of 85% of atmospheric pressure. This pressure is a commonly accepted value for motor oil, but experiments were performed for verification.

The cavitation pressure is considered to be the pressure at which dissolved gasses come out of solution, which should be evident by the appearance of bubbles in the liquid. A sample of STP was placed under vacuum, and the pressure at which bubbles were visible was recorded as 0.6 atm at 23°C. Because bubbles only become visible when enough gas has collected to grow to a visible size, the recorded 'cavitation pressure' is a very low limit of pressure. The actual pressure is expected to be much higher, and therefore the generally accepted value of 0.85 atm is reasonable.

Table 6.1. Experimental and theoretical cavitation velocity for 100µm 5% surface. The measured radius and rotational speed give the velocity for cavitation and can be compared to the calculated velocity for the given gap height and velocity.

Rotational speed (rad/s)	Cavitation radius (mm)	Measured gap (mm)	Observed velocity (mm/s)	Calculated velocity (mm/s)
0.3	5.5	0.003	1.7	0.9
2.1	2.0	0.007	4.3	1.5
6.8	1.4	0.017	9.4	4.3

As expected, the calculated linear speed at the cavitated holes is significantly lower than the velocity at which cavitation is seen with the triborheometer setup. The cavitation that can be seen on the textured surface in Figure 6.4 is only visible once enough of the hole has cavitated so that the gas does not readily go back into solution and therefore the cavitation streamer can be seen. Before reaching the observed velocity, there is local cavitation within the hole that cannot be seen using the Phantom camera system without significant magnification.

For completeness, a 100 μ m 10% surface with the same surface properties and more surface roughness was tested to look for evidence of cavitation. This surface had consistent results with the 100 μ m 5% textured surface except that the cavitation occurs at different velocities, due to different geometric dimensions as indicated in equation (5.5). Still images collected from video footage are shown in Figure 6.5, with the circumferential cavitation streamers appearing as dark streaks.

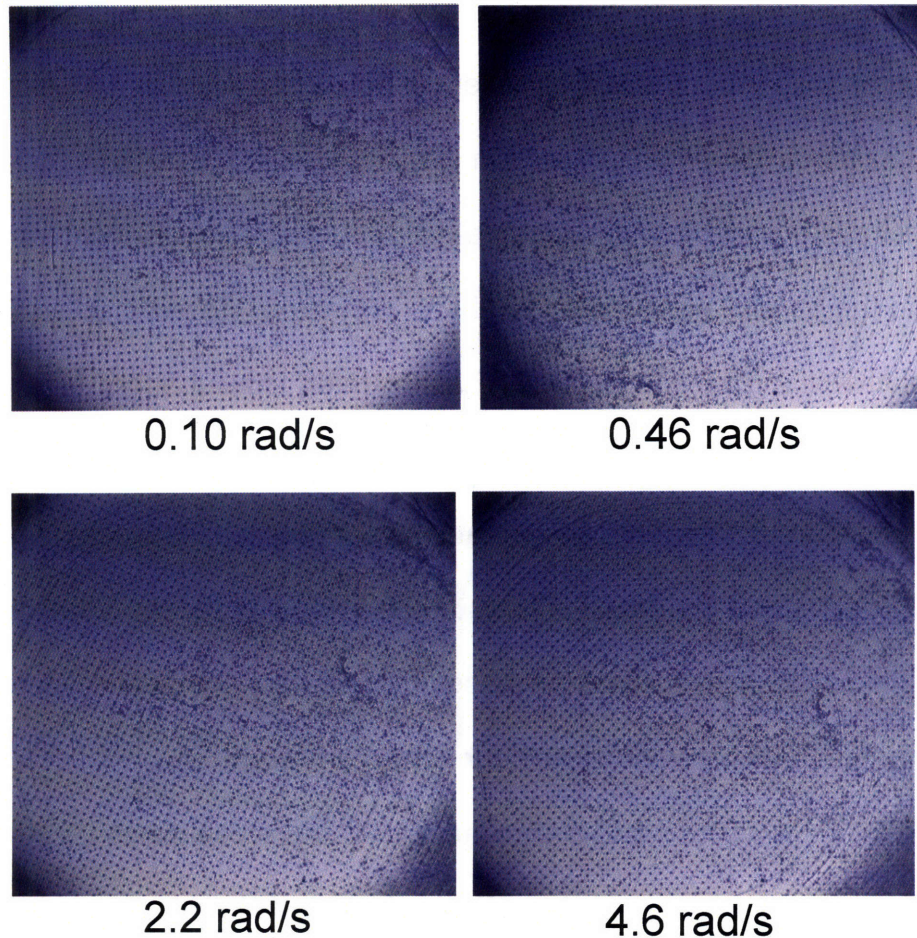


Figure 6.5. 100µm 10% surface with cavitation streamers. Each photo measures 15×17 mm², and STP is used as the interfacial lubricant. The cavitation streamers here are consistent with the streamers seen on the 100µm 5% surface.

6.1.2 Flat Surface

Cavitation occurs on surfaces as a result of lubricant flowing over designed cavities in the surface, and Figure 6.4 and Figure 6.5 show that applied surface texture can induce cavitation. In addition to applied surface textures, when looking at a textured surface under a higher magnification, small-scale surface roughness that is a result of manufacturing conditions can be seen. The hydrodynamic stability of parallel surfaces under lubricated contact is often

contributed to this roughness without specifically defining which mechanisms are supporting the load [46]. Evidence presented below suggests that at least one of these mechanisms is lubricant cavitation.

A flat nickel surface with a surface RMS roughness of $0.015\mu\text{m}$ was attached to the parallel plate rheometer head in place of the textured surface and rotated relative to a glass plate with STP as the interfacial lubricant. Figure 6.6 shows that cavitation streamers developed on the surface. This result is expected because experiments show that load support is possible on two parallel surfaces. The support is a result of the surface asperities acting in the same way as the applied surface texture, since these tiny step bearings also cavitate and help support the load between sliding, lubricated surfaces.

In addition to micro-scale surface texturing, there could also be other mechanisms of load support. The waviness of the surface was determined to be on average $0.1\mu\text{m}$, with a wavelength of 5 mm, as measured by a Dektak³ surface profilometer, so there could also be a plane slider effect where the slightly inclined surface is contributing to hydrodynamic lift. This additional load support must be considered when approximating the Stribeck diagram for textured surfaces. It is important to note, however, that cavitation streamers are seen at lower velocities on the textured surfaces than on the flat surface. This indicates that while the surface waviness and roughness may cause cavitation, the applied surface micro texture enhances the induced cavitation.

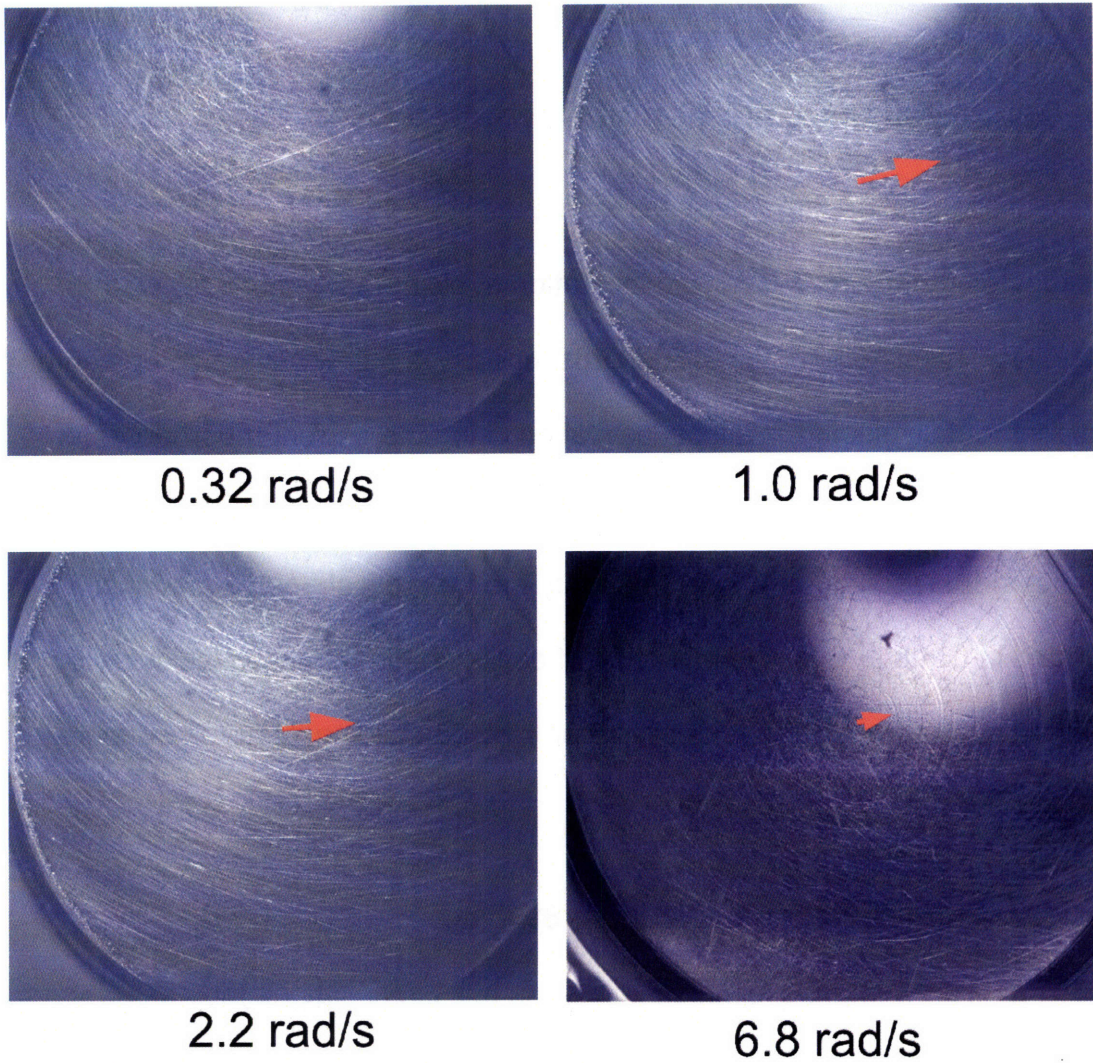


Figure 6.6. Cavitation streamers on flat surface. Each photo measures 23×28 mm². Surface roughness results in cavitation streamers on a flat surface lubricated with STP. The streamer with the innermost radius is indicated with a red arrow. This cavitation can improve load support for the surface.

6.2 Numerical Investigation of Cavitation

While cavitation streamers are visible at high rotational speeds, theory also indicates that there is localized cavitation at slower speeds. Cavitation initiates at points where the local fluid pressure drops below cavitation pressure, but experimentally seeing this local cavitation using the current triborheometer setup and visualization methods is not possible due to the lubricant layer and the current camera resolution. In order to verify the theoretical approximations developed in Chapter 6 for the inception of cavitation, numerical simulation can be used to determine the limits of cavitation between sliding, textured surfaces.

6.2.1 Numeric Simulation of Textured Surfaces

The direct numerical simulation used in this study was developed by Y. Li, F. McClure, and T. Tian at the Massachusetts Institute of Technology. Designed to simulate hydrodynamic lubrication [72], Li's model uses a Universal Reynolds equation that was developed by Elrod to accommodate two-phase lubrication flow [73]. The Universal Reynolds has a "cavitation index" that indicates whether the lubricant is in liquid form or the lubricant is at cavitation pressure and therefore in vapor phase. In liquid phase, then the pressure distribution is governed by the Reynolds equation, but in the vapor phase, the pressure remains constant at the cavitation pressure, and the mass of the vapor is neglected.

Applicability of the Reynolds equation in determining pressure distribution in micro textured surfaces is questioned in tribology research due to the cavity depth over gap ratios that exist in the surface cavities. A good review of the different arguments is given by Feldman et al. [74]. The typical argument describes the need for an inertial term in the calculations because the gap between the surfaces increases, and there is significant flow disturbance due to the sharp surface corners. For the present system, the Reynolds number defined using the gap between the surfaces as the length scale $Re = \frac{\rho UH}{\eta_0}$, ranges from 10^{-8} to 10^{-3} within the surface cavities. Because these low Reynolds numbers, which are a result of the relatively low speeds and high viscosity lubricants used in this study, inertial terms will be neglected.

The assumptions made in developing the Universal Reynolds equations are the same as those described in Chapter 2 for applying the lubrication approximation and using the Navier Stokes equations to find the pressure distribution in a flow. First, the lubricant is approximated as a Newtonian fluid with a constant viscosity. This assumption does not allow for lubricants that have a shear rate-dependent viscosity, nor does it consider the generation of normal stresses as a result of lubricant elasticity when the fluid is subjected to a shear flow. These effects in sliding, lubricated contacts are discussed in Chapter 4 with respect to the Stribeck diagram. For the lubrication approximation, the pressure is assumed to be constant across the gap between the sliding surfaces.

In addition to assumptions about the flow, the bounding surfaces are assumed to be rigid and smooth. More complete models, such as the average

Reynolds equation that was developed by Patir and Chang [50], could be designed to account for surface roughness. Surface deformation could be considered using an elastohydrodynamic model such as the one developed by de Kraker [75], but the scope of the modeling for this research did not require such detail. The focus was to determine scaling parameters, and therefore the changes in surface properties would be common to all surfaces regardless of the geometric texturing parameters.

To solve for the pressure distribution within the lubricant layer, a control volume method is used to discretize the governing equations [76]. The resulting equations composed a very sparse system, and Li used sparse solver iteratively find the pressure distribution in the lubricant [77]. Details about the particular numerical algorithm used in this simulation are described by Li [72].

In order to use Li's direct numeric simulation to determine whether cavitation occurs at low velocities with the geometries presented in this study, periodic boundary conditions were applied to the boundaries that were perpendicular to the sliding direction. Because the surface map that was developed for the model only represented a section of cavities with boundaries corresponding to the midpoint between the modeled cavities and the neighboring cavities, as is shown in Figure 6.7, periodic boundary conditions were appropriate to estimate the effects of neighboring cavities.

The inputs of the numerical simulation are the surface map, sliding velocity, clearance between the two surfaces, lubricant bulk viscosity, and the applied normal stress. The surface map is a text file that gives the surface height

measured from the top surface, so that the height is equal to the cavity depth when inside of a cavity and equal to the asperity height when on the surface level. These surface maps only modeled applied surface texture and did not consider surface roughness. For this study, the surface map was written using MATLAB so that the resulting text file was a single column of data. A surface plot of this data is shown in Figure 6.7. The sliding velocity was determined to be the rotational velocity times the average radius of the disk, and the clearance between the two surfaces was estimated from experimental data on a similar surface with the same viscosity and rotational speed. The lubricant viscosity was also estimated from experimental data to be the shear-thinned viscosity at the particular rotational velocity.

The outputs of the numerical simulation are maps of the location of cavitation on the surface and the pressure distribution on the surface. The cavitation maps are taken directly from the “cavitation index” parameter used in the Universal Reynolds equation [73] that determines when cavitation is present.

6.2.2 Comparing Results with Numeric Simulation

To verify that the numerical simulation corresponds with observed experimental data, the running conditions applied to the triborheometer can be entered into the simulation, and it is expected that the model produce results that indicate cavitation at the radii where cavitation streamers are observed. The lowest speed at which streamers were observed on the 100 μ m 5% textured surface was 0.3rad/s. The innermost radius of cavitation was 5.5mm, which

corresponds to a sliding speed of 1.65mm/s, and the measured gap height at that speed was 3 μ m. From the speed and gap height, the shear-thinned viscosity for STP can be calculated using a Carreau model to be 1.8Pa.s.

When these parameters are entered into the numerical simulation, along with the surface map (Figure 6.7), the resulting pressure profile is given in Figure 6.8. From this profile, it is clear that the pressure distribution is truncated at the cavitation pressure and therefore the resulting distribution is asymmetric. The cavitation map for this simulation is shown in Figure 6.10; any area shown in blue indicates that the lubricant is in a vapor-phase rather than in a liquid-phase. The cavitation map for the 100 μ m 5% textured surface at a rotational speed of 0.3rad/s shows that the hole has completely cavitated, and therefore it follows that cavitation streamers are likely to be seen from holes at this particular radius on the surface.

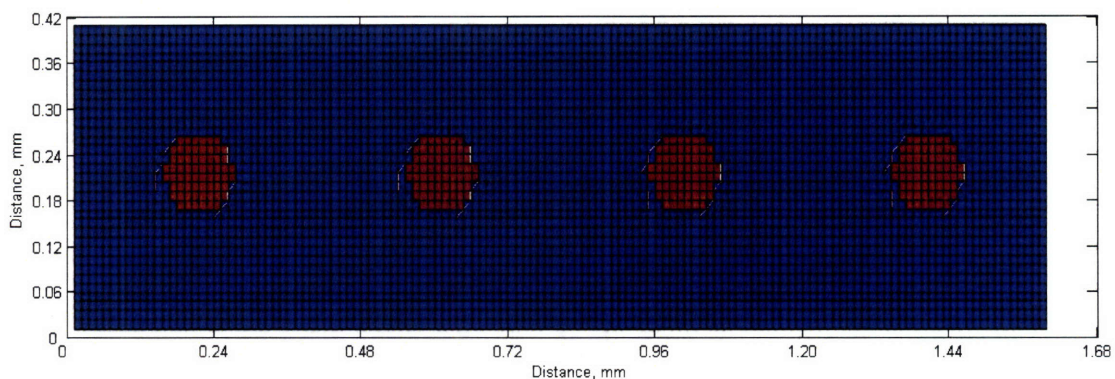


Figure 6.7. Surface map for 100 μ m 5% surface. This section of a 100 μ m 5% surface is the input to the numerical simulation to determine pressure on the textured surface.

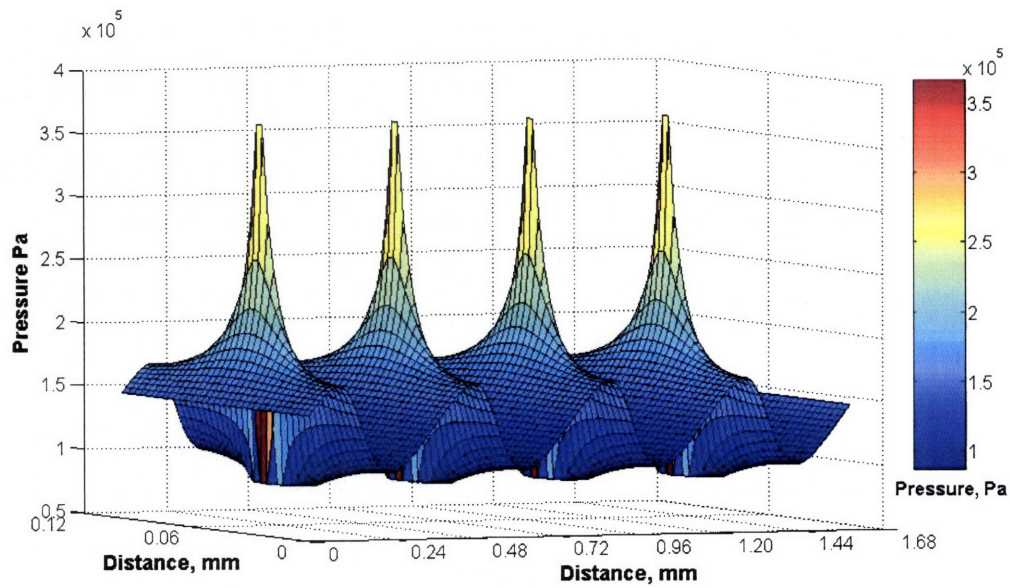


Figure 6.8. Pressure profile at 1.65 mm/s. The pressure profile for a 100 μ m 5% textured surface at a velocity of 1.65 mm/s shows an asymmetric pressure that is truncated at the cavitation pressure.

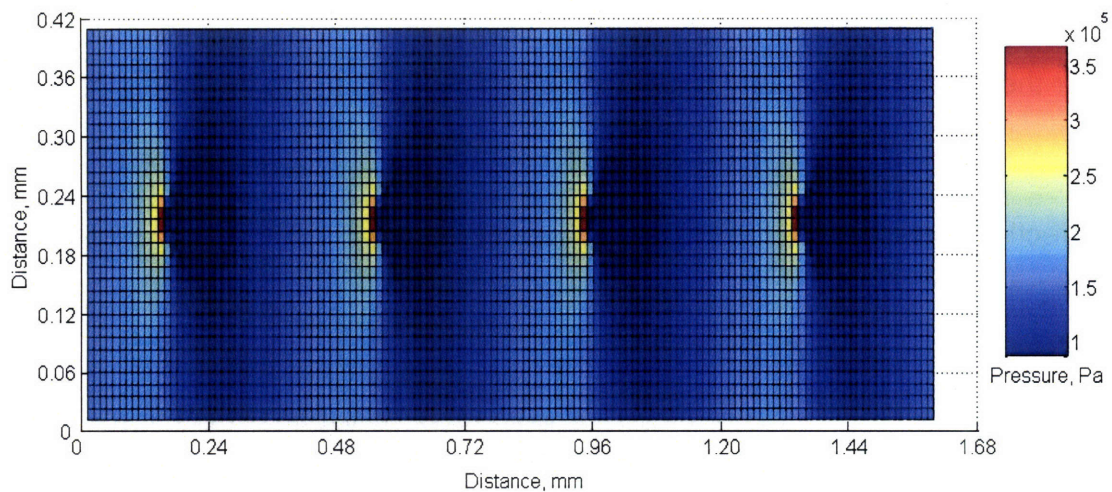


Figure 6.9. Pressure map at 1.65 mm/s. The pressure map for a 100 μ m 5% surface sliding at 1.65 mm/s illustrates that there is both a pressure gradient in the sliding direction and in the radial direction.

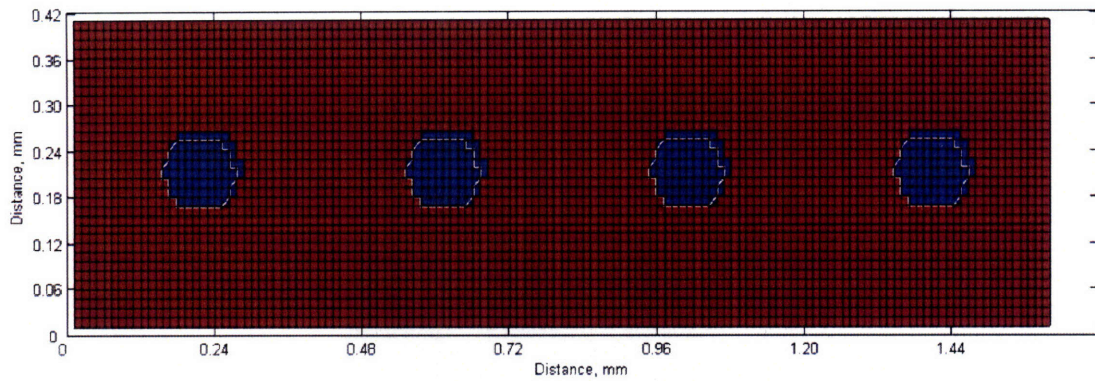


Figure 6.10. Cavitation map at 1.65mm/s. When compared to the surface map in Figure 6.7, the blue shading on this cavitation map indicates that the entire cavity for the 100 μ m 5% textured surface sliding at 1.65 mm/s with STP as the interfacial lubricant is filled with vapor.

As a comparison, holes that are 2-places closer to the center of rotation have a circumferential velocity of 1.4mm/s, and Figure 6.4 shows that there are no cavitation streamers from cavities at this velocity. Figure 6.11 and Figure 6.12 show data from a numerical simulation for this new speed. The gap is constant over the entire surface, and there is no significant change in the lubricant viscosity. The red section in Figure 6.11 shows that the cavitated region is not perfectly circular, which indicates that the entire cavity is not in the vapor-phase.

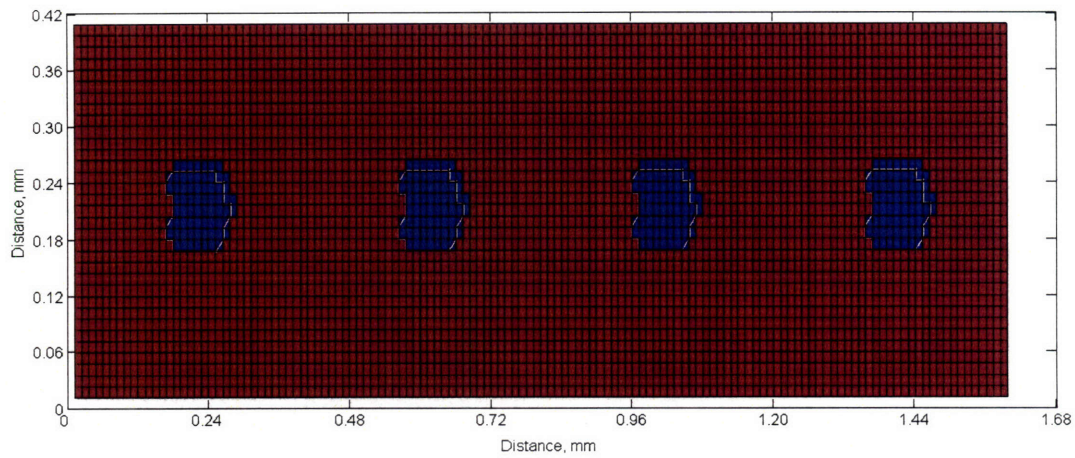


Figure 6.11. Cavitation map at 1.4mm/s. The non-symmetrical blue regions indicate that holes in the 100 μ m 5% textured surface are not entirely vapor-filled. 1.4mm/s corresponds to the velocity of a surface cavity that is 2-spaces or about 0.8mm closer to the center of rotation for the surface in Figure 6.4.

The pressure distribution for this slower speed is shown in Figure 6.12. There is still an asymmetric pressure distribution because cavitation is still present within the surface cavities despite the fact that there are no cavitation streamers visible in Figure 6.4.

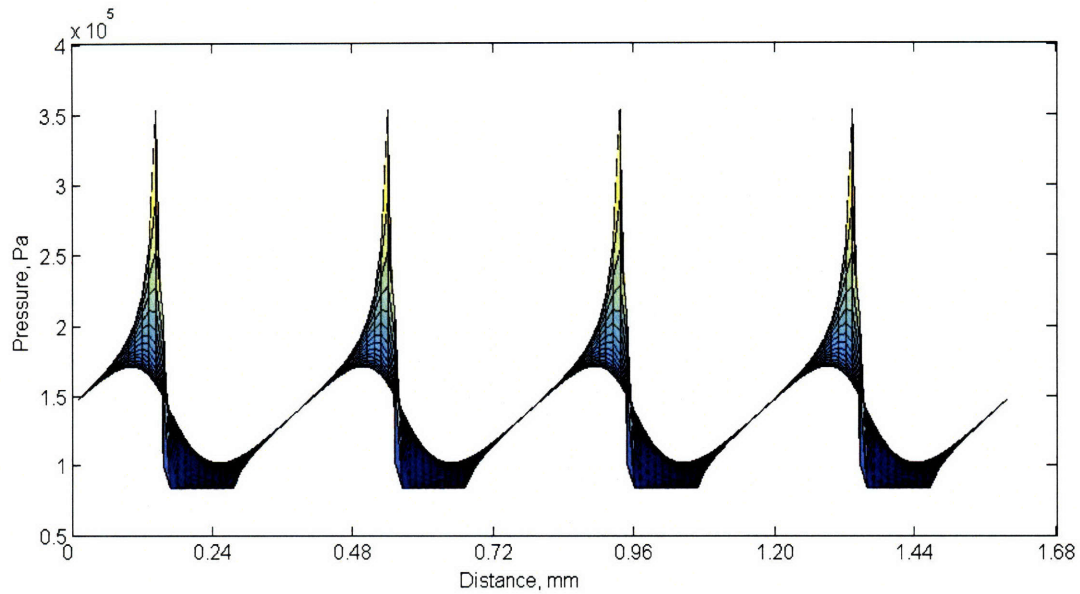


Figure 6.12. Pressure profile at 1.4 mm/s. The pressure profile for a 100 μm 5% surface at a velocity of 1.4 mm/s shows an asymmetric pressure although there are no visible cavitation streamers at this velocity in Figure 6.4.

6.2.3 Cavitation at Low Velocities

The advantage of using direct numeric simulation of the textured surfaces is to confirm that at low speeds where cavitation streamers are not visible, cavitation can still exist and contribute to load support, as predicted by the equations developed in Chapter 5. Equation (5.5) can be used to calculate the velocity at the inception of cavitation on a 100 μm 5% surface at the average radius of the disk, which is 6.7mm, by assuming that the gap is nearly equal to the asperity height since there is no mechanism of load support before cavitation, and the local lubricant viscosity corresponds to a velocity near the transition point from mixed to hydrodynamic lubrication on the Stribeck curve. These assumptions will be carried into the numerical simulation for consistency and

may not match the actual experimental conditions. The resulting velocity from the calculation is 0.9mm/s, as shown in Table 6.1.

At the very inception of cavitation, there will not likely be visible cavitation streamers from the surface, but there will be an asymmetric pressure profile that will result in load support from the surface texturing. To validate the scaling values from equation (5.5), the velocity at the inception of cavitation is entered into the numerical simulation. Figure 6.13 verifies that the numerical simulation supports the scaling equations by indicating that cavitation is present at this velocity. Cavitation streamers are not visible in Figure 6.4 from experimental investigation, however, because the cavities are only partially filled with vapor.

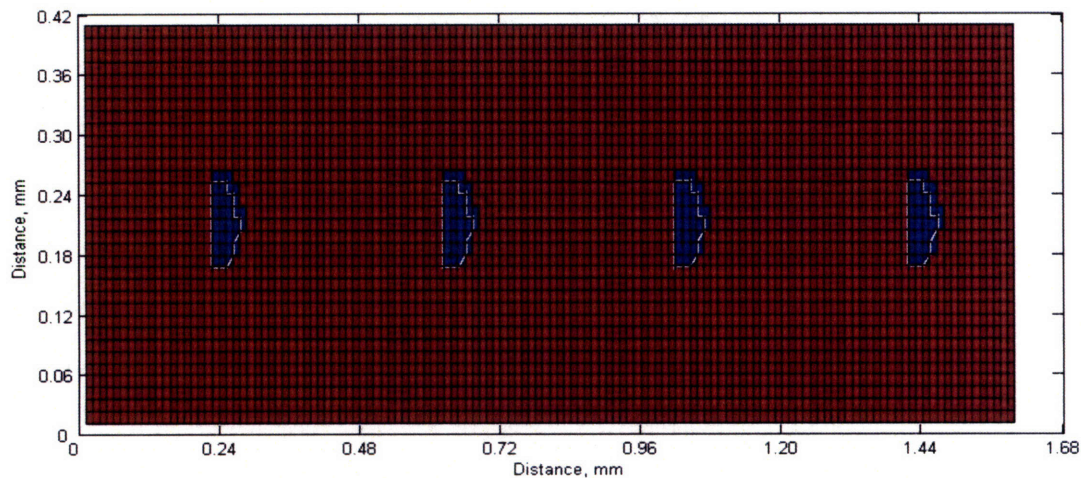


Figure 6.13. Cavitation map at 0.9mm/s. There is evidence of cavitation in numerical simulations at the velocity where theory indicates cavitation should start. This cavitation remains local and is not visible in experiments.

6.2.4 Influence of Radial Pressure Gradients

The numerical simulation not only verifies the existence of cavitation, but it also shows the pressure distribution in both the radial and circumferential directions. It is important to notice that the simulation is performed for a linear sliding system instead of rotating parallel plates. When looking at the midpoint radius of the rotating plates, the scale in the sliding direction is much larger than that of the other two directions, so it is reasonable to assume that there are no curvature effects.

There will likely be a significant difference in the linear and rotational systems if the entire system is modeled instead of only a section of the midpoint radius due to the pressure distribution under the rotating plate. For the rotating system, there is a pressure gradient from the center to the outermost radius because of the very slow velocity at the center and increasing velocity with increasing radius. Corresponding to the increasing velocity is an increasing pressure gradient, as given by equation (5.5). Because fluid flows from high-pressure regions to regions of lower pressure, the lubricant will not tend to flow out from underneath the plate because the pressure gradient will encourage the fluid to flow to the center of the plate to the low-pressure area. In contrast, for the linear system there is no velocity gradient and therefore no corresponding pressure gradient.

Figure 6.9 shows that when surface texturing is added to sliding surfaces, there is not only a pressure gradient as a result of velocity gradient, but there will

also be a radial velocity gradient as a result of the pressure gradient. With a linear sliding system, there is no pressure to resist the lubricant from flowing to areas of lower pressure, which means that the lubricant flows out from underneath of the textured surface. This leads to lubrication starvation underneath of the surface unless there is a system of replenishing the lubricant.

6.3 Summary

This chapter described experiments that verified the existence of cavitation on micro textured surfaces. First, experimental work using the triborheometer and a transparent surface allowed a high-speed camera to record cavitation streamers on both textured and flat surfaces. Then, numerical modeling was presented to theoretically predict local cavitation pockets at low velocities where cavitation cannot be experimentally observed. This experimental and numerical proof of cavitation supports the theory that surface micro texturing improves load support by acting as step bearings because these step bearings result in cavitation that leads to an asymmetric pressure profile and thus added load support.

Now that mechanism of reduced friction for micro textured surfaces has been verified, texture geometry optimization can be explored.

CHAPTER 7: MICRO TEXTURING AND THE STRIBECK DIAGRAM

In order to determine the effect surface micro texturing had on the Stribeck curve, experimental surfaces were fabricated according to the procedures described in Appendix B and tested using the method outlined in Appendix A. Table 7.1 provides a summary of the texture geometries that were fabricated and tested in this study, and Appendix C shows photographs of each surface. Each surface is identified by the texture diameter and area density. Unless otherwise specified, all geometries had circular cross-sections as shown in Figure 7.1, which is rendering of a surface with circular cavities along with a photograph of a surface with 100 μ m diameter cavities. Experimental methods were verified in a previous study of micro textured surfaces [64] and will not be repeated here.

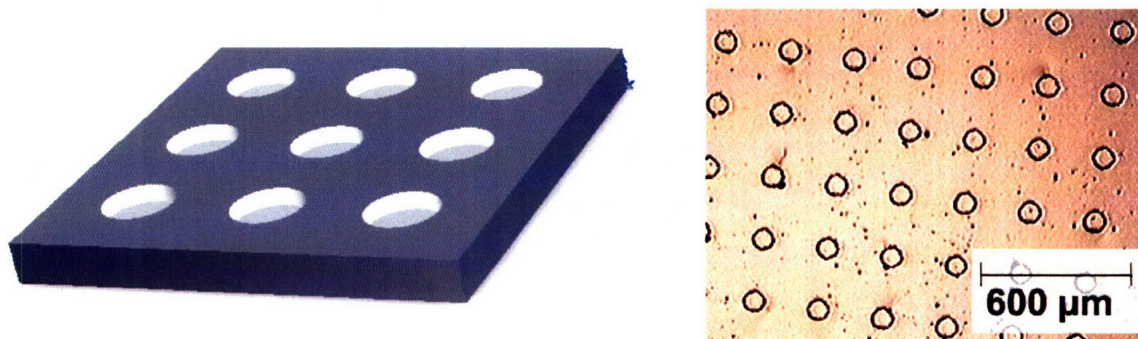


Figure 7.1. Rendering and photo of micro textured surface. Unless otherwise specified, surface cavities are cylindrical with a specified diameter, area density, and depth.

7.1 Exploring Texturing Parameters

In order to verify the theory that micro textured surfaces act as step bearings to develop load support under sliding, lubricated conditions, surfaces with different texturing parameters were tested experimentally. In particular, the cavity depth, diameter, and area density were explored. The depth of the cavity was varied from 17 to 22 μm as measured from the top surface, and the depth tolerance was $\pm 1\mu\text{m}$. The cavity diameter is consistent throughout the depth of the hole as a result of the technique of fabricating the holes by plating around a photoresist post. When the texture geometry is square instead of circular, then the given hole size will be the side length rather than the hole diameter. Due to the accuracy of the diameter at all hole depths, there is an immediate step from the surface to the hole depth, which is very different from the resulting geometry achieved through etching or laser texturing [40]. This difference could result in different fluid mechanics in the region of the inlet step for the two texturing methods. Finally, the are density ϕ , is defined as the total surface area of the textured plate divided by the total surface area of the texture cavities and ranges from 1 percent to 15 percent for this study.

7.2 Effect of Texture on Stribeck Diagram

Chapter 5 derives equation (5.5) for the pressure distribution in a step bearing according to the geometrical parameters of the step. That equation can be applied to a micro textured surface in order to determine the local pressure difference, then the pressure is integrated over the surface to determine the load support due to the added surface texturing. Equation (5.9) calculates the load support per unit width over a single surface cavity considering cavitation area. To determine the effect of micro texturing on the Stribeck diagram, the altered pressure distribution is considered at either the transition point between the boundary and mixed lubrication regimes or the transition point between the mixed and hydrodynamic lubrication regimes. Because the effects of surface micro texturing are not independent of the lubrication regime, it does not make sense to present a modified Gumbel number that normalizes surface texturing parameters. This modification could be appropriate for a more focused, application-specific study.

When examining these transition points on the Stribeck diagram and the effects of applied surface micro texturing, the effects of the natural surface texture must also be considered. In Chapter 6, Figure 6.4 and Figure 6.6 showed that cavitation occurred on both the flat and textured surfaces, and it was suggested the surface asperities could act as micro step bearings. A complete understanding of the individual asperity effects would require a statistical study of the distribution of surface asperities, and it is not within the scope of this thesis.

Instead, the bulk effect of the surface asperities will be approximated and described in the following sections.

7.2.1 Boundary to Mixed Regime Transition

Boundary lubrication is a result of the interfacial lubricant no longer supporting any of the applied load between the sliding surfaces. When transitioning from boundary to mixed lubrication, the lubricant begins to support some of the applied load, while the rest is still supported by asperity contact. In order to establish this load support, there must be sufficient relative sliding velocity. For textured surfaces, the load support is a result of the lubricant moving over a surface cavity where the local pressure drops low enough for the lubricant to cavitate and thus produce an asymmetric pressure distribution over the surface.

The role of the surface asperities is neglected at this transition point because the load-carrying capability of the entire surface is irrelevant. Only the pressure drop over the surface cavity for a particular geometry is required to determine the scaling parameters for the textured surface.

To determine the effect of surface texturing at the transition point from boundary to mixed lubrication, the Gumbel number at which the transition occurs can be determined by calculating the velocity at the inception of cavitation within the surface cavity. The velocity is found by starting with equation (5.5) with the geometric parameters defined by Figure 5.3 and determining that at the transition

point, the minimum pressure is just equal to the cavitation pressure p_{cav} , and it is symmetric with the maximum pressure p_{max} about the applied stress σ , so that $(p_{max} + p_{cav}) = 2\sigma$. The velocity at the transition can be calculated as

$$\Omega_{bdy \rightarrow mixed} R = \frac{(p_{cav} - \sigma)(h_0^3 L_c + h_c^3 L_0)}{3\eta L_c L_0 (h_0 - h_c)} \quad (7.1)$$

7.2.2 Mixed to Hydrodynamic Transition

The transition point from hydrodynamic to mixed lubrication can be approximated as the point at which the gap clearance between the two surfaces reaches the height of the tallest surface asperities. When two surfaces are transitioning from the hydrodynamic into the mixed lubrication regime, reaching this height leads to surface-to-surface contact, which is characteristic of the mixed lubrication regime. Unlike the transition from mixed to boundary lubrication, the contribution of the surface asperities on the flat surface to load support cannot be neglected, so the load support of both the surface asperities and the applied surface texture must be considered to find the transition point velocity for different texture parameters.

For a particular surface geometry, the equation for the pressure profile has 3 main variables: applied normal stress σ , gap height between the two surfaces h_0 , and sliding velocity, U . The applied normal stress is maintained at a constant value for this study, so there are only 2 remaining variables. For this transition point, though, the gap height is a known variable. Regardless of the surface geometry, the gap at the transition point is equal to the tallest surface asperity, so

there is only one variable in the pressure equation, which is the transition velocity. Equation (5.7) can therefore be written for the entire surface rather than just one hole, and it is a function of only one variable for any surface geometry at the transition point between the hydrodynamic and mixed lubrication regimes

$$\frac{W}{B} = \Lambda * (\Omega R_{avg}) + P_{cav} (2\pi R_{avg}) \quad (7.2)$$

Λ is a constant that represents the surface geometry. For the flat surface, this constant will be called Λ_0 and is an unknown that must be found experimentally so that the load support contribution from the surface asperities alone is determined. A standard tribology experiment as described in Chapter 3 can be performed so that the coefficient of friction at each rotational velocity determined. The velocity at the lowest coefficient of friction represents the velocity at the transition point. This velocity Ω , along with the applied load W , per unit width B , are substituted into equation (7.3) in order to determine the geometric pressure parameter Λ_0 . The flat surface geometric parameter is equal to

$$\Lambda_0 = \frac{1}{\Omega R_{avg}} \left[\frac{W}{B} - P_{cav} (2\pi R_{avg}) \right] \quad (7.3)$$

Once the flat surface contribution is determined, the geometric parameter for the textured surface Λ_T , is found by once again assuming a constant applied normal stress and a gap height equal to the height of the tallest asperity. These assumptions along with the geometric dimensions for the particular textured

surfaces can be entered into the following equation to find the appropriate constant

$$\Lambda_T = 2\pi R_{avg} \left[\frac{3\eta L_c L_0 (h_0 - h_c)}{(h_0^3 L_c + h_c^3 L_0)} \right] \quad (7.4)$$

The total load support is calculated using the average radius of the plate, $R_{avg} = \frac{2}{3}R$ as the width variable and the area density of surface texturing ϕ , to estimate the surface area covered by the surface asperities compared to the applied texturing. Equation (7.2) can now be written to include pressure contributions as a function of the area density from both the cavities and the flat surfaces

$$W = R_{avg} \left[(\phi \Lambda_T + (1 - \phi) \Lambda_0) \Omega R_{avg} + 2\pi R_{avg} P_{cav} \right] \quad (7.5)$$

When this equation is solved to find the velocity at the transition from the hydrodynamic to the mixed lubrication regime for a constant applied normal force, the velocity is determined to be

$$\Omega_{mixed \rightarrow hydro} R = \frac{W - 2\pi R_{avg}^2 P_{cav}}{R_{avg} [\phi \Lambda_T + (1 - \phi) \Lambda_0]} \quad (7.6)$$

7.3 Results and Discussion

Figure 7.2 illustrates the effect of surface texturing in the different lubrication regimes for 5 different surfaces compared to a flat, non-textured surface. Equations for the added load support due to the surface texturing have

been discussed in this chapter, and predictions for the transition velocities were described. Equations (7.1) and (7.6) were solved in Matlab with the appropriate geometric dimensions for 6 different textured surfaces to determine the effectiveness of the assumed equations for determining the effect of surface texturing on the Stribeck diagram. A summary of the surfaces used in this study is given in Table 7.1 along with the geometric pressure parameters calculated from equation (7.3) for the flat surface and equation (7.4) for the textured surfaces.

Table 7.1. Summary of the textured nickel surfaces in this study.

Surface	Depth, $h_c - h_0$ (μm)	Distance between 2 cavities, L_0 (μm)	Geometric pressure parameter, Δ ($\text{N}\cdot\text{s}/\text{m}^2$)
Control	(na)	(na)	1.76×10^5
50μm 1%	18	441	1.25×10^5
50μm 2.5%	17	280	1.39×10^5
50μm 5%	18	198	1.25×10^5
100μm 5%	17	395	2.78×10^5
100μm 10%	20	280	1.99×10^5
125μm 15% (squares)	23	319	2.06×10^5

For the analyses in this section, the lubricating fluid was STP Oil Treatment, and the cavitation pressure for STP was approximated as 0.85 atm. This approximation is based on commonly accepted values in the automotive industry with experimental verification given in Chapter 6.

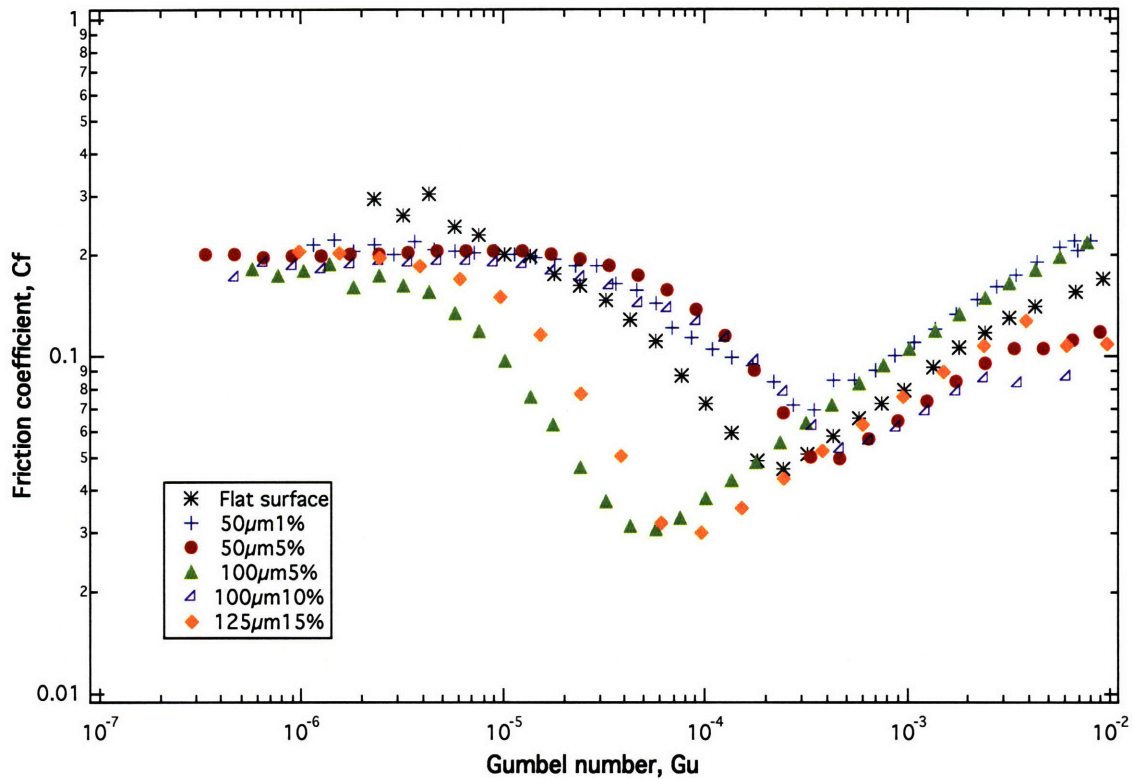


Figure 7.2. Surface texturing effects for 5 different surfaces. These surfaces are compared to a flat control surface to show the effect that surface texturing has on the Stribeck diagram.

7.3.1 Transition from Mixed to Boundary Lubrication

At the transition from the boundary to the mixed lubrication regime, the lubricant begins to cavitate and therefore the applied normal force on the surfaces transitions from being only supported by surface-to-surface contact to being partially supported by the lubricant. Equation (7.1) describes the predicted velocity at this point for a particular surface geometry, and Figure 7.3 shows the prediction for 6 different surfaces along with the corresponding experimental data.

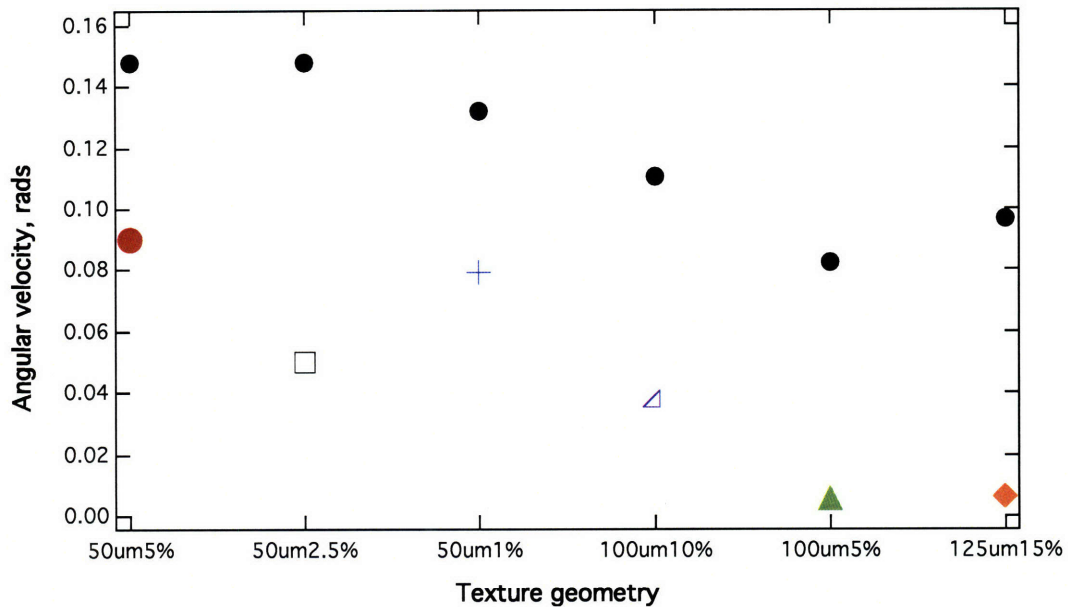


Figure 7.3. Comparison of experimental data and data predicted from theory for the transition from boundary to mixed lubrication.

The prediction scales well with the experimental data, but there is a 40% difference between the actual value and the predicted value of the transition velocity. The main reason for this difference is that the normal stress that the fluid experiences is not the same as the applied normal stress. The force applied to the surface is supported almost entirely by the surface asperities, so the real force on the lubricant is only a fraction of the applied force. If the statistical distribution of the surface asperities is known, then equations developed by Greenwood and Tripp [52] and Mikic [78] can be applied to determine the exact value of the applied normal stress.

Another possible source of error in the calculation of the transition velocity is in the length of the contacting surface L_0 , where there is a drop in the lubricant pressure. Due to contacting surface asperities, contacting points will interrupt the

distance between surface cavities and therefore the pressure drop may not be linear over these surfaces. A final source of error is in the calculation of cavitation pressure. The theoretical calculations do not include corrections for side flow, as described in Chapter 5. This side flow reduces the generated pressure at the high-pressure end of the step. In addition to slide flow, an illustration of the flow over a surface cavity replicated from Shen and Floryan [79] is shown in Figure 7.4 and illustrates that the flow of a lubricant over a surface cavity with a sharp corner could result in flow instabilities. These instabilities, which are also discussed by McKinley [80] for elastic fluids, will change the local pressure distribution and could result in cavitation before the velocity predicted by only the continuity and momentum equations.

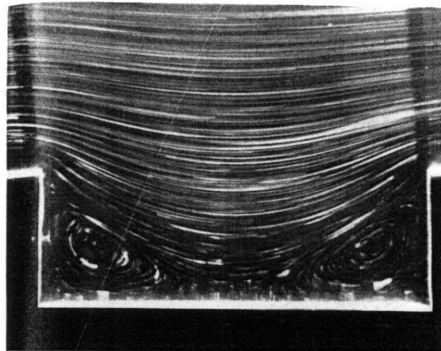


Figure 7.4. Illustration of fluid flow over a cavity replicated from Shen and Floryan [79]. The fluid used in the illustration was glycerin seeded with aluminum dust at a Reynold's number of 0.01 based on cavity height. The aspect ratio b/h is equal to 3.

The experimental and theoretical velocity predictions show good scaling agreement, which indicates that the errors in the velocity calculations are similar for all surfaces. Equation (7.1) is therefore successful at capturing the

relationship between surfaces with different surface textures and can successfully be used to determine the optimum geometric dimensions of surface texturing to delay entering the boundary lubrication regime for surfaces that operate in the mixed lubrication regime.

7.3.2 Transition from Hydrodynamic to Mixed Lubrication Regimes

The transition from the hydrodynamic lubrication regime to the mixed lubrication regime is characterized by the initial contact of surface asperities between the two sliding surfaces and therefore the lubricant thickness is equal to the height of the tallest surface asperity. Equation (7.6) gives an equation to calculate the velocity at which this transition occurs with respect to a flat, non-textured surface for the same material, surface roughness, surface waviness, and lubricant. Figure 7.5 shows a comparison of this theoretical calculation compared to experimental data from Figure 7.2 for 6 different textured surfaces.

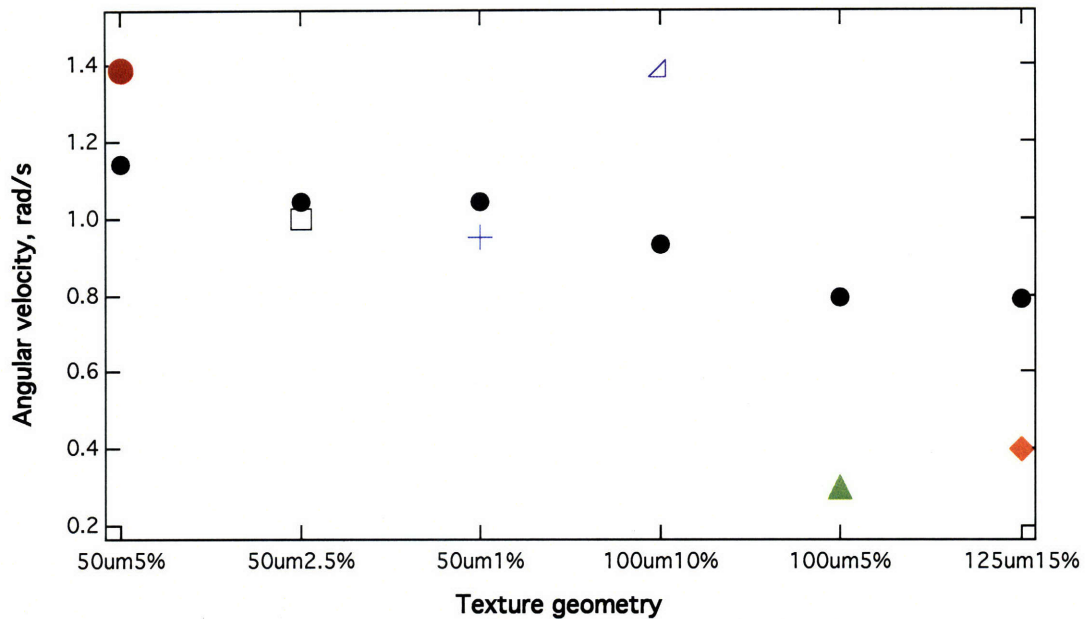


Figure 7.5. Comparison of experimental data and data predicted from theory for the transition point from mixed to hydrodynamic lubrication.

The theoretical and experimental data show basic trends and scaling, indicating the success of the theoretical analysis in capturing the critical mechanisms of load support for micro textured surfaces. It is particularly interesting to note that some of the textured surfaces transitioned from hydrodynamic to mixed lubrication before the flat, non-textured surface, and that is successfully captured in the theoretical analysis. Physically, for this to happen, the applied surface texturing must be less efficient at producing load support than the small-scale surface asperities. Table 7.1 shows the values of the different geometric parameters introduced in equation (7.2) for the different textured surfaces in Figure 7.2. The geometric pressure parameter for the flat surface is higher than the parameters for all of the textures with a 50 μ m hole diameter. This indicates that the added pressure due to the step-effect in these holes is less than the pressure would be on just a flat surface. Therefore, the load-bearing

capability is actually lower for the 50 μ m surfaces than for the flat surface. Figure 7.2 supports these conclusions by showing that the control surface transitions to the mixed lubrication regime at a lower velocity than the two 50 μ m diameter surfaces shown.

The main sources of error in the calculations of the transition velocity from the hydrodynamic to mixed lubrication regime are corrections for side-flow and flow instabilities, as shown in Figure 7.4. Flow instabilities at the low-pressure entrance region to the cavity can allow cavitation pressures higher than those calculated by the continuity and momentum equations, and side-flow can reduce the amount of pressure generated at the high-pressure exit-region of the cavity.

In addition to the side flow, equation (7.6) does not calculate the resulting amount of vapor in each cavity at the transition velocity. In order to rebuild pressure in a cavity, there must be lubricant in the fluid-phase to resist flow. Figure 7.6 is an illustration of a cavity that is partially filled with vapor and the corresponding pressure distribution. When a cavity is completely filled with lubricant in the vapor-phase, it cannot rebuild pressure and thus cannot help to support an applied load. For rotating parallel plates, this effect is less evident because of the velocity gradient from the center to the outer rim of the plate.

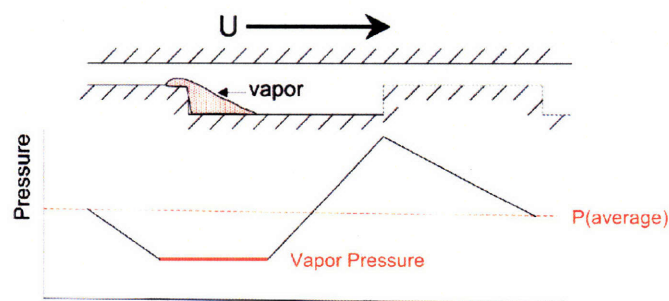


Figure 7.6. Illustration of pressure profile with cavitation. As the hole fills with vapor, there is less area for pressure to rebuild and support the applied load.

7.4 Optimizing Surface Texture

Now that scaling equations have been found and verified, they can be used as design tools to determine the how cavity dimensions affect the friction coefficient for a given set of running conditions. Typically, mechanical devices are designed to remain in the hydrodynamic lubrication regime to avoid surface contact and wear. Equations (7.1) and (7.6) present scaling equations to help determine the geometric parameters that will allow the lowest velocity before transitioning from one lubrication regime to another. These equations can also be arranged to determine to critical applied load or lubricant viscosity.

The scaling parameters were calculated for a surface with a 15N normal load and 7 Pa·s viscosity lubricants, to determine which parameters would delay transition into the mixed lubrication regime the longest. The calculations do not indicate what the resulting friction coefficient would be, but from the Stribeck diagram, we know that the friction coefficient is smallest at velocities close to the transition point from hydrodynamic to mixed lubrication. It is also important to note that that the scaling equations do not give a precise calculation for the transition velocity, and reasons for precision errors were presented. Instead, to attain precise velocity calculations, the geometry must be first determined using the scaling equations, then numerical simulation can be used to determine the velocity.

The following graphs show the scaling for three different geometric parameters at the transition point from hydrodynamic to mixed lubrication: cavity

depth, cavity diameter, and area density of texturing. Each graph shows the effects on one parameter while holding the other two constant, as calculated from equation (7.6). Unless the parameter is changing in the graph, the area density is maintained at 5%, the cavity diameter is 100 μm , and the cavity depth is 16 μm . For these particular conditions, changing cavity depth and area density has a much more significant effect on the transition velocity than changing the cavity diameter. A similar analysis can be performed for the transition from mixed to boundary lubrication.

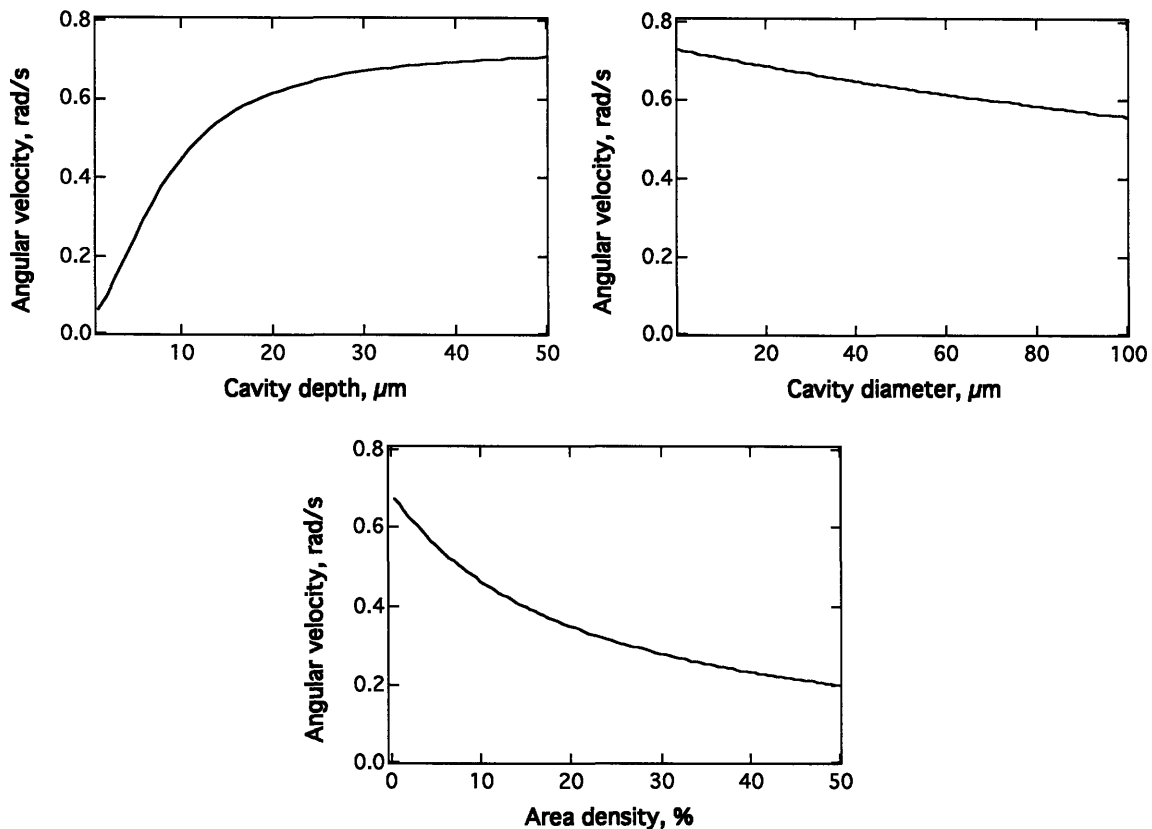


Figure 7.7. Optimization of texturing geometry. 2 geometric parameters are kept constant to show the effect of the third parameter on the transition velocity from mixed to hydrodynamic lubrication. When kept constant, the texturing parameters are 100 μm diameter, 5% area density, and 16 μm cavity depth.

For a more general understanding of the effects of texturing geometry on the transition velocity, contour plots can be developed to represent the effects of 2 different texturing parameters while only holding one parameter constant. These plots are shown in Figure 7.8.

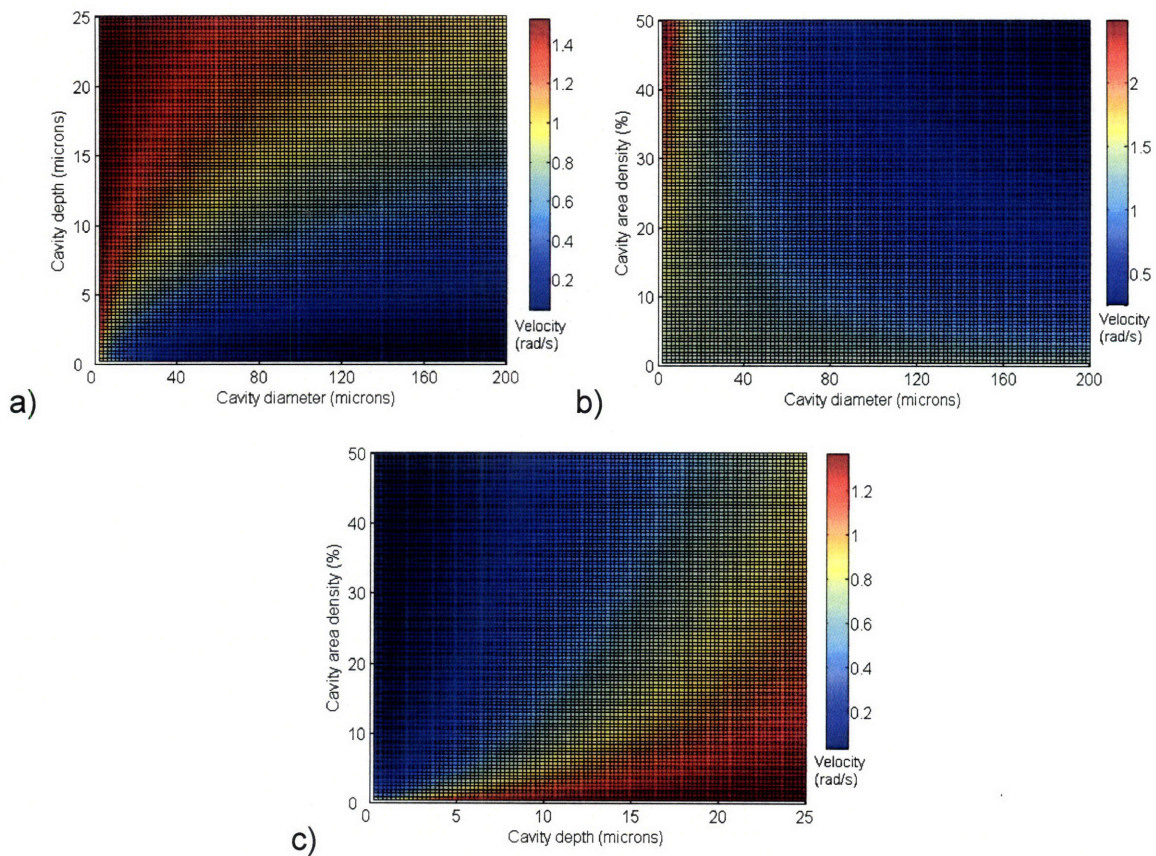


Figure 7.8. Transition velocity contours. The transition velocity from the hydrodynamic to mixed lubrication regime is shown as a function of 2 variables in each plot. a) Cavity area density is maintained at 5%, b) cavity depth is maintained at 16 μ m, and c) cavity diameter is maintained at 100 μ m.

7.5 Summary

The scaling effects of surface micro texturing have been captured in equations (7.1) and (7.6). Comparison with experimental data, as shown in Figure 7.3 and Figure 7.5, show that the predicted scaling equations effectively capture the mechanisms of altered friction for surface texturing. Using the developed scaling equations, it is now possible to determine how the surface texture geometry affects the friction coefficient to improve decisions on geometric texturing parameters for tribological design.

CHAPTER 8: CONCLUSIONS AND RECOMMENDATIONS

Tribology is a subject that touches systems ranging from nano-scale engineered surfaces of magnetic storage devices to earthquakes and geophysical phenomena associated with the Earth's shifting crust. The serious consequences of friction and wear are explained in a 1994 study, which concludes that 40% of the total fuel energy in automotive engines is consumed by engine friction [7]. In bio-tribology, the lifetime of implanted artificial hips and knees are limited by surface wear. Looking at the consequences of tribology in fiscal terms, PhysicsWorld reports that nearly 10% of an industrialized nation's gross national product is spent on "direct costs of friction and wear" [10].

In tribological design there are currently two main techniques that are being used to reduce friction between sliding, lubricated surfaces: adding viscoelasticity to lubricants and adding a micro-scale texture to surfaces. These techniques have been shown in studies to reduce friction by as much as 40% and nearly double the service life of mechanical seals [41], but very little work has been done to optimize the effects of these two friction reduction techniques.

The work presented in this thesis provides new insights into understanding the physical mechanisms governing sliding, lubricated friction. In particular, the roles of lubricant elasticity and surface micro texturing have been investigated, and the related consequences for the Stribeck diagram were determined. These results are necessary to design new frictional systems using elastic lubricants or to determine more effective geometries for low-friction micro textured surfaces.

8.1 Lubricant Elasticity

Advances in lubrication technology have led to the development of lubricants that are more complex than those that were available to Gumbel when he developed the Stribeck diagram in 1914. These new lubricants often have added long-chain polymers that require viscoelastic analysis because of the shear-thinning viscosity and added normal stresses that are described and quantified in Chapter 4. Chapter 5 describes how shear thinning effects the viscosity term in the Gumbel number and generated normal stresses in the lubricant add an extra term to applied normal stress. Each of these new viscoelastic properties has a strong effect on the Stribeck curve, and in order to normalize these new lubricants with Newtonian lubricants, a new modified

Gumbel number was developed, $Gu' = \frac{\eta(\dot{\gamma})\Omega}{\sigma(1 + \alpha De)}$. This new number

allows the Stribeck curve can be used as a design tool to determine the appropriate Newtonian and non-Newtonian lubricant properties for a given set of system running conditions. “Tuning” the lubricant to match the running

conditions in this way can both improve the system wear and increase the efficiency by decreasing the energy due to frictional losses.

8.2 Surface Micro Texturing

Chapter 5 described the fluid mechanics of a micro textured parallel surface under full-film lubrication conditions as a series of step-bearings. Each texture was analyzed individually, and its contribution to load support was considered. This analysis concluded that in order for the surface to act as series of micro-step bearings, there must be cavitation to break the symmetry of the pressure profile so that there is a net positive load support.

The cavitation was verified using both experimental and numerical techniques. An experimental setup was designed that allowed a micro textured surface to rotate relative to a glass prism. The textured surface/lubricant interaction was recorded using a high-speed camera, and cavitation streamers were visible as the rotational velocity increased. Thus, it is possible to conclude that cavitation does exist on micro textured surfaces, but the cavitation streamers were not visible at lower velocities, where the Stribeck diagram indicates that there should still be load support on the textured surface.

Since local cavitation within the surface cavities was not visible without image magnification or other visualization techniques, numerical simulations were used to confirm the existence of cavitation at low velocities. Simulations that were previously developed to detect cavitation conditions in lubricant films and predict the resulting pressure profiles were used with surface maps that

reflected the experimental micro textured geometries. When run according to the experimental conditions, the numerical simulations indicated that the surface cavity was fully cavitated at velocities where cavitation streamers were visible, but they were less than fully cavitated at lower velocities. There was still sufficient evidence of cavitation in the surface cavities at very low velocities, where the theoretical predictions of Chapter 5 indicated the inception of cavitation. Therefore, although the cavitation was not visible using experimental techniques, it is evident in the numerical simulations.

After verifying the existence of cavitation, its role in improving lubrication conditions on micro textured surfaces was considered in Chapter 5, and scaling arguments were developed that indicated the contribution of the different geometric and dynamic parameters to the load support. These arguments were shown to depend on the lubrication regime, and predictions for the transition points were presented. For the transition point from boundary to mixed lubrication, the expected velocity scaled according to equation (7.1), which is repeated below:

$$\Omega_{bdy \rightarrow mixed} R = \frac{(p_{cav} - \sigma)(h_s^3 c + h_c^3 s)}{3\eta cs(h_s - h_c)}.$$

The transition point from mixed to hydrodynamic lubrication was based on slightly different lubrication conditions and was presented in to scale according to equation (7.6), which is repeated here for completeness:

$$\Omega_{mixed \rightarrow hydro} R = \frac{W - \pi R_{avg}^2 P_{cav}}{R_{avg} [\phi M + (1 - \phi) N]}.$$

Experimental data from micro textured nickel surfaces tested with STP Oil Treatment as the interfacial lubricant supported the scaling parameters, and further discussion was presented on the nature of friction in the lubrication regimes.

Chapter 6 concluded that cavitation does exist, and it is a major source of load support for micro textured surfaces. The new scaling equations can be used to predict the effect of individual geometric parameters on the lubrication regime transition velocities. Understanding these effects can lead to designing more effective surface textures. The results from correlating these scaling equations to experimental data suggest that a numerical simulation is not needed in order to design micro textured surfaces, rather, the simple scaling arguments are sufficient to determine appropriate surface texture geometries.

8.3 Recommendations

To extend and complete this research, it is recommended that the effects of micro texturing on surface wear be fully evaluated to determine the consequences of surface micro texturing over the lifetime of the surface. Wear scars were visible after friction testing each surface if the interaction was allowed to pass through hydrodynamic lubrication and enter into the mixed lubrication regime where the surface experienced surface-to-surface contact. Although the wear conditions are unknown, Tian, Saka, and Suh [27] suggest that the

texturing pattern could help to trap wear particles and keep them from further damaging the contacting surfaces.

In addition, it is suggested that the lubricant cavitation and film thickness be probed further using LIF techniques, such as those developed by Hidrovo et al [81]. The current experimental setup for cavitation visualization would have to be modified so that an etched glass surface acted as the textured surface and was positioned on top of the beam-splitter as the non-rotating surface. A standard parallel-plate rheometer head could be used as the rotating surface. Using this experimental setup, fluorescent dye could be mixed with the lubricant so that the lubricant thickness could be measured while the experiment was running. This measurement would give information about both the exact gap height between the surfaces and the existence of locally cavitating areas in the lubricant. This technique allows detection of cavitation at the moment of inception rather than waiting until streamers are formed.

8.4 Final Remarks

The research presented for this thesis provides a systematic, fundamental study of lubricant elasticity and micro texturing and explains the mechanisms for the altered frictional profile on the Stribeck diagram. As a result of this research, designers can better optimize the effects surface micro texturing to a particular surface and application in order to reduce friction and therefore reduce the energy dissipated in the system. Moreover, this research could potentially be a step forward towards building more efficient systems that have reduced energy consumption and longer expected service periods.

REFERENCES

1. Kessler, D.A., *A new crack at friction*. Nature, 2001. **413**: p. 260-261.
2. Ancy, C., *Plasticity and geophysical flows: A review*. Journal of Non-Newtonian Fluid Mechanics, 2007. **143**(1-3): p. 4-35.
3. Israelachvili, J., *Tribology of Ideal and Non-Ideal Surfaces and Fluids*, in *Fundamentals of Tribology and Bridging the Gap between Macro- and Micro/Nanoscales*, B. Bhushan, Editor. 2001, Kluwer Academic Publishers: Netherlands. p. 631-650.
4. Jabbarzadeh, A., J.D. Atkinson, and R.I. Tanner, *Nanorheology of molecularly thin films on n-hexadecane in Couette shear flow by molecular dynamics simulation*. J. Non-Newtonian Fluid Mechanics, 1998. **77**: p. 53-78.
5. Shi, B., et al., *Tribological performance of alternative bearing materials for artificial joints*. Wear, 2003. **255**: p. 1015-1021.
6. Gispert, M.P., et al., *Friction and wear mechanisms in hip prosthesis: Comparison of joint materials behaviour in several lubricants*. Wear, 2006. **260**: p. 149-158.
7. Nakada, M., *Trends in engine technology and tribology*. Tribology International, 1994. **27**(1): p. 3-8.
8. Vicuna, S., *Exploring Greenhouse Gas Reduction Options for Automobiles: A Report on the International Vehicle Technology Symposium*. 2004, Environmental Defense.
9. AudiAG, *Light at the End of the Cylinder*, in *AudiWorld*. 2004.
10. Taylor, I., *Car lubricants: fact and friction*, in *PhysicsWorld*. February 2002.
11. Dowson, D., *History of Tribology*. 2nd ed. 1998, London: Professional Engineering Publishing Ltd. 304-359.
12. Spikes, H., *The History and Mechanisms of ZDDP*. Tribology Letters, 2004. **17**(3): p. 469-489.
13. Scott, G., *History of Engine Oil*. 2005, Volvo.
14. Taylor, T.I. and R.C. Coy, *Improved fuel efficiency by lubricant design: a review*. Proceedings of the Institution of Mechanical Engineers Part J- Journal of Engineering Tribology, 2000. **214**(J1): p. 1-15.

15. Kono, R.N., et al., *Rheology of perfluoropolyether lubricants*. IEEE Transactions on Magnetics, 2001. **37**(4): p. 1827-1829.
16. Freeman, M., et al., *Friction, wear, and lubrication of hydrogels as synthetic articular cartilage*. Wear, 2000. **241**: p. 129-135.
17. Okrent, E.H., *The Effect of Lubricant Viscosity and Composition on Engine Friction and Bearing Wear*. ASLE Transactions, 1961. **4**: p. 97-108.
18. Williamson, B.P., et al., *Viscoelastic properties of multigrade oils and their effect on journal-bearing characteristics*. Journal of Non-Newtonian Fluid Mechanics, 1997. **73**(1-2): p. 115-126.
19. Akyildiz, F.T. and H. Bellout, *Viscoelastic lubrication with Phan-Thein-Tanner fluid (PTT)*. J. of Tribology, 2004. **126**(2): p. 288-291.
20. Tichy, J.A., *Hydrodynamic Lubrication with the Convective Maxwell Model*. Journal of Tribology, 1996. **118**(2): p. 344-349.
21. Glavatskih, S.B. and D.M.C. McCarthy, *Hydrodynamic Performance of a Thrust Bearing with Micropatterned Pads*. Tribology Transactions, 2005. **48**: p. 492-498.
22. Pettersson, U. and S. Jacobson, *Influence of surface texture on boundary lubricated sliding contacts*. Tribology International, 2003. **36**(11): p. 857-864.
23. Bolander, N.W. and F. Sadeghi, *Deterministic Modeling of Honed Cylinder Liner Friction*. Tribology Transactions, 2007. **50**(2): p. 248 - 256.
24. Lewis, P.R. and C.W. McCutchen, *Mechanism of Animal Joints: Experimental Evidence for Weeping Lubrication in Mammalian Joints*. Nature, 1959. **184**: p. 1284 - 1285.
25. Bossler, R.B., *Boundary Layer Lubrication Behavior*. Lubrication Engineering, 1965. **21**: p. 104-111.
26. Hamilton, D.B., J.A. Walowit, and C.M. Allen, *A theory of lubrication by micro-irregularities*. Trans. ASME Journal of Basic Engineering, 1966. **88**: p. 177-85.
27. Tian, H., N. Saka, and N. Suh, *Boundary Lubrication Studies on Undulated Titanium Surfaces*. Tribology Transactions, 1989. **32**(3): p. 289-296.
28. Blatter, A., et al., *Lubricated sliding performance of laser-patterned sapphire*. Wear, 1999. **232**: p. 226-230.
29. Steinhoff, K., W. Rasp, and O. Pawelski, *Development of deterministic-stochastic surface structures to improve the tribological conditions of sheet forming processes*. J. of Materials Processing Tech., 1996. **60**: p. 355-361.
30. Cogdell, J.D., et al., *Surface Texture Effects in Thin Film Lubrication of Steel by Silicones*. ASLE Transactions, 1986. **30**(2): p. 141-148.

31. Yu, X.Q., S. He, and R.L. Cai, *Frictional characteristics of mechanical seals with a laser-textured seal face*. J. of Materials Processing Tech., 2002. **129**: p. 463-466.
32. Lo, S. and T. Horng, *Lubrication Permeation From Micro Oil Pits Under Intimate Contact Condition*. Journal of Tribology, 1999. **121**: p. 633-638.
33. Geiger, M., S. Roth, and W. Becker, *Influence of laser-produced microstructures on the tribological behaviour of ceramics*. Surface and Coatings Tech, 1998. **100-101**: p. 17-22.
34. Tønder, K., *Dynamics of rough slider bearings: effects of one-sided roughness/waviness*. Tribology International, 1996. **29**(2): p. 117-122.
35. Tønder, K., *Hydrodynamic effects of tailored inlet roughnesses: extended theory*. Tribology International, 2004. **37**: p. 137-142.
36. Tønder, K., *Inlet roughness tribodevices: dynamic coefficients and leakage*. Tribology International, 2001. **34**: p. 847-852.
37. Brajdic-Mitidieri, P., et al., *CFD Analysis of a Low Friction Pocketed Pad Bearing*. J. of Tribology, 2005. **127**: p. 803-812.
38. Olver, A.V., et al., *'Inlet suction', a load support mechanism in non-convergent, pocketed, hydrodynamic bearings*. Proc. Instn. Mech. Engrs, Part J, 2006. **220**: p. 105-108.
39. Etsion, I. and L. Burstein, *A Model for Mechanical Seals with Regular Microsurface Structure*. Tribology Transactions, 1996. **39**(3): p. 677-683.
40. Etsion, I., Y. Kligerman, and G. Halperin, *Analytical and Experimental Investigation of Laser-Textured Mechanical Seal Faces*. Tribology Transactions, 1999. **42**(3): p. 511-516.
41. Etsion, I., *State of the Art in Laser Surface Texturing*. J. of Tribology, 2005. **127**.
42. Bhushan, B., ed. *Modern Tribology Handbook*. Vol. 1. 2001, CRC Press: New York.
43. Meyer, E., et al., *Nanoscience: Friction and Rheology on the Nanometer Scale*. 1998, Singapore: World Scientific.
44. Luengo, G., J. Israelachvili, and S. Granick, *Generalized effects in confined fluids: new friction map for boundary lubrication*. Wear, 1996. **200**: p. 328-335.
45. Cuilli, E., *Friction in Lubricated Contacts: From Macro- to Microscale Effects*, in *Fundamentals of Tribology and Bridging the Gap between the Macro- and Micro/Nanoscales*, B. Bhushan, Editor. 2001, Kluwer Acad. Publishers: Netherlands. p. 725-734.
46. Khonsari, M.M. and E.R. Booser, *Applied Tribology: Bearing Design and Lubrication*. 2001, NY: Wiley & Sons, Inc.

47. Bird, R.B., R.C. Armstrong, and O. Hassager, *Dynamics of Polymeric Liquids*: 2nd ed. 1987, New York: Wiley.
48. Liu, Y., et al., *EHL simulation using the free-volume viscosity model*. Tribology Letters, 2006. **23**(1): p. 27-37.
49. Torrence, A.A., *A method for calculating boundary friction and wear*. Wear, 2005. **258**: p. 924-934.
50. Patir, N. and H.S. Cheng, *An average flow model for determining effects of three-dimensional roughness on partial hydrodynamic lubrication*. ASME J. of Lubrication Technology, 1978. **100**: p. 12-17.
51. Kovalchenko, A., et al., *The Effect of Laser Texturing of Steel Surfaces and Speed-Load Parameters on the Transition of Lubrication Regime from Boundary to Hydrodynamic*. Tribology Transactions, 2004. **47**: p. 299-307.
52. Greenwood, J.A. and J.H. Tripp, *The Contact of Two Nominally Flat Rough Surfaces*. Proc. Instn. Mech. Engrs, 1970. **185**: p. 625-633.
53. Furey, M.J., *Metallic Contact and Friction between Sliding Surfaces*. ASLE Transactions, 1961. **4**(1): p. 1-11.
54. Furey, M.J., *Surface temperature in sliding contact*. ASLE Transactions, 1964. **7**: p. 133-146.
55. Müller, M., et al., *The Design of Boundary Film-Forming PMA Viscosity Modifiers*. Tribology Transactions, 2006. **49**: p. 225-232.
56. Fay, J.A., *Introduction to Fluid Mechanics*. 1994, Cambridge: MIT Press.
57. McKinley, G.H. and A. Tripathi, *How to extract the Newtonian viscosity from capillary breakup measurements in a filament rheometer*. J. Rheology, 2000. **44**(3): p. 653-670.
58. Trouton, F.T., *On the Coefficient of Viscous Traction and Its Relation to that of Viscosity*. Proc, Royal Society, 1906. **A77**: p. 426-440.
59. Papageorgiou, D.T., *On the breakup of viscous liquid threads*. Phys. Fluids, 1995. **7**(7): p. 1529-1544.
60. McKinley, G.H., *VISCO-ELASTO-CAPILLARY THINNING AND BREAK-UP OF COMPLEX FLUIDS*, in *Rheology Reviews*, D.M. Binding and K. Walters, Editors. 2005. p. 1-48.
61. Rodd, L.E., et al., *Capillary break-up rheometry of low-viscosity elastic fluids*. Applied Rheology, 2005. **15**(1): p. 12-27.
62. Green, M.A. and C.A. Brockley, *Viscoelastic effects in boundary lubrication*. Nature, 1974. **251**: p. 306-307.
63. Sawyer, W.G. and J.A. Tichy, *Non-Newtonian lubrication with the second-order fluid*. Journal of Tribology-Transactions of the Asme, 1998. **120**(3): p. 622-628.

64. Hupp, S.J., *A Tribological Study of the Interaction between Surface Micro Texturing and Viscoelastic Lubricants*. 2004, MIT: Cambridge, MA.
65. Astarita, G. and G. Marrucci, *Principles of non-Newtonian Fluid Mechanics*. 1974, London: McGraw-Hill.
66. Rudisill, J.W. and P.T. Cummings, *Brownian dynamics simulation of model polymer fluids in shear flow. I. Dumbbell models*. *J. Non-Newtonian Fluid Mechanics*, 1992. **41**(3): p. 275-288.
67. Bai, M. and K. Kato, *Analysis of Contact Deformation and Stiction Between Textured Disk and Textured Slider*. *J. of Tribology*, April 2001. **123**: p. 350-357.
68. Brizmer, V., Y. Kligerman, and I. Etsion, *A Laser Surface Textured Parallel Thrust Bearing*. *Tribology Transactions*, 2003. **46**(3): p. 397-403.
69. Ashoori, D.R., *Photo of Hard-Drive Texturing*, <http://electron.mit.edu>. 2003.
70. Fuller, D.D., *Theory and Practice of Lubrication for Engineers*. 2nd ed. 1984, New York: J. Wiley & Sons.
71. Fowell, M.T., et al., *Entrainment and Inlet Suction: Two Mechanisms of Hydrodynamic Lubrication in Textured Bearings*. *J. of Tribology*, 2007. **129**: p. 336-347.
72. Li, Y., *Modeling of a metal-to-metal face seal*, in *Mechanical Engineering*. 2008, MIT: Cambridge, MA.
73. Elrod, H.G., *A Cavitation Algorithm*. *J. of Lubrication Technology*, 1981. **103**: p. 350-354.
74. Feldman, Y., et al., *The Validity of the Reynolds Equation in Modeling Hydrostatic Effects in Gas Lubricated Textured Parallel Surfaces*. *Journal of Tribology*, 2006. **128**: p. 345-350.
75. de Kraker, A., et al., *A Multiscale Method Modeling Surface Texture Effects*. *J. of Tribology*, 2007. **129**: p. 221-230.
76. Patankar, S.V., *Numerical Heat Transfer and Fluid Flow*. 1980, Washington, D.C.: McGraw-Hill.
77. McClure, F., *Thesis*, in *Mechanical Engineering*. 2007, MIT: Cambridge.
78. Mikic, B., *Analytical Studies of Contact of Nominally Flat Surfaces: Effect of Previous Loading*. *J. of Lubrication Technology*, 1971. October: p. 451-456.
79. Shen, C. and J.M. Floryan, *Low Reynolds number flow over cavities*. *Phys. Fluids*, 1985. **28**(11): p. 3191-3202.
80. Pakdel, P., S.H. Spiegelberg, and G.H. McKinley, *Cavity flows of elastic liquids: Two-dimensional flows*. *Phys. Fluids*, 1997. **9**(11): p. 3123-3140.

81. Hidrovo, C.H. and D.P. Hart, *Emission reabsorption laser induced fluorescence (ERLIF) film thickness measurement*. Measurement Science & Technology, 2001. **12**(4): p. 467-477.
82. Kavehpour, H.P. and G.H. McKinley, *Tribo-rheometry: from gap-dependent rheology to tribology*. Tribology Letters, 2004. **17**(2): p. 327-355.
83. Hupp, S. and D.P. Hart. *Experimental Method for Frictional Characterization of Micro-Textured Surfaces*. in *ASME/STLE International Joint Tribology Conf.* 2004. Long Beach, CA.
84. Wakuda, M., et al., *Effect of surface texturing on friction reduction between ceramic and steel materials under lubricated sliding contact*. Wear, 2003. **254**: p. 356-363.
85. Fletcher, D.I., et al., *Wear behaviour and surface form evolution of a novel titanium carbide implanted surface under lubricated conditions*. Proc. Instn. Mech. Engrs Part J, 2000. **214**: p. 597-610.
86. Wang, X., et al., *The effect of laser texturing of SiC surface on the critical load for the transition of water lubrication mode from hydrodynamic to mixed*. Tribology International, 2001. **34**: p. 703-711.
87. Pearlstein, F., *Electroless Plating*, in *Modern Electroplating*, F.A. Lowenheim, Editor. 1974, Wiley & Sons: New York. p. 710-747.
88. Ronen, A., I. Etsion, and Y. Kligerman, *Friction-reducing surface-texturing in reciprocating automotive components (C)*. Tribology Transactions, 2001. **44**(3): p. 359-366.

APPENDICES

APPENDIX A: EXPERIMENTAL SETUP AND PROCEDURES	161
A.1 Triborheometer	162
A.2 Testing Procedures.....	164
A.2.1 Rheometer Setup.....	165
A.2.2 Flow Parameters.....	165
A.2.3 Run-In Procedure.....	166
A.2.4 Testing Procedure	167
A.3 Data Processing	168
A.4 Verification of Procedure.....	168
APPENDIX B: MANUFACTURE OF TEXTURED SURFACES	171
B.1 Surface Fabrication Techniques	171
B.2 Fabrication Process	174
B.2.1 Aluminum Preparation	174
B.2.2 Electroless Nickel Plating.....	176
B.2.3 Photolithography	178
B.2.4 OmniCoat™ Develop.....	183
B.2.5 Electroless Nickel Plating.....	183
B.2.6 OmniCoat™ Removal	186
B.2.7 Surface Polishing	187
B.3 Electroless Nickel Surface Properties.....	188
APPENDIX C: SURFACE PHOTOGRAPHS AND CHARACTERISTICS.....	191
C.1 50µm 1%	191
C.2 50µm 2.5%	192
C.3 50µm 5%	193
C.4 100µm 5%	194
C.5 100µm 10%	195
C.6 125µm 15%	196
C.7 Control.....	197
APPENDIX D: SECOND ORDER FLUID SOLUTION FOR FILAMENT BREAK- UP	199
REFERENCES	203

APPENDIX A: EXPERIMENTAL SETUP AND PROCEDURES

The Stribeck diagram for a particular lubricant/surface pair must be determined experimentally. This experimental procedure has been performed with a range of devices that include pin-on-disk tribometers, cross-cylinder devices, and atomic force microscopes (AFM). Such devices have a limited range of normal loading and operating conditions, which can limit testing in all of the lubrication regimes of the Stribeck diagram. Instead, the triborheometer described by Kavehpour is used [1] to test the effects that the rheometric properties of lubricants and surface micro texturing have on the friction between sliding surfaces. The triborheometer is reviewed here, and testing procedures used for this study are explained in detail. After explaining the testing details, data verifying the experimental setup and procedures is presented. Further explanation and verification of the testing procedures are given in earlier work by Hupp [2].

A.1 Triborheometer

The triborheometer is adapted from a standard torsional rheometer with a parallel plate geometry. A photo of a rheometer is shown in Figure A.1. A 20mm-diameter stainless steel flat plate is rotated relative to an experimental surface with an interfacial lubricant under a nominal normal force of 15N. The normal force is measured by the Peltier plate and controlled via a feedback loop. The Peltier plate can also control temperature and maintains the surface at a constant value throughout testing. It is not recommended to test for friction directly on the Peltier plate because there is no means of guaranteeing parallelism, and testing in the mixed and boundary lubrication regimes will leave wear scars on the Peltier plate. For tests where the temperature must be carefully controlled, however, this type of testing may be necessary. A labeled schematic of the triborheometer is shown in Figure A.2.

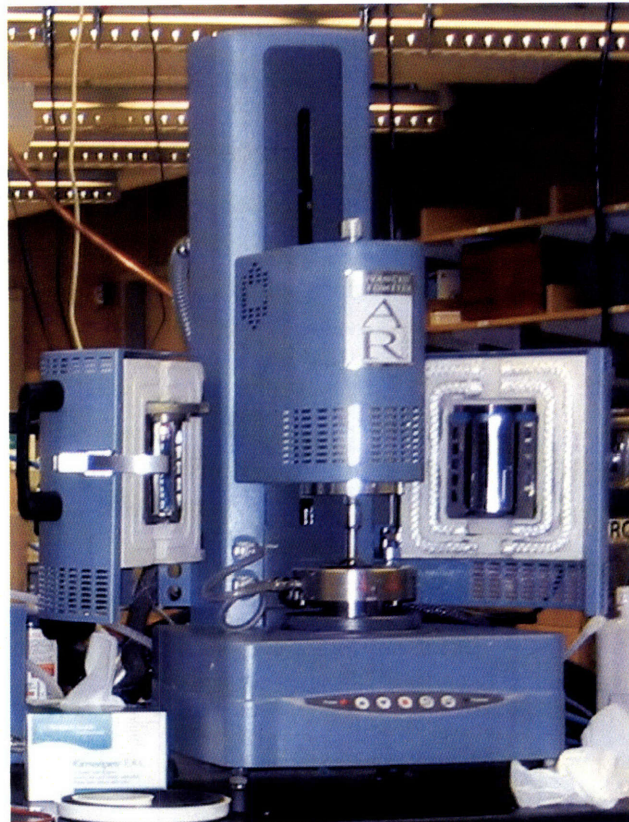


Figure A.1. Photograph of a torsional rheometer. This rheometer is termed a “triborheometer” when it is used with a parallel plate geometry and tested against an experimental surface with an interfacial lubricant under conditions of a constant normal force.

Attaching the lower plate onto the base Peltier plate using a layer of softened wax as described by Kavehpour attains parallelism between the testing surface and the rotating parallel plate. Friction data is extracted from rheometer measurements of the torque required to increase the angular velocity of the rotating upper flat plate over several decades at a constant normal force. The rheometer maintains a constant angular velocity for an integer multiple of a complete revolution of the rheometer head and records an average torque before stepping to the next value of angular velocity. Due to an observed break-in period of the surface, the procedure for testing requires that the same method described for collecting data be performed once before data is collected with the

exception that the angular velocity is decreased in incremental steps until the Stribeck curve flattens to a horizontal line, thus indicating the boundary lubrication regime and full surface-to-surface contact.

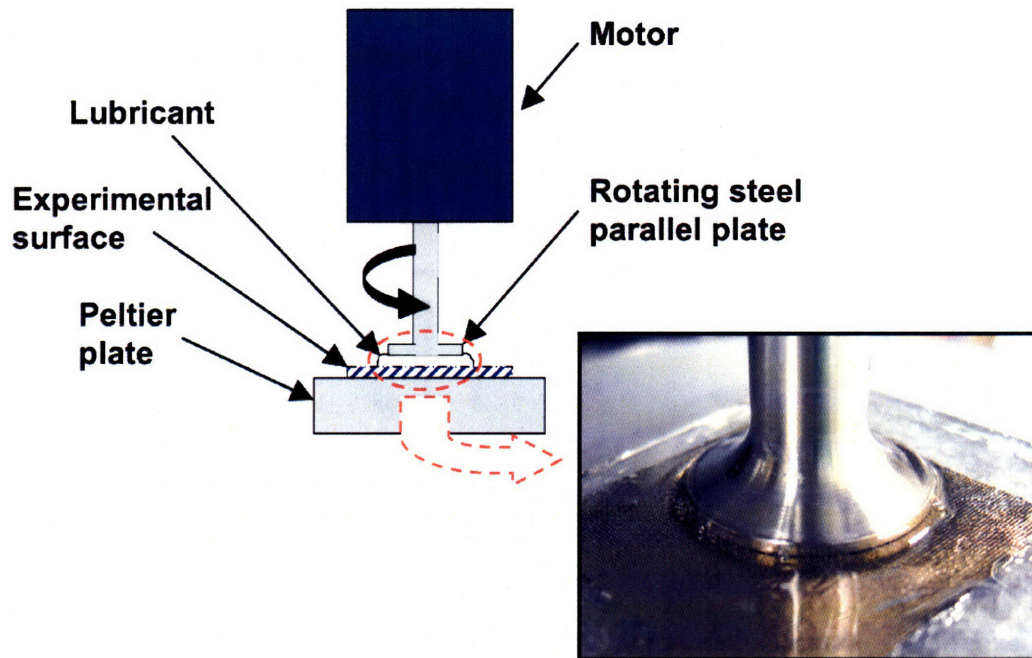


Figure A.2. Schematic of the tribometer device with a 20mm diameter flat, stainless steel parallel plate rotating relative to a textured nickel surface with an interfacial lubricant.

A.2 Testing Procedures

Specific and consistent testing procedures helped to improve the repeatability of the resulting data.

A.2.1 Rheometer Setup

In order to attach the textured surface to the surface of the Peltier plate as shown in Figure A.2 approximately 1 cubic centimeter of paraffin wax is chopped and placed in the center of the Peltier plate. Then the textured surface is set on top of the wax and the rheometer head is lowered until it made contact with the plate. Using the rheometer control interface, a constant 15N normal force is applied to the surface. After setting the normal force, the temperature of the Peltier is raised to the melting point of the wax. The normal force applied to the surface of the plate pushed the surface into a nearly perfect parallel configuration with the rheometer head while securely affixing it to the surface of the Peltier plate. Before the wax melts completely and while the textured surface and Peltier are still approximately 1mm apart, the Peltier is cooled back to 25°C at no more than 5°C per minute while maintaining the 15N normal force.

Once the Peltier reaches 25°C, the rheometer head is lifted off of the surface. The textured surface with the nickel surface is then securely affixed to the Peltier plate and configured to be parallel with the rheometer head.

A.2.2 Flow Parameters

The only parameter that is varied during the friction test is the angular velocity, Ω , of the parallel plate. The lubricant rheology and rheometer geometry determine the range of angular velocities and the constant normal force for each test. The desired result is a complete Stribeck curve, so if a high viscosity lubricant is used, then lower velocities are required, whereas if a lower viscosity

lubricant is selected, then the rheometer needs to run at higher velocities to reach the boundary lubrication regime. The target normal stress for testing is 35kPa, so the applied normal force is adjusted for different rheometer head geometries.

Once the textured plate is affixed to the Peltier plate, the rheometer is configured to perform a flow test procedure at 25°C with a constant normal force. The angular velocity is either set to decrease from between 1 and 100 rad/s to 0.01 rad/s for run-in procedures, or it is set to increase from 0.001 rad/s to 100 rad/s for surface testing. If the torque required to attain the desired rotational velocity exceeds the safe running conditions for the rheometer at high angular velocities, the test will be terminated at speeds less than 100rad/s.

A.2.3 Run-In Procedure

A run-in procedure is performed before running the friction testing procedure if the test is expected to run at conditions where the surfaces will be in contact with one another. This run-in requires the same surface preparation and testing parameters, but the velocity is typically decreased from 100 rad/s to 0.01rad/s at intervals of only 5 points per decade. The rheometer is required to make at least one complete rotation at each velocity point before accepting the average shear stress and moving on to the next data point.

After the run-in procedure is complete, the rheometer head is wiped cleaned using methanol. The nickel, textured surface is simply wiped off, removing as much lubricant as possible without leaving dust or fibers from the

cleaning cloth. Once the surface is cleaned, it is visually examined from dust or unwanted particles and cleaned a second time if necessary. If the experimental surface becomes detached from the Peltier during the cleaning process, the run-in procedure must be repeated. After cleaning, new lubricant is applied and the testing procedure is started.

A.2.4 Testing Procedure

After each surface is run-in, a second velocity sweep is performed. The results from a velocity sweep depended on whether the surface is accelerating or decelerating, as shown in Figure A.3, so for the second run, the velocity is always increased from 0.001rad/s at a sampling frequency of at least 6 points per decade. For velocities ranging from 0.001rad/s to approximately 0.05rad/s, the rheometer is typically only allowed to make a single full rotation before accepting the average shear stress for that velocity and moving on to the next speed. It is important to accept data points only after complete rotations because the shear stress could change in value by as much as 5000 Pa during a single rotation, but the variation is periodic, with a period of a full rotation. Once velocities of greater than 0.05rad/s are reached, a single rotation requires less than 5 minutes to complete, so the rheometer is typically allowed several full rotations before accepting the average shear stress.

A.3 Data Processing

The recorded data is viewed using a Rheology Advantage Data Analysis© software by TA Instruments Ltd. With this software, the pertinent variables are selected for each test and copied into Microsoft Excel© for further analyzing.

In order to determine the friction coefficient and the Gumbel number to make up a Stribeck diagram, the relevant rheometer output parameters are the torque, normal force, velocity, and gap. From these parameters, the normal force N is divided by the surface area of the rheometer head with radius r to calculate the normal stress, $\sigma = N / \pi r^2$. The shear stress τ is calculated from the rheometer torque T acting at the rim radius and distributed over the surface area such that $\tau = 2T / \pi r^3$. Both of these calculated stresses are given as outputs in the TA Data Analysis software, but they can be calculated independently for verification.

A.4 Verification of Procedure

To verify the accuracy and repeatability of the testing setup and procedures, several tests were performed. The first test was to keep a surface on the rheometer and test it several times to determine the effect of testing procedures on surface wear and the subsequent effect on the Stribeck diagram. The Stribeck diagram shown in Figure A.3 illustrates the results of this test. There is a directional effect of testing such that the Stribeck curve changes depending on whether the test was run with increasing or decreasing speeds.

Despite this effect, there was not evidence of surface wear after the initial break-in period, which was considered the first run from fast to slow speeds in Figure A.3.

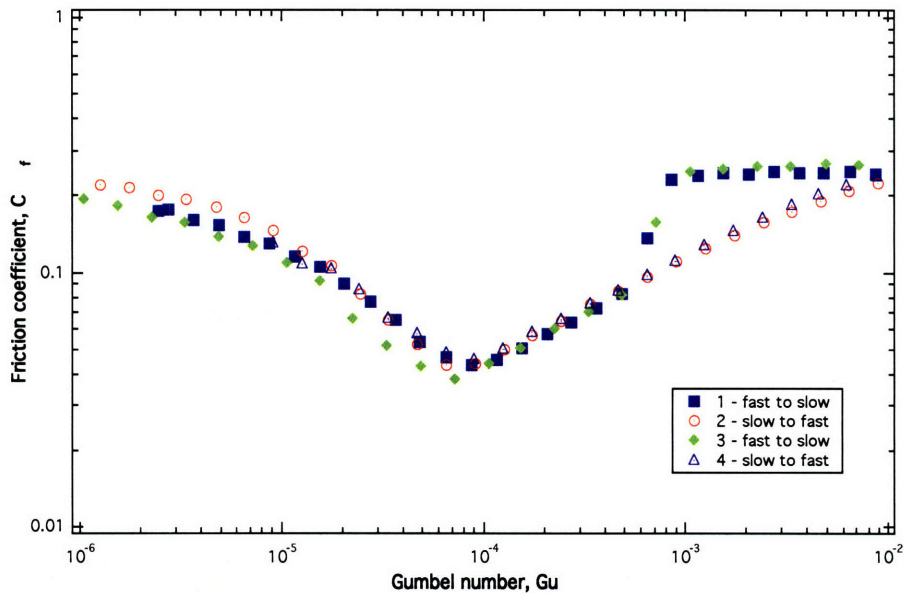


Figure A.3. Verification of testing procedures. There is no evidence of surface wear after the break-in period (run 1), and the data is highly repeatable for tests in which the velocity is varied in the same way.

Figure A.4 illustrates the success of the Stribeck diagram in normalizing the applied normal force. Each data-collection test used a particular lubricant and tested the lubricant/surface interaction by applying a constant normal force and increasing the applied relative rotational velocity between the two surfaces. The effects of changing lubricant viscosity are discussed in Chapters 4 and 5.

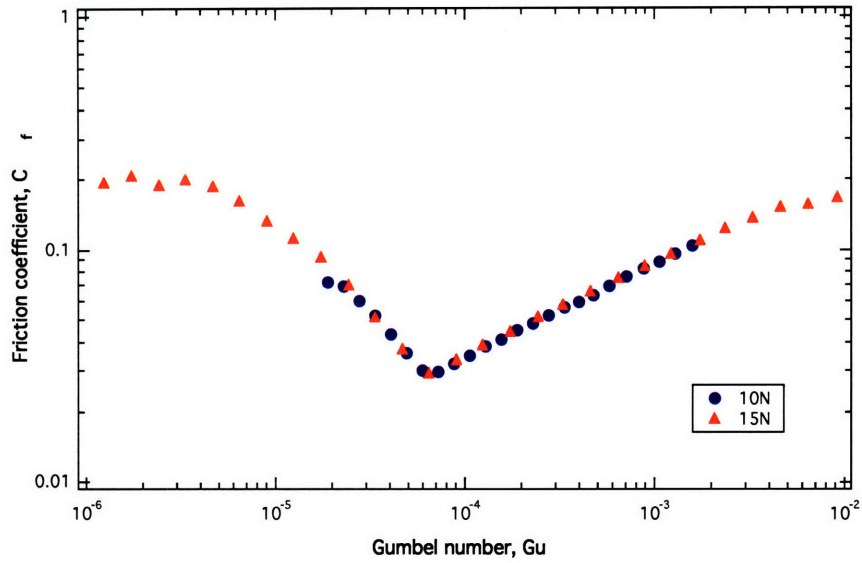


Figure A.4. Verification that the Gumbel number, Gu , successfully normalized the applied normal force. Here, both a 10N and 15N applied normal force are normalized to match the same Stribeck curve.

Further explanation and verification of the testing procedures are given in earlier work by Hupp [2, 3]. The testing procedures described in this appendix were used exclusively for collecting data for this thesis research, unless other procedures are specified.

APPENDIX B: MANUFACTURE OF TEXTURED SURFACES

There are several documented methods of fabricating surfaces with a micro-scale applied texture, including chemical etching, machining, and laser surface texturing [4-8]. After reviewing these methods and considering the desired surface material characteristics for this study, an additive method of combined photolithography and electroless deposition was determined to be most appropriate.

B.1 Surface Fabrication Techniques

Several surface fabrication techniques have been explored in published literature. Chemical etching is a process where a pattern is placed on a flat surface, and an etching chemical is allowed to dissolve the remaining exposed surface for a pre-specified period of time or until a desired depth had been reached [9]. When the etchant creates a hole, both the bottom of the hole and the sides of the hole are exposed, so the sides begin to dissolve along with the layer of material on the bottom. As the hole reaches the required depth, the diameter has increased and the sides of the hole may no longer be vertical. Instead of etching, surface machining is a more controlled micro fabrication

method. Surface machining is limited by the size and shape of the texture patterns. Longitudinal patterns have successfully been machined on titanium surfaces using a shaper [4], but micro-scale holes have not been documented for tribological experimentation. Future progress of small-scale machining techniques may create opportunities to fabricate micro textured surfaces using this technique.

Laser ablation has been demonstrated to successfully micro texture many different surface materials with precise geometries [10], and this texturing can be applied to component surfaces of different shapes and sizes. In addition, it gives uniform results and has large-scale manufacturing potential. Depending on the material used, however the laser can crack the surface [11] or it can melt some of the material and re-deposit it around the hole so that polishing is necessary to eliminate burrs on the surface. Another concern with laser ablation techniques is that the melting and subsequent re-solidification of the material due to the laser may work-harden the material around the hole so that the surface properties are not uniform.

The desired surface material for this research was a common engineering material that was easy to fabricate. Metals that are wear and corrosion resistant fit this category along with ceramics. Of the previously discussed manufacturing techniques, etching does not provide uniform, repeatable results and was therefore not desirable for an experimental investigation. Previous literature recommended that optimal surface texturing required texture geometries that were unreachable with current machining techniques [6, 7] and surface laser

texturing was not readily available. Therefore, a new micro texturing technique was developed. This techniques has been previously described by Hupp [2, 3], but will be repeated here for clarity and completeness.

The new micro texturing technique used to fabricate surfaces for this work was an additive process that required photolithography techniques to apply a texture pattern, electroless nickel plating to build the surface, and removal of the photoresist so that the remaining surface consisted only of the base substrate covered in electroless nickel. Figure B.1 illustrates the layering process that will be described in detail.

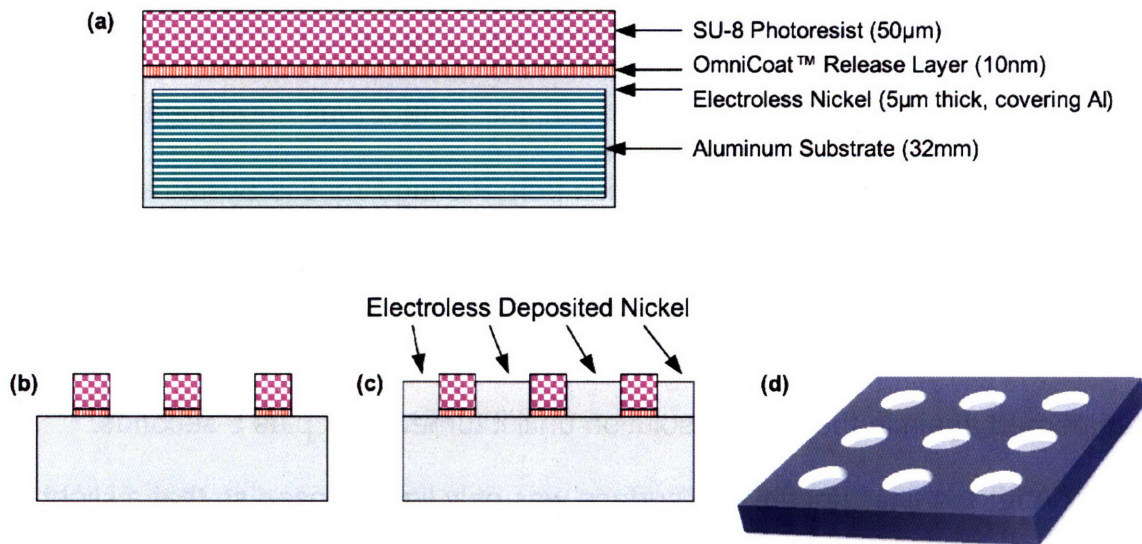


Figure B.1. Illustration showing the layering required for the manufacture of nickel micro textured surfaces. a) An aluminum disk is zincated and coated with electroless nickel, and then photoresist is applied on top of a release layer. b) the photoresist and release layer are developed to leave a pattern, and c) electroless nickel is deposited in the negative space of the photoresist pattern. d) After depositing the nickel, the photoresist is removed, which leaves only the nickel texture on the surface.

B.2 Fabrication Process

B.2.1 Aluminum Preparation

The autocatalytic process for electroless nickel plating will not occur on an aluminum surface, so the first step in the fabrication process was to produce a zinc immersion coating on the aluminum substrate and plate a seed layer of electroless nickel. The zinc coating is produced using a commercial zincate solution from Plating Process Systems, Inc.

First, the aluminum was washed to remove all dirt and impurities, and then it was zincated. The zincate process is given in Table B.1. First the substrate was rinsed with deionized water, and then it was soaked in a 40%vol solution of nitric acid for 1 minute. After the acid soak, the surface was rinsed again and immersed in ZinAl™, the zincate solution from Plating Process Systems, Inc. until the surface turned dark plus an extra 5 seconds. The surface was again rinsed and put in the acid bath, and after 30 seconds the surface was rinsed and submerged again in the zincate solution until it turned dark plus 5 seconds.

After the final zincate, the surface was only lightly rinsed so that a slight alkaline film remained- this film acts as a catalyst for the nickel plating process. A nickel strike was then performed, where the surface was submerged in an electroless nickel plating bath held between 88 and 92°C. After 10 minutes in the nickel strike, the surface was moved to a new electroless nickel solution maintained between 88 and 92°C, where it was left for 1 hour to plate a 5 micrometer thick coating onto the aluminum.

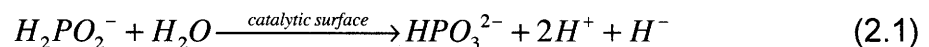
Table B.1. Zincate process to prepare aluminum substrate for electroless nickel plating. Instructions provided by Plating Process Systems, Inc.

Prepare surface	Wash aluminum surface thoroughly
Rinse	Rinse surface with cold, deionized water
Acid	Immerse surface in 40% nitric acid bath at room temperature for 1 minute
Rinse	Rinse surface with cold, deionized water
Zincate	Immerse surface in zincate solution at room temperature until 5 seconds after the surface turns dark or for a maximum of 30 seconds.
Rinse	Rinse surface with cold, deionized water
Acid	Immerse surface in 40% nitric acid bath at room temperature for 30 seconds
Rinse	Rinse surface with cold, deionized water
Zincate	Immerse surface in zincate solution at room temperature until 5 seconds after the surface turns dark or for a maximum of 30 seconds.
Rinse	Quickly rinse surface with cold, deionized water
Electroless Nickel Strike	Immerse surface in electroless nickel plating solution at 88 to 92°C for 10 minutes.
Electroless Nickel Plate	Move surface to a new electroless nickel bath and continue to plate at temperatures between 88 and 92°C for 1 hour.

B.2.2 Electroless Nickel Plating

Electroless plating is a “controlled autocatalytic chemical reduction process for depositing metals” [12]. Once the deposition is initiated on a catalytic surface, plating continues at a rate linear with time. For nickel hypophosphate baths, such as the one used for this study, the essential chemicals for the reaction are a nickel salt, hypophosphite, and a salt, which acts both as a buffer and a mild complexing agent for nickel. Other substances can be added to improve bath stability or increase plating rates. Plating can only be initiated on catalytic metals such as nickel, cobalt, steel, and other active metals. Non-catalytic metals and non-metals can also be plated, but appropriate conditioning steps such as the zincate process for aluminum that was described in Section B.2.1 must first be performed. Once the plating process is initiated on any surface, deposition continues because electroless nickel is itself catalytic. A description of the chemical reactions that take place during the plating process are given by Pearlstein [12] and summarized here.

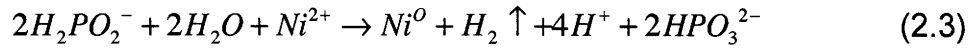
The first step in the deposition process is catalytic dehydration of hypophosphate with a hydride transfer to the catalytic surface [12]:



The hydride ions can then react with nickel ions to produce the deposit:



The total reaction can be represented by



Electroless nickel plating produces a nickel-phosphorus alloy rather than a pure nickel coating. Typical deposits contain 3 to 15% (wt) phosphorus.

For this study, a commercial electroless nickel bath was chosen in order to attain consistent results. The plating bath resulted in a high phosphorous, corrosion resistant surface and was developed and sold by Plating Process Systems as their CR bath.

Bath Preparation

In order to use the electroless nickel bath, two solutions, CR-M and CR-N, were carefully mixed together and heated according to the directions given by Plating Process Systems, Inc. The pH was maintained around 4.8 using dilute ammonia hydroxide, and the temperature range for plating was between 88–92 °C. The bath did not plate at lower temperatures, and it could decompose at higher temperatures. Once the bath was prepared and stabilized at the desired temperature, it was ready for plating.

B.2.3 Photolithography

After depositing the nickel seed layer onto the aluminum substrate, the next step of the fabrication process was to create a photoresist pattern on top of the nickel seed layer. Patterns were designed to test the effect of pattern density and size and included the recommended optimum sizes and densities from previous research [6, 11, 13-15]. There is a minimum size limitation for photolithography texturing because a transparency mask of the pattern must first be available. Available printers were limited to a maximum resolution of 5080 dots per inch; therefore the pattern is comprised of dots that are approximately $5\mu\text{m}$ in diameter. Square patterns thus had a minimum corner radius of $2.5\mu\text{m}$, but the dot pattern led to discontinuous lines for features smaller than approximately $50\mu\text{m}$ in diameter.

Another limitation to photolithography is the aspect ratio of the features. Applications that require the photoresist to be eventually removed from the surface typically use positive photoresists, which will easily dissolve in solvents such as acetone or methanol. Positive resists, however, can only be spun in thicknesses less than $20\mu\text{m}$, and the goal for this research is to attain surface features that are around $20\mu\text{m}$ deep. The best option for taller features is to use SU-8, a negative photoresist. SU-8 is not easily removed with solvents, but using OmniCoat™ from MicroChem corporation as a base/release layer, the photoresist can be lifted off using RemoverPG™, another MicroChem product. SU-8 is a very viscous photoresist and can be spun into thicknesses greater than $100\mu\text{m}$.

OmniCoat™ Release Layer Application

Before applying the photoresist and release layer to the surface of the nickel-coated glass samples, they were first dehydrated in a convection oven at 180°C for 20 minutes. After dehydration, the OmniCoat™ release layer was spun onto the sample and baked for 1 min. on a 200°C hotplate according to the instructions given by MicroChem and shown in Table B.2.

After baking the OmniCoat™, the surfaces were allowed to cool before starting the SU-8 process.

Table B.2. Details for applying the OmniCoat™ release layer.

Thickness	20nm
Dispense	2mL
Spin	500 rpm for 5sec with acceleration of 100 R/s 3000 rpm for 30 sec with acceleration of 300 R/s
Bake	200 °C hotplate for 1 min

SU-8 Photoresist Application

The SU-8 photoresist application process is summarized in Table B.3 and described below in detail. Because the substrate was a 3/8-inch thick aluminum plate rather than a silicon wafer, the bake times for the SU-8 were altered from the MicroChem instructions to allow for the difference in thermal properties between the two substrates. Overall the bake times increased slightly, but the thick aluminum allowed for very uniform heating of the photoresist layer.

Spin

The first step in processing the photoresist was to spin coat the surface. To do this, approximately 4mL of SU-8 was dynamically dispensed onto the surface, creating as few air bubbles as possible. Once on the surface, the photoresist was allowed to spread until almost reaching the sides, at which point the surface was spun at 500 rpm to allow the resist to completely cover the surface. Once covered, the surface was moved to hotplates for the pre-bake and softbake steps.

Softbake

After completing the softbake, the surfaces were required to cool to room temperature before UV exposure. Depending on the room temperature and humidity, the bake times may need slight adjustment. If the photoresist surface is still tacky after cooling from the softbake, it should be baked again at 95 °C at

approximately 1-minute intervals until the surface is no longer tacky at room temperature.

Expose

While the surface was cooling after the softbake, a transparency mask was selected to create the desired texture pattern. This pattern should be the negative image of the desired texture since the photoresist will ultimately be removed to leave only a nickel pattern. The pattern should be free of dust and creases in order to get a more consistent pattern. When the surface was cool, it was placed on the aligner with the mask on top covered by a glass slide to hold the mask in place, and then it was exposed to near UV light (350–400nm) at 400 mJ/cm².

Post Expose Bake

Following exposure, the surface was baked at 65 °C for 1 minute and then moved to 95 °C for 6 minutes. This final bake cross-linked the exposed photoresist film.

Develop and Rinse

The photoresist was developed using a spin process. While the surface was spun at 100 rpm on a coater, it was sprayed with propylene glycol monomethylether acetate (PGMEA) in 5 second intervals for 2 minutes. After developing, the PGMEA was rinsed with isopropyl alcohol and allowed to spin

dry. A visual inspection was done under a microscope to check if the SU-8 has been fully developed. It is essential that the developing is complete and that there is no residue left in corners or at the base of the resist posts since photoresist is not a catalytic surface for electroless nickel.

If the resist is not completely developed, repeat the spin develop step for 30 second to 1-minute intervals and repeat the rinse step.

Table B.3. Photolithography process for SU-8 100 on borosilicate glass substrate

Thickness	50 μ m
Dispense	3mL
Spin	500 rpm for 5sec with acceleration of 100 rpm/s 1500 rpm for 30 sec with acceleration of 300 rpm/s
Pre-bake	65 °C hotplate for 7 min
Soft bake	95 °C hotplate for 24 min
Expose	350-400nm at either 400 mJ/cm ²
Post exposure bake 1	65 °C hotplate for 1 min
Post exposure bake 2	95 °C hotplate for 6 min
Develop	Spin develop using PGMEA for 2 min
Rinse	Briefly rinse with isopropyl alcohol

B.2.4 OmniCoat™ Develop

The final step in completing the photoresist mask was to develop the OmniCoat™, which was done by O₂ plasma removal. The surface was placed under a 200 mTorr vacuum while the power was maintained at 75W for 3 minutes in order to completely remove the exposed OmniCoat™ from the surface of the vapor-deposited nickel. After removing the OmniCoat™, only the nickel surface not covered by the photoresist pattern was exposed for subsequent plating by the nickel electroless plating process.

B.2.5 Electroless Nickel Plating

A surface that had previously undergone patterning with photoresist and ashing was lowered into a plating bath prepared according to Section B.2.2. The surface was secured so that it remained fully submerged. The bath was stirred gently using a magnetic stirring rod, and in order to obtain the most uniform pattern, the orientation of the surface was changed every 15 to 30 minutes; a simple 90° rotation worked well. Figure B.2 shows a photograph of a surface that was not rotated in the bath, and Figure B.3 shows the result of a surface with an identical pattern, but it was rotated every 15 minutes for the first 2 hours and every 30 minutes for the last hour. As bubbles collected around a photoresist post, they rise to the top of the post but remained there until enough gas was collected to gain the buoyant force required to dislodge it from the surface. For

this reason, surfaces that were not rotated often were formed with a low region at the top of the post where less plating had built-up due to air bubble accumulation.

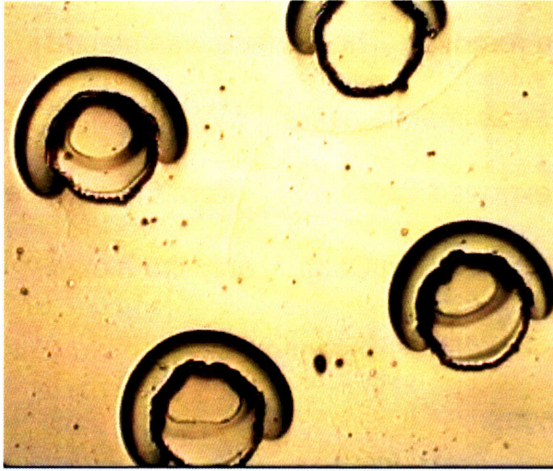


Figure B.2. 100 μ m10% surface shows a non-uniform pattern due to bubble accumulation during the nickel plating.

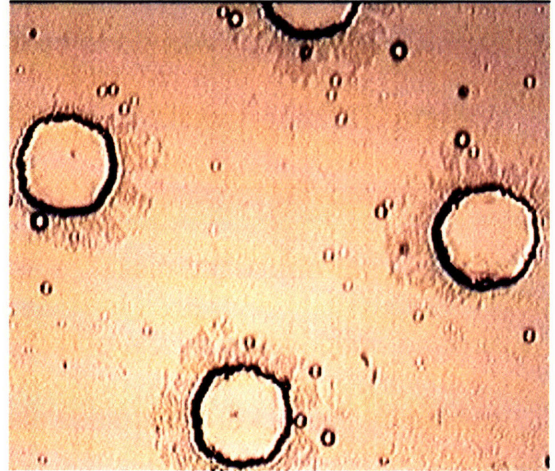


Figure B.3. B100 μ m10% surface was rotated frequently during plating, so the holes are more uniform.

Plating time depended on bath pH, nickel activity, and bath temperature. If the bath remained around 90°C, a nickel layer of approximately 15µm was deposited after 3 hours of plating. To determine the exact layer thickness, the surface thickness was carefully measured before plating and compared to measurements during plating. To measure the thickness of the surface during plating, it was removed from the bath and rinsed with deionized water. After measuring, the surface is rinsed again with DI water before being returned it to the bath in order to reduce the impurities on the surface and in the bath. During the plating process, the bath was monitored for impurities and loose nickel pieces. If the bath became contaminated with visible impurities, the surfaces was removed and rinsed with DI water. The bath was filtered through a 5 to 20µm membrane filter, and then it was reheated to plating temperature before the surface was re-submerged and plating was resumed.

Once the desire thickness was reached, the surface was removed from the plating bath and rinsed a final time with deionized water. The electroless plating bath was no longer needed and was disposed of according to appropriate chemical safety procedures.

B.2.6 OmniCoat™ Removal

Once the nickel plating process was complete, the final step in the surface manufacturing procedure was to remove the OmniCoat™ release layer. First, 100mL of RemoverPG™ was heated to 80 °C. After the solution was stabilized at the desired temperature, the textured surface was completely immersed in the solution and agitated for 30 minutes. The surface was removed from the solution after 30 minutes, rinsed with distilled or DI water and dried using forced air. If some of the photoresist posts remained on the surface, they were blown off using the canned air. Typically, the photoresist was visible without the aid of a microscope by looking at the plate profile instead of looking directly from the top. Figure B.4 shows a surface with the photoresist posts before it was submerged in the plating solution. The posts can be seen without the aid of magnification, although it is not necessarily possible to identify the post shape or size. A microscope may be necessary in some cases. If the posts were still in place, the RemoverPG™ bath was repeated until all posts were removed from the surface. The surface was dried completely and stored in a dry place with care taken not to scratch the surface.

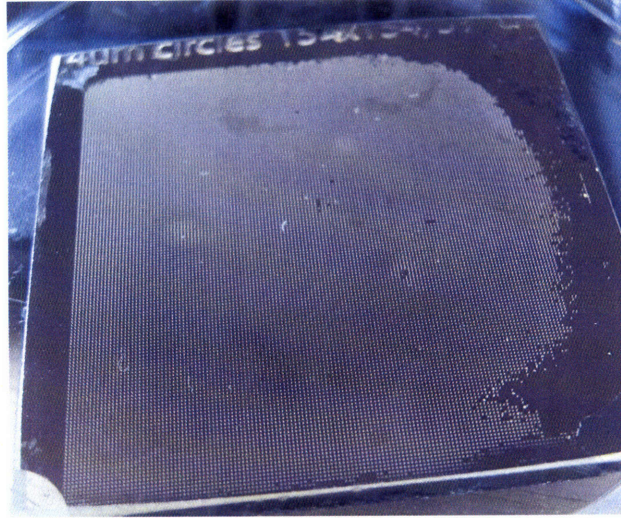


Figure B.4. Photograph of a surface with photoresist posts before the nickel plating process. The posts can be seen without the aid of magnification as tiny opaque pieces.

B.2.7 Surface Polishing

After the electroless nickel deposition, it is possible to have surface burrs as a result of impurities in the electroless nickel bath because the bath is not continuously filtered during the deposition process. These burrs result in surface inconsistencies that affect the surface friction profile, so they are eliminated using a lapping process. The surface is lapped at a speed of about 1 rotation per second for 5 minutes on 5 μ m silicon carbide lapping film, and then it is lapped another 3 minutes on 1 μ m aluminum oxide film. The surface is ultra-sonically cleaned after lapping to remove particles from inside the micro cavities. The final surface preparation step is a deionized water rinse and drying with forced air.

Electroless nickel is very sensitive to heat treatments, so if a harder surfaces is desired, then it is possible to heat treat the surfaces using a hotplate

or oven. This step was not performed for the current research project in order to limit variations in the surface properties between each textured surface.

B.3 Electroless Nickel Surface Properties

Since electroless nickel plating is an autocatalytic process, the chemistry involved requires that the resulting surface actually be a nickel-phosphorus alloy. This alloy is advantageous in friction testing because electroless nickel-phosphorous coatings are considerably harder and more wear resistant than conventional electroplated nickel [12]. According to literature from Plating Process Systems Inc., the particular process used for this research resulted in a surface that was approximately 89% nickel and 11% phosphorus. The material properties of the surface are given in Table B.4.

Table B.4. Typical deposit properties of CR-MRN electroless nickel plating as reported by Plating Process Systems, Inc.

Phosphorous	10.5 – 12%
Hardness (VHN ₁₀₀) as plated	450 – 550
Density	8.2 g/cc
Internal Stress	0 to -15 kpsi
Tensile Strength	>100 kpsi

In addition to knowing the material properties, the final size of the surface texture and the surface roughness must be measured using a Zygo laser

profilometer. A NewView 5000 model was used in this study; Figure B.5 is a sample scan of a surface that has 100 μm diameter holes with a cavity depth of 16 μm , as shown in the surface profile. The vertical resolution of the scan is reported by Zygo to be 0.1nm with a standard maximum vertical step height of 100 μm . With the 20x Mirau interferometric objective, the lateral resolution of the scan is 0.88 μm with a maximum change of angle between pixels of 14.56 degrees. The unresolved black area around the surface cavity in Figure B.5 is a result of this slope limitation. Due to the high reflectivity of the nickel surfaces, Zygo scans were performed at a low light level in order to reduced reflected light.

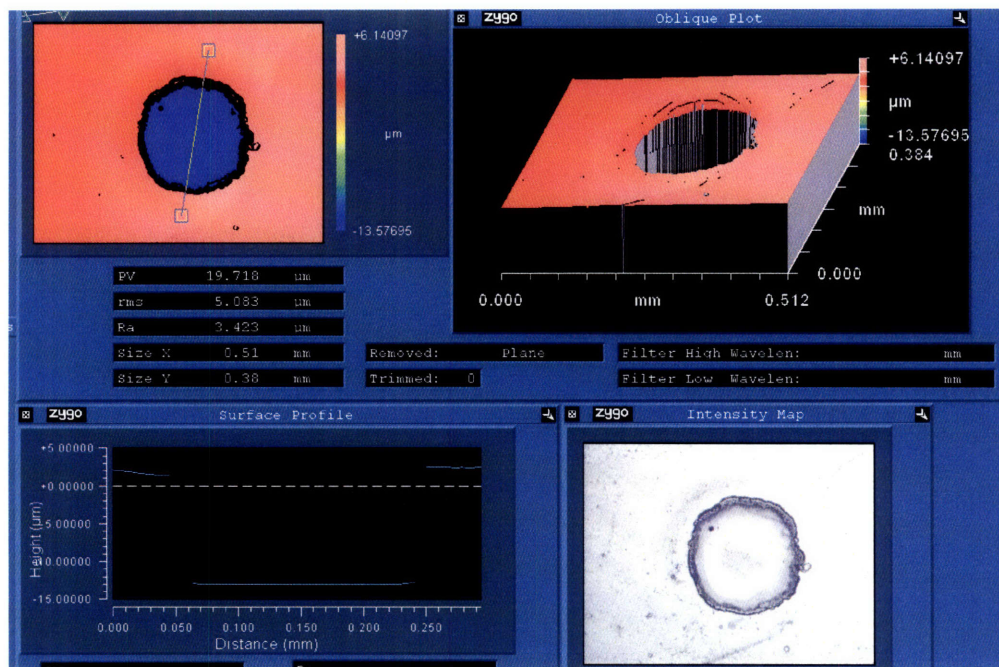


Figure B.5. Profilometer scan from a Zygo laser profilometer. This scan shows that the hole diameter is 100 μm , and the depth is 16 μm .

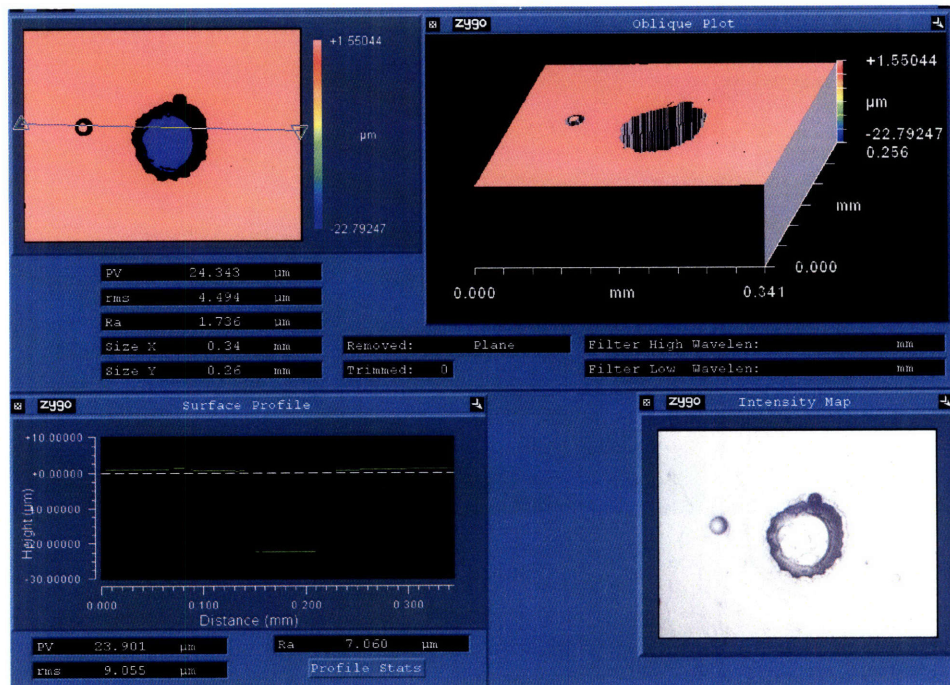
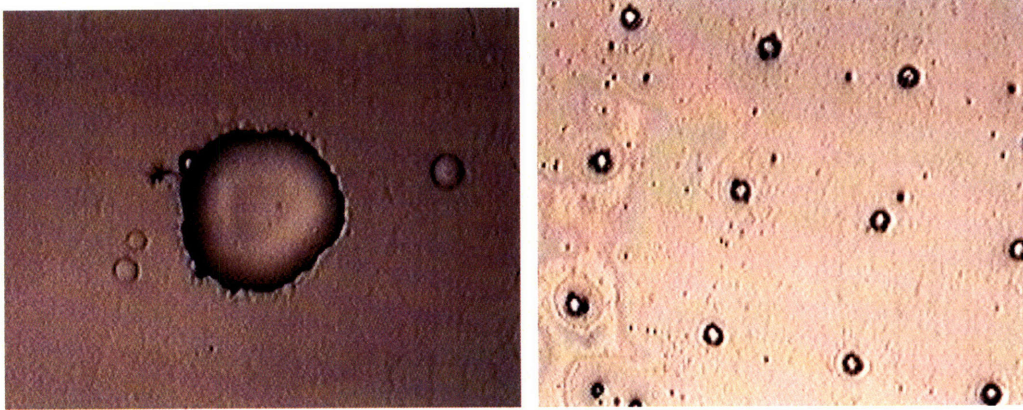
In addition to the hole geometry and surface roughness, the surface waviness is also a property of interest. The waviness is measured with a Dektak³ surface

profilometer. A summary of the surfaces fabricated for this study along with the corresponding texture diameter, depth, and surface roughness for each surface is reported in Appendix C.

APPENDIX C: SURFACE PHOTOGRAPHS AND CHARACTERISTICS

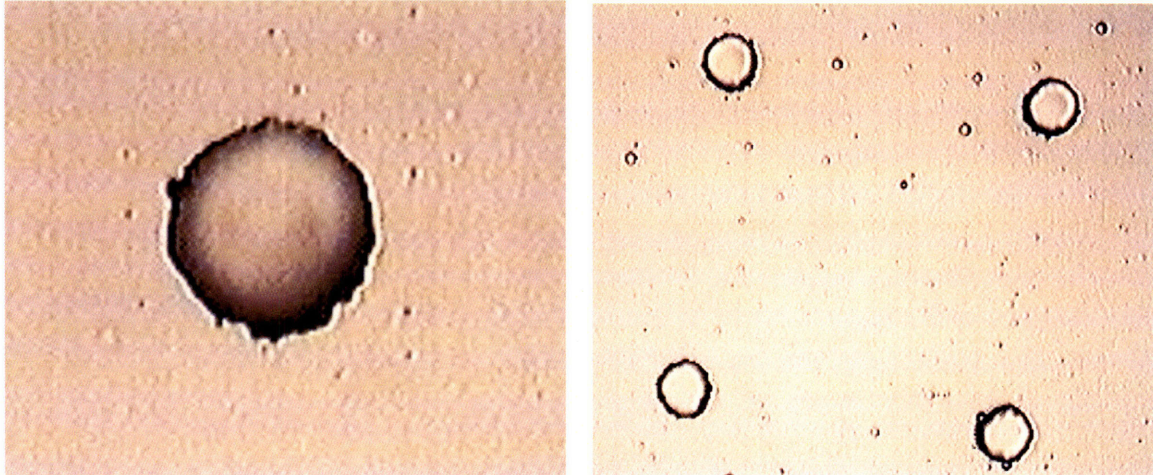
C.1 50 μ m 1%

Surface Roughness (RMS) = 0.01 μ m
Cavity Depth = 24 μ m



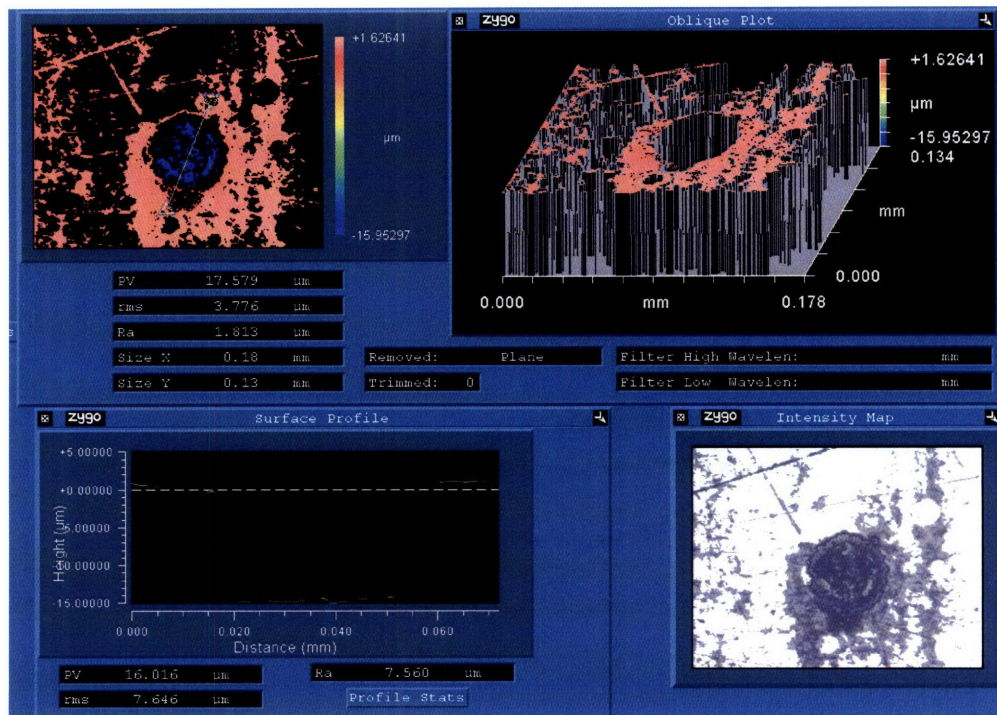
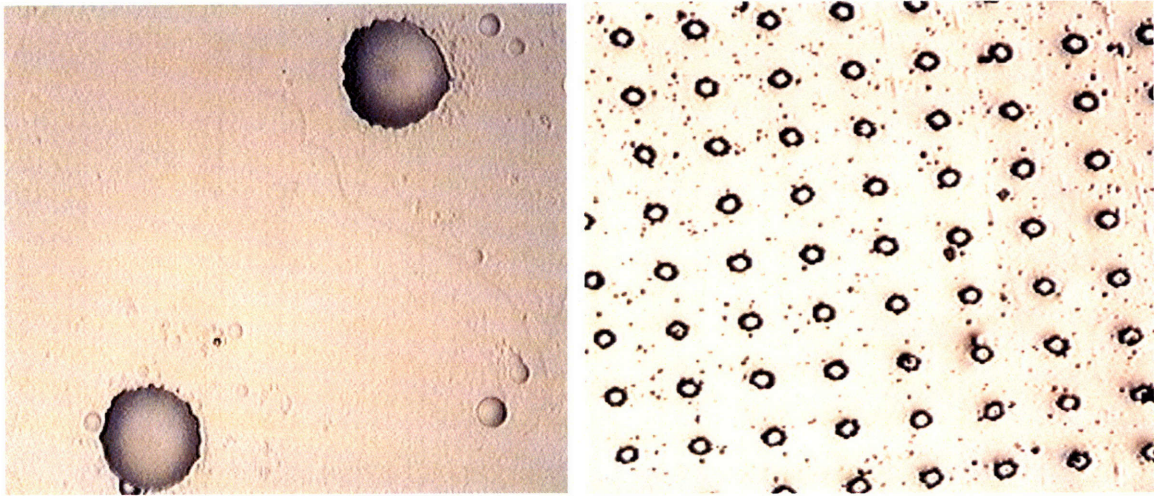
C.2 50 μ m 2.5%

Surface Roughness (RMS) = 0.02 μ m
Cavity Depth = 18 μ m



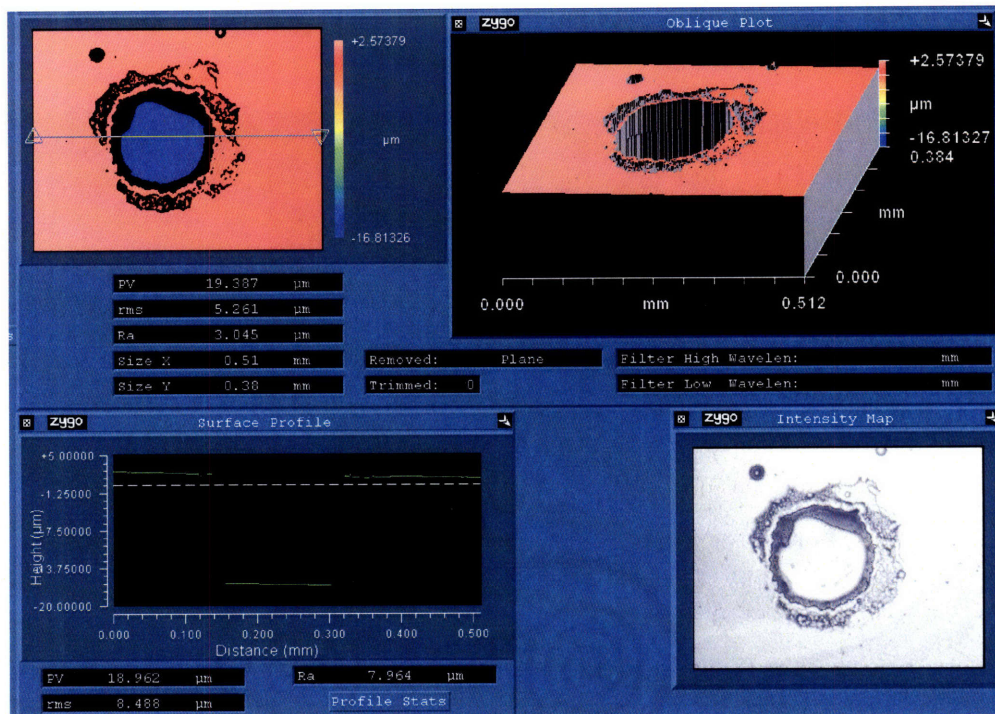
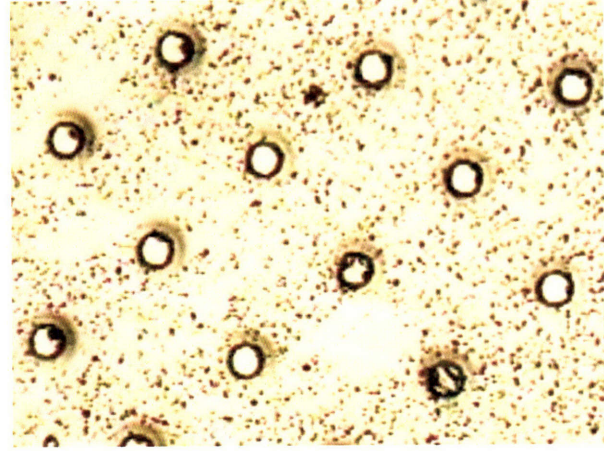
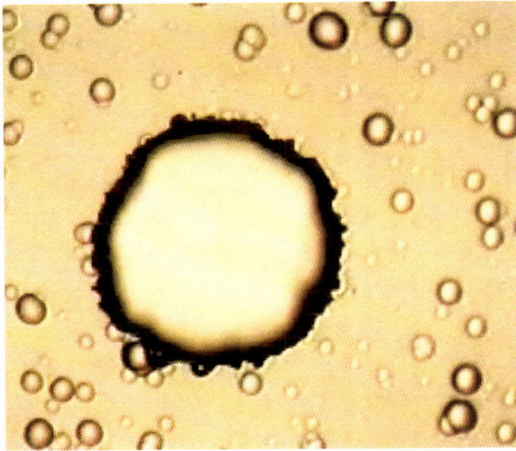
C.3 50µm 5%

Surface Roughness (RMS) = 0.07 µm
Cavity Depth = 16 µm



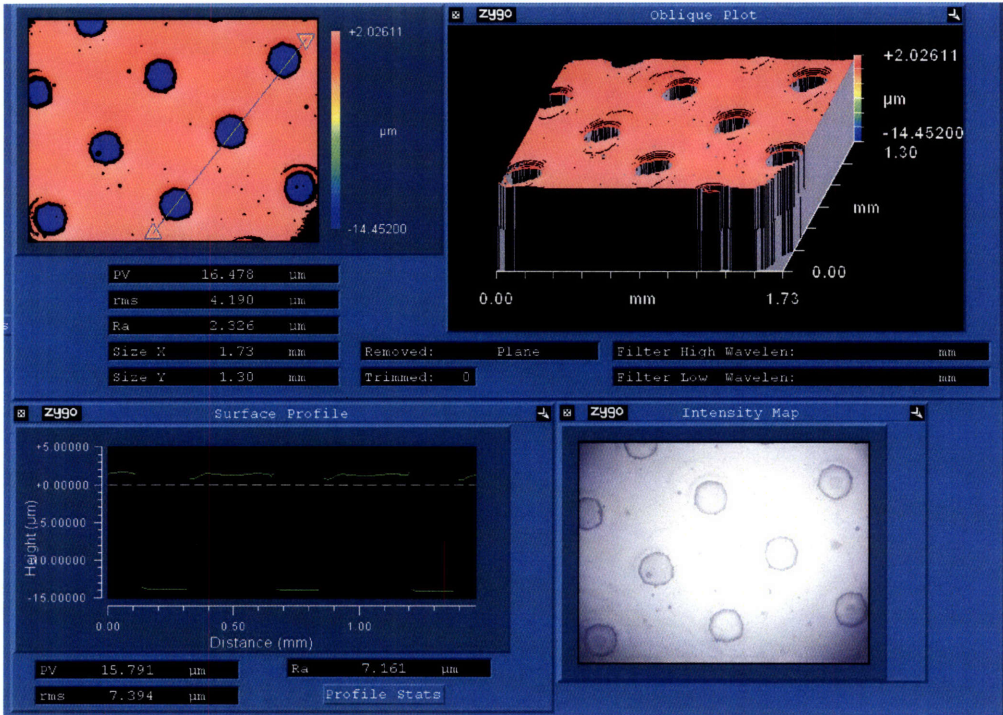
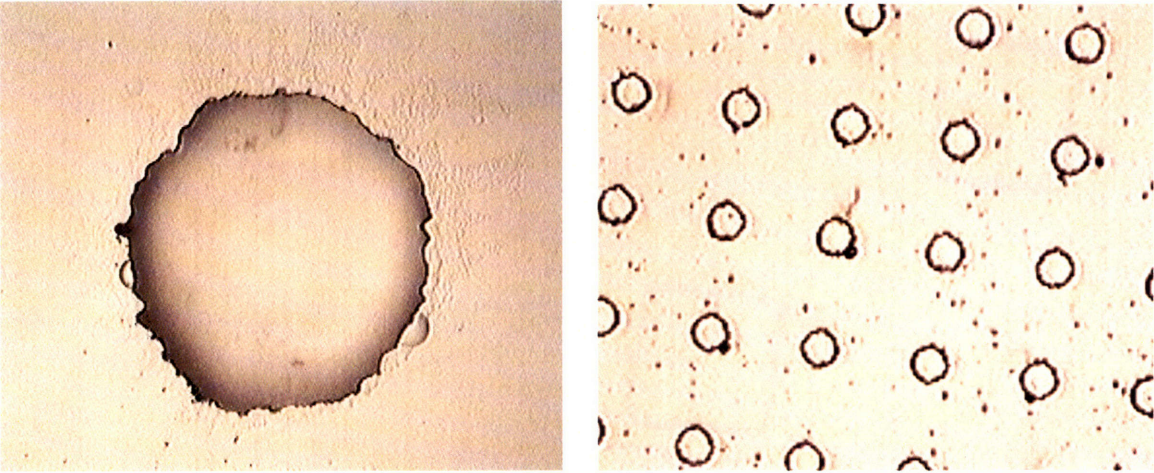
C.4 100 μ m 5%

Surface Roughness (RMS) = 0.03 μ m
Cavity Depth = 19 μ m



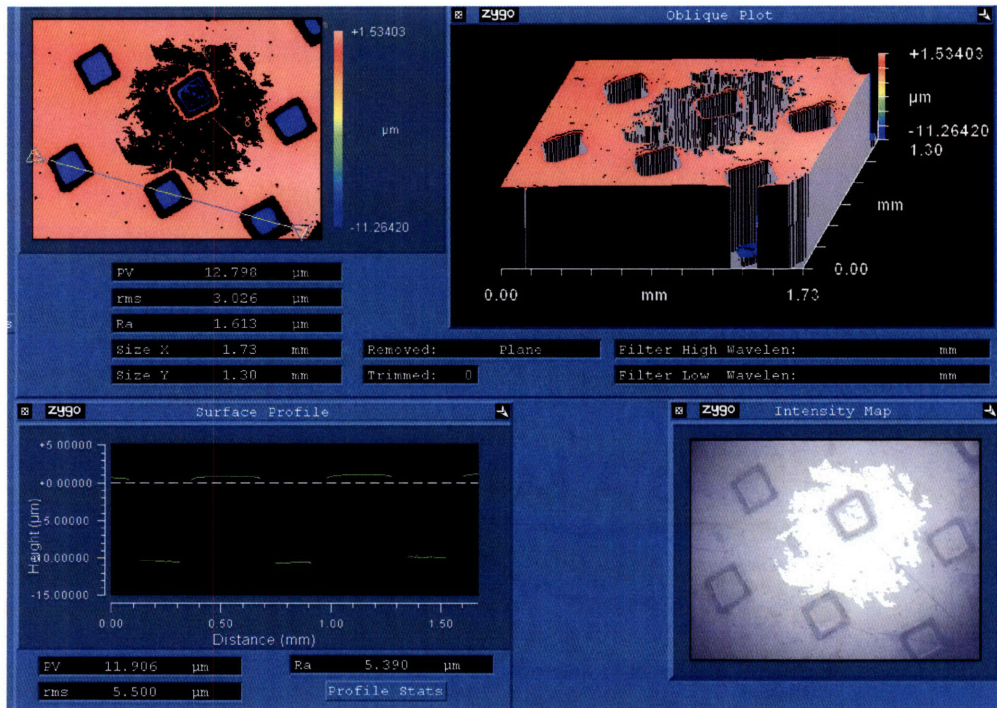
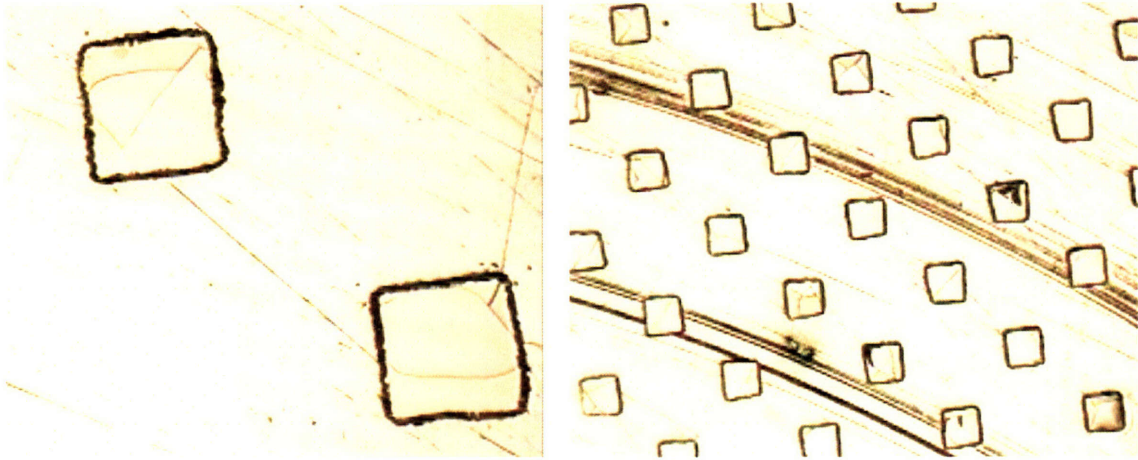
C.5 100µm 10%

Surface Roughness (RMS) = 0.06 µm
Cavity Depth = 16 µm



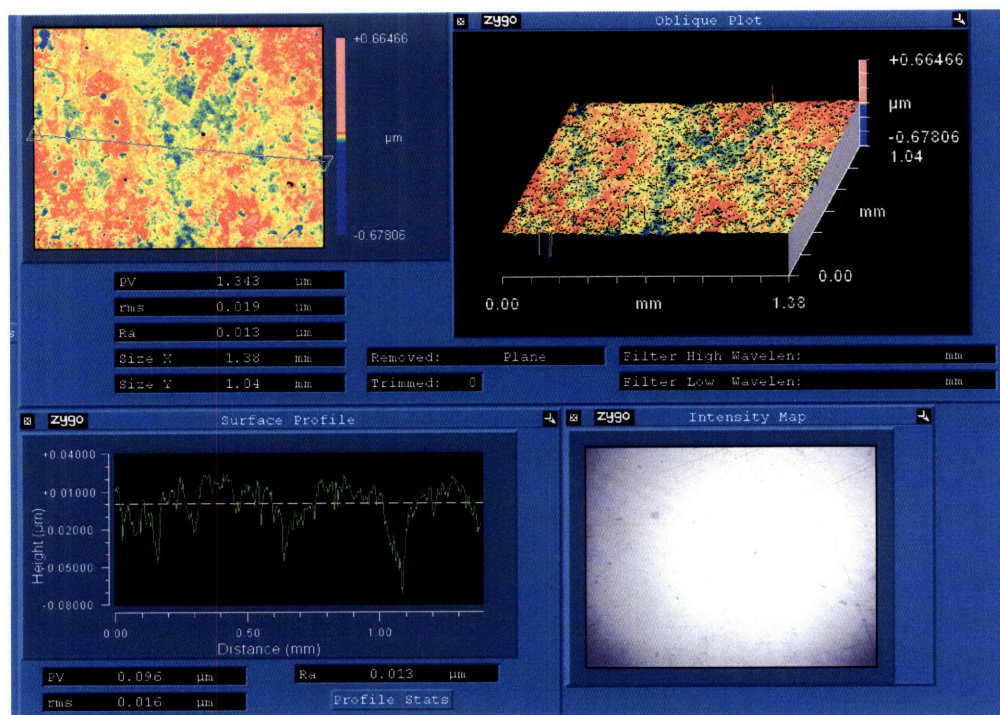
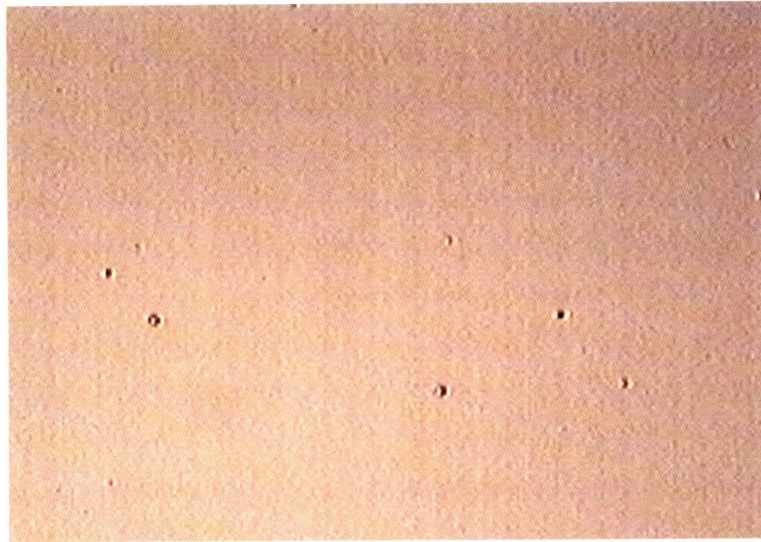
C.6 125 μ m 15%

Surface Roughness (RMS) = 0.03 μ m
Cavity Depth = 12 μ m



C.7 Control – Flat Surface

Surface Roughness (RMS) = $0.02 \mu\text{m}$



APPENDIX D: SECOND ORDER FLUID SOLUTION FOR FILAMENT BREAK-UP

* Notes from Gareth McKinley, Professor in Mechanical Engineering at MIT

$$3\eta_E \dot{\epsilon} = (3\eta_0 + 3b_E \dot{\epsilon}) = \frac{(2x-1)\sigma}{R}$$

Scale with $h = R/R_0$, $t = \hat{t}/t_{\text{char}} = \hat{t}\sigma/6\eta_0 R_0$

$$\left\{ 1 + \left(\frac{b_E \sigma}{3\eta_0^2 R_0} \right) \left(\frac{-1}{h} \frac{dh}{dt} \right) \right\} \left(\frac{-1}{h} \frac{dh}{dt} \right) = \frac{(2x-1)}{h}$$

$$\text{where } B = \frac{b_E \sigma}{3\eta_0^2 R_0} = \frac{b_E}{\eta_0} \frac{\sigma}{3\eta_0 R_0} = \frac{\lambda \sigma}{3\eta_0 R_0}$$

For the Newtonian Solution:

B=0

$$\frac{dh}{dt} = -(2x-1)$$

$$h = 1 - (2x-1)t$$

$$R = R_0 - \frac{(2x-1)\sigma}{6\eta_0} \hat{t}$$

$$t_c = \frac{6\eta_0 R_0}{(2x-1)\sigma}$$

For the Second Order Fluid Solution:

Solve: $B(-\dot{h})^2 - h\dot{h} - (2x-1)h = 0$

$$\text{Solution: } \frac{1}{2}(e^{2y} - 1) + y = \frac{(t_c - t)}{2B}$$

$$\text{Where } y = \sinh^{-1} \left(\frac{h}{4B(2x-1)} \right)^{1/2}$$

Close to breakup for $y \ll 1$:

$$y \approx \frac{(t_c - t)}{4B}$$

$$\sinh y \approx y \approx \left(\frac{h}{4B(2x-1)} \right)^{1/2}$$

or $h \approx \frac{(2x-1)}{4B} (t_c - t)^2$

Rescaling

$$h = R/R_0, \quad t = \frac{\hat{t} \sigma}{6\eta_0 R_0}$$

or $\frac{R}{R_0} \approx \frac{(2x-1)3\eta_0^2 R_0}{4b_E \sigma} \cdot \frac{(\hat{t}_c - \hat{t})^2 \sigma^2}{36\eta_0^2 R_0^2}$

$$R \approx \frac{(2x-1)}{48\sigma} \cdot \frac{\sigma}{b_E} (\hat{t}_c - \hat{t})^2$$

Summary of Fitting Protocol/Equations

1) External Length Scale

- Original equations contain an (arbitrary) external scale, R_0
- This cancels out when substituting for $h = R/R_0$

$$t = \frac{\hat{t}\sigma}{6\eta_0 R_0}$$

$$B = \frac{\lambda\sigma}{3\eta_0 R_0}$$

To Be Fitted:

$$y = \sinh^{-1} \left(\frac{h}{4B(2x-1)} \right)^{1/2}$$

$$\frac{1}{2}(e^{2y} - 1) + y = \frac{(t_c - t)}{2B}$$

for $i = 1, 2, \dots, N_{\text{data}}$

Left-Hand Side

$$y^{(i)} = \sinh^{-1} \left\{ \left(\frac{(R/R_0)}{4 \left(\frac{\lambda\sigma}{3\eta_0 R_0} \right) (2x-1)} \right)^{1/2} \right\} = \sinh^{-1} \left\{ \left(\frac{3\eta_0 R^{(i)}}{4(2x-1)\lambda\sigma} \right)^{1/2} \right\}$$

Right-Hand Side

$$\frac{1}{2B}(t_c - t^{(i)}) = \frac{\frac{\sigma}{6\eta_0 R_0} (t_c - t^{(i)})}{2 \frac{\lambda\sigma}{3\eta_0 R_0}} = \frac{\hat{t}_c - \hat{t}^{(i)}}{4\lambda}$$

2) Fitting

Determine \hat{t}_c (critical time) - intercept
 λ (relaxation time) - curvature
 $\frac{3\eta_0}{(2x-1)\sigma}$ (1/capillary velocity) - linear region

3) The Apparent Extensional Viscosity (Derived from Fit)

$$\eta_E \dot{\epsilon} = \eta_E \frac{-2}{R} \frac{dR}{dt} = \frac{(2x-1)\sigma}{R}$$

$$\eta_E = \frac{(2x-1)\sigma}{-2(dR/dt)} \text{ [Pa.s]} \quad \text{or} \quad \frac{\eta_E}{\eta_0} = \frac{(2x-1)\sigma}{\eta_0} \frac{1}{-2(dR/dt)}$$

- a) do this from data $dR^{(i)}/dt^{(i)}$
- b) do this from theory prediction (must be linear with rate, as this is the model prediction)

NB: for consistency, plot $R(t)$ [m] and dR/dt [m/s]

REFERENCES

1. Kavehpour, H.P. and G.H. McKinley, Tribo-rheometry: from gap-dependent rheology to tribology. *Tribology Letters*, 2004. 17(2): p. 327-355.
2. Hupp, S.J., A Tribological Study of the Interaction between Surface Micro Texturing and Viscoelastic Lubricants. 2004, MIT: Cambridge, MA.
3. Hupp, S. and D.P. Hart. Experimental Method for Frictional Characterization of Micro-Textured Surfaces. in *ASME/STLE International Joint Tribology Conf.* 2004. Long Beach, CA.
4. Tian, H., N. Saka, and N. Suh, Boundary Lubrication Studies on Undulated Titanium Surfaces. *Tribology Transactions*, 1989. 32(3): p. 289-296.
5. Blatter, A., M. Maillat, S.M. Pimenov, G.A. Shafeev, A.V. Simakin, and E.N. Loubnin, Lubricated sliding performance of laser-patterned sapphire. *Wear*, 1999. 232: p. 226-230.
6. Geiger, M., S. Roth, and W. Becker, Influence of laser-produced microstructures on the tribological behaviour of ceramics. *Surface and Coatings Tech*, 1998. 100-101: p. 17-22.
7. Wakuda, M., Y. Yamauchi, S. Kanzaki, and Y. Yasuda, Effect of surface texturing on friction reduction between ceramic and steel materials under lubricated sliding contact. *Wear*, 2003. 254: p. 356-363.
8. Fletcher, D.I., A. Kapoor, K. Steinhoff, and N. Schuleit, Wear behaviour and surface form evolution of a novel titanium carbide implanted surface under lubricated conditions. *Proc. Instn. Mech. Engrs Part J*, 2000. 214: p. 597-610.
9. Hamilton, D.B., J.A. Walowit, and C.M. Allen, A theory of lubrication by micro-irregularities. *Trans. ASME Journal of Basic Engineering*, 1966. 88: p. 177-85.
10. Etsion, I., State of the Art in Laser Surface Texturing. *J. of Tribology*, 2005. 127.

11. Wang, X., K. Kato, K. Adachi, and K. Aizawa, The effect of laser texturing of SiC surface on the critical load for the transition of water lubrication mode from hydrodynamic to mixed. *Tribology International*, 2001. 34: p. 703-711.
12. Pearlstein, F., *Electroless Plating*, in *Modern Electroplating*, F.A. Lowenheim, Editor. 1974, Wiley & Sons: New York. p. 710-747.
13. Yu, X.Q., S. He, and R.L. Cai, Frictional characteristics of mechanical seals with a laser-textured seal face. *J. of Materials Processing Tech.*, 2002. 129: p. 463-466.
14. Brizmer, V., Y. Kligerman, and I. Etsion, A Laser Surface Textured Parallel Thrust Bearing. *Tribology Transactions*, 2003. 46(3): p. 397-403.
15. Ronen, A., I. Etsion, and Y. Kligerman, Friction-reducing surface-texturing in reciprocating automotive components (C). *Tribology Transactions*, 2001. 44(3): p. 359-366.